NMR STUDY OF PHOTOISOMERIZATION IN BULK AND CONFINED LIQUID CRYSTALS

Doctoral Dissertation
Jožef Stefan International Postgraduate School
Ljubljana, Slovenia, May 2010

Supervisor: *prof. dr. Boštjan Zalar*

Evaluation Board:

prof. dr. Zdravko Kutnjak, Chairman, Jožef Stefan Institute, Ljubljana
prof. dr. Mojca Čepič, Member, Faculty of Education, UL, Ljubljana
prof. dr. Daniele Finotello, Member, Kent State University, USA

Blaž Zupančič

NMR Study of Photoisomerization in Bulk and Confined Liquid Crystals

Doctoral Dissertation

Raziskava fotoizomerizacije tekočih kristalov v neomejeni in omejeni geometriji z jedrsko magnetno resonanco

Doktorska disertacija

Supervisor: prof. dr. Boštjan Zalar

May 2010

MEDNARODNA PODIPLOMSKA ŠOLA JOŽEFA STEFANA
JOŽEF STEFAN INTERNATIONAL POSTGRADUATE SCHOOL
Ljubljana, Slovenia

Contents

Abstract

Deuteron nuclear magnetic resonance was used to study the phase separation behavior of photoisomerizable liquid crystal diheptylazobenzene (7AB). Under UV illumination, the elongated trans molecules are converted to boomerang shaped cis form, creating a binary trans-7AB and cis-7AB mixture. It was demonstrated that the concentration of both components can be controlled dynamically using UV-illumination stimulated trans-to-cis photoisomerization and thermally-induced cis-to-trans backisomerization. The so far elusive temperature-concentration phase diagram of such mixture has been determined by comparative analysis of the behavior in bulk, thin planar cell, and Anopore confining geometries.

Detailed information on mixing-demixing and isotropic-nematic phase segregation mechanisms was obtained by using a newly constructed deuterium NMR probehead which made it possible to perform in-situ UV illumination. In the nematic phase, the spectra of selectively deuterium-labeled photoisomerized 7AB consisted of two doublets, attributed to orientationally ordered trans and cis molecules, respectively. The temperature profiles of the order parameters of both components were determined from the T-dependent frequency splittings of the doublets, taking into account the average quadrupolar frequency $\overline{\nu}_Q = 53$ kHz, estimated from the powder pattern spectrum of crystallized 7AB. In the isotropic phase, NMR spectrum of bulk material exhibited a narrow central line.

In order to avoid the problems related to illumination-created spatial inhomogeneity of bulk samples, 7AB was confined to cylindrical pores of Anopore membranes. The flat geometry of membranes allowed for easy implementation of uniform illumination, resulting in a homogeneous concentration profile throughout the sample. In confined samples, a weak splitting of the isotropic central line was observed reflecting the surface-induced order. Similar to the nematic phase, the splitting could be controlled by changing either the temperature or the concentration.

The experimental temperature-concentration phase diagram was constructed by performing the measurements in the backisomerization regime, where sample heating effects due to non-resonant absorption of light are absent. Since the timescale of the backisomerization process was several hours, deuteron NMR experiments could be performed in a quasi-equilibrium regime. The concentration of cis molecules was shown to decay exponentially with time, whereas the characteristic decay times were found to be thermally activated with activation energy $E_a = 0.68$ eV. In the phase diagram, boundary lines separating the nematic and isotropic phases from the region of coexistence of both phases are clearly resolvable.

The measurements were modeled phenomenologically with an extended Landau-de Gennes theory. By taking into account the concentration-dependence of the free energy terms, as well as allowing for spatially-variable order parameter, we were able to reproduce the experimentally observed behavior of both nematic and surface-induced orientational order, including the phase boundary lines. The theory predicts straight isonematic lines in the temperature-concentration phase diagram, a behavior also confirmed experimentally. Photoisomerized confined 7AB thus behaves thermodynamically as a conventional binary nematic. Its main advantage, however, is the dynamically variable concentration by means of UV illumination. This provides for an easy way of accessing an arbitrary point in the temperature-concentration phase diagram.

Povzetek

Z metodo jedrske magnetne resonance smo preučili značilnosti fazne separacije fotoizomerizabilnega tekočega kristala diheptilazobenzena (7AB). Pri obsevanju z UV svetlobo se del podolgovatih trans molekul pretvori v upognjene cis molekule, zato nastane binarna trans-7AB/cis-7AB mešanica. Pokazali smo, da lahko koncentracijo obeh komponent dinamično spreminjamo z UV stimulirano trans-cis fotoizomerizacijo in s termično cis-trans relaksacijo. Do sedaj težko določljivi fazni diagram v odvisnosti od temperature in koncentracije smo določili s primerjalno analizo obnašanja materiala v neomejeni geometriji, v ploščati celici ter v omejeni geometriji Anopore membran.

Podrobne informacije o mešanju ter segregaciji izotropne in nematske faze smo pridobili z uporabo posebej prirejene sonde za JMR devterija, ki je omogočala osvetljevanje vzorca med meritvami. V nematski fazi so bili spektri z devterijem selektivno označenega fotoizomeriziranega 7AB sestavljeni iz dveh parov vrhov, ki sta ustrezala orientacijsko urejenim trans ter orientacijsko urejenim cis molekulam. Temperaturne profile ureditvenih parametrov obeh komponent smo določili iz temperaturno odvisnih frekvenčnih razcepov obeh parov vrhov. Pri tem smo upoštevali povprečno kvadrupolno frekvenco $\overline{\nu}_Q = 53$ kHz, ki je bila izmerjena iz praškastega spektra kristalnega 7AB. V izotropni fazi smo v JMR spektru 7AB v neomejeni geometriji zaznali ozko centralno črto.

Da bi se izognili težavam zaradi nehomogenosti, ki je posledica neenakomerne osvetlitve vzorcev neomejene geometrije, smo 7AB konfinirali v cilindrične kanale Anopore membran. Zaradi ploščate geometrije membran se da material na enostaven način enakomerno osvetliti, zato je koncentracija znotraj vzorca homogena. V konfiniranih vzorcih smo opazili majhen razcep izotropne centralne črte, ki je posledica urejanja zaradi vpliva površine. Podobno kot v nematski fazi smo razcep lahko regulirali s spreminjanjem temperature ali koncentracije.

Fazni diagram v odvisnosti od temperature in koncentracije smo določili z meritvami med termično cis-trans relaksacijo, saj takrat izločimo vpliv segrevanja vzorca zaradi neresonančne absorpcije svetlobe. Glede na to, da je karakterističen čas termične relaksacije nekaj ur, smo lahko meritve JMR devterija izvajali v kvaziravnovesnem stanju. Ugotovili smo, da se koncentracija cis molekul zmanjšuje eksponentno s časom. Pri tem so karakteristični razpadni časi termično aktivirani z aktivacijsko energijo $E_a = 0.68$ eV. Mejne črte, ki ločijo nematsko in izotropno fazo od koeksistenčnega območja faz, so v faznem diagramu jasno razvidne.

Meritve smo fenomenološko modelirali z razširjeno Landau-de Gennes-ovo teorijo. Pri tem smo upoštevali, da so členi v prosti energiji odvisni od koncentracije ter da se lahko ureditveni parameter prostorsko spreminja. Tako smo pojasnili eksperimentalno opažene značilnosti nematskega in površinsko induciranega ureditvenega parametra, vključno z mejnimi črtami v faznem diagramu. Teorija napoveduje ravne izonematske črte v faznem diagramu, kar je bilo tudi eksperimentalno potrjeno. Fotoizomeriziran konfiniran 7AB se termodinamsko obnaša kot običajen binarni nematik. Ne glede na to ima pomembno prednost, saj lahko koncentracijo komponent dinamično spreminjamo z UV osvetlitvijo. Na ta način lahko enostavno dostopamo do poljubne točke v faznem diagramu.

Abbreviations

5CB	=	4-pentyl-4′-cyanobiphenyl
7AB	=	diheptylazobenzene
EFG	=	electric field gradient
FWHM	=	full width half maximum
I	=	isotropic
IR	=	infrared
LC	=	liquid crystal
LCD	=	liquid crystal display
MEMS	=	micro-electro-mechanical system
N	=	nematic
N+I	=	nematic and isotropic coexistence
NMR	=	nuclear magnetic resonance
PAA	=	para-azoxyanisole
PDLC	=	polymer-dispersed liquid crystal
RF	=	radiofrequency
SEM	=	scanning electron microscopy
S/N	=	signal-to-noise ratio
UV	=	ultraviolet
UV-VIS	=	ultraviolet and visible

1 Introduction

The basic characteristics of mesomorphic systems like liquid crystals is the orientational ordering of molecules [1, 2]. Various possible spatial modulations of this orientational order are reflected in a rich palette of different thermodynamic phases. There are many applications of liquid crystalline materials, the most common being liquid crystal displays (LCD), where optical properties (the transmission and reflection of light) are manipulated by changing the orientational arrangement of molecules. In addition, liquid crystals are also used in light modulators, nonlinear optics, stereovision, adaptive optics, etc [3].

A special case of mesomorphic systems are confined liquid crystals. In contrast to bulk matter, the structure of confined liquid crystals is affected by the limiting interfaces which leads to a variety of surface effects [4]. Among them are the pretransitional effects and the change of the order of the phase transition [5]. In addition, surface can destabilize phases or produce new ones [6]. Due to the interplay between surface and bulk forces, confined liquid crystals are interesting from a theoretical point of view [7]. Furthermore, theoretical predictions can easily be tested since fluidity allows for liquid crystals to be introduced into variety of porous media. Examples are liquid crystals confined in thin flat cells [8], cylindrical cavities [9], square capillary tubes [10], random porous networks [11, 12] and small droplets [13]. One of the first and most known uses of confined liquid crystals are polymer-dispersed liquid crystals (PDLC) where the material can be made translucent or opaque simply by applying electric field [14]. In the past, a lot of applicative research was focused on explaining the surface anchoring which is important for liquid crystal display industry. Recently, confined systems are becoming important in the development of sensors [15, 16]. Small changes at the interface are magnified by the bulk which makes optical detection of targeted chemicals possible.

Another system that is interesting both theoretically and experimentally is a binary mixture where at least one component is liquid crystalline. Such mixtures exhibit behavior that is more complex than that of a single component liquid crystal. More specifically, phenomena such as phase separation and self-organization of colloidal droplets were observed in a microemulsion of liquid crystal and an isotropic fluid [17, 18]. Furthermore, it is expected that nematic microemulsions will provide a new kind of random disordering effect which is not found in other systems [19]. The usual way of preparing a two-component system is by mixing the starting materials in a specified ratio. When different concentrations of components are needed, the procedure has to be repeated. For a concentration dependence measurement, numerous samples have to be prepared which is a time consuming process.

A more efficient way of creating a binary mixture is photoisomerization. The ratio between isomers of a photo-active material can easily be controlled by light. Typically, derivatives of azobenzene are used where the conformation of the molecule changes in response to UV irradiation. This intriguing photo-induced change has found many potential application areas such as optical data storage, MEMS, artificial muscles, tunable diffraction gratings, lab-on-a-chip systems, molecular electronics and general manipulation of organic materials [20, 21, 22, 23, 24, 25]. The main advantage of using photo-active materials is the possibility of remotely controlling molecular structures. This was demonstrated with the twisting of a molecule [26], remote control of protein function [27] and flip-flop of amphiphilic molecules in lipid bilayers [28]. On a more

macroscopic scale, the motion of artificial cilia was demonstrated [29]. The key to understanding the photo-induced changes is the in-depth knowledge about the coupling between photoactive molecules and the surrounding matrix. Here, a liquid crystalline binary mixture can serve as a model system where any change in photoactive mesogens is reflected in the change of the liquid crystalline ordering.

The ordering in liquid crystals can be determined by using deuteron nuclear magnetic resonance. Although several other methods like optical birefringence, dielectric relaxation and small angle neutron scattering exist [30, 31], NMR is extremely sensitive to the orientational ordering of molecules and therefore the method of choice. This is especially true in confined systems, where NMR can be employed for the determination of liquid crystalline director configuration [32]. From the NMR spectra the information about both the order parameter and the director orientation can be obtained.

In the presented work we have combined the orientational ordering of liquid crystals with the disordering effect of non-mesomorphic solutes. This kind of binary mixture was produced dynamically by using a photoisomerizable liquid crystal where the cis isomer acts as impurity reducing the LC order of the trans molecules. In addition, the material was confined in cylindrical cavities of porous membranes to study the effect of cis isomer on the surface-induced order.

The photo-induced phase transitions in liquid crystalline mixtures have been studied before because of possibility for image recording applications [33]. Nevertheless, only a few measurements of the order parameters in photoisomerization-created mixtures are reported. In a previous study, Zalar and coworkers have reported deuterium NMR measurements of the order parameters in bulk photoisomerizable liquid crystal [34]. However, only the order in nematic phase was determined and due to bulk samples the material never reached full isotropic phase. The measurements of magnetic field induced order in the isotropic phase of a binary mixture were reported by Attard [35]. In this study, photoisomerization was not used which is why the concentration of non-mesomorphic solute was fixed at 7%. In comparison, our work combines the best methods from previous experiments. First, the concentration change is produced by photoisomerization which allows for an arbitrary concentration to be selected. By varying the concentration and temperature it is therefore possible to measure the entire phase diagram with a single sample. In addition, the confinement of the material allows for the determination of the surface-induced order inside porous membranes. It is thus possible to measure the order parameters of both phases, which allows for comparison of order parameter behavior in the nematic-isotropic coexistence region.

The main motivation for the work was to understand the influence of impurities on the order parameters and the phase transition behavior. The possibility to vary both concentration and temperature dynamically enabled us to compare the effects of these parameters. The measurements presented answer the question of interchangeability of temperature and concentration, which is important in any liquid crystalline system that exploits the photoinduced changes to alter the order inside a material.

The rest of this chapter gives general introduction to the topics of liquid crystals, photoisomerization and nuclear magnetic resonance. In chapter 2, the theoretical predictions concerning our system are presented. The experimental methods are described in chapter 3. Finally, main experimental results, discussion and conclusions are given in chapters 4 and 5.

1.1 Liquid crystals

Most materials have a single transition between crystal and liquid phase. At the phase transition temperature, the positional and orientational order of a crystal is destroyed and a liquid phase

is formed with no long range order. Liquid crystals on the other hand, have a cascade of transitions involving new phases [1, 2]. These phases are called mesomorphic which means they are an intermediate state between ordered crystal and isotropic liquid. Liquid crystals exhibit properties characteristic of liquids such as high fluidity as well as inability to support shear and the formation of droplets. At the same time, mesomorphic materials are similar to crystals because of anisotropic optical, electrical and magnetic behavior.

The molecules of liquid crystalline materials are called mesogens. The common feature of mesomorphic molecules is a highly anisotropic rod-like or disc-like shape. In rod-like calamitic materials, the long axis of the molecule is usually defined by a rigid backbone with double bonds and flat segments such as benzene rings. Many mesogens have strong dipoles and easily polarizable groups whereas the groups attached to the ends of the molecule do not influence much the formation of mesophases. A typical and widely used liquid crystalline molecules PAA (para-azoxyanisole) and 5CB (4-pentyl-4′-cyanobiphenyl) are schematically shown in Fig. 1.1.

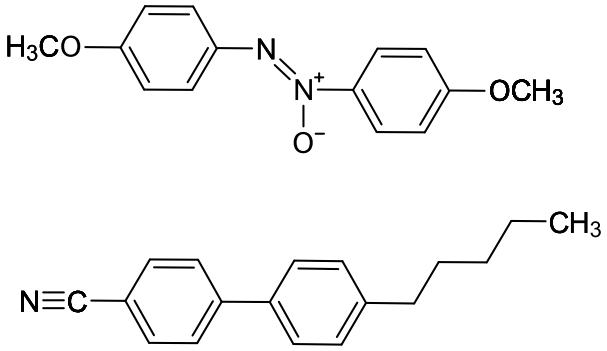

Figure 1.1 *Chemical structure of PAA (top) and 5CB (bottom).*

1.1.1 Liquid crystalline phases

A precise definition of a mesophase can be formulated by considering the orientational and positional order of the molecules. A mesophase can exist without any long range positional order. Whenever orientational order of molecules is the only long range order, the phase is called nematic. The positional order in one dimension is characteristic of smectic phases where the molecules form layers. The third possibility are columnar phases. In this case columnar stacks of molecules are arranged in two dimensions. In the simplest case the orientational order is spatially homogeneous. However, more complex structures exist. In cholesteric phases, the average molecular orientation is helically modulated in space.

A schematic representation of the nematic phase is shown in Fig. 1.2b. The molecules tend to orient along a preferred direction which is described by a vector called the nematic director **n**. Since only the direction is important, the director is a unit vector. The molecules in nematic phase can reorient around their long axes. Furthermore, there is no preferential orientation of both ends of the molecule. The sign of the director therefore has no physical meaning. For example, if the mesogen has permanent electric dipole along the long axis, the nematic material is not ferroelectric because there are as many dipoles oriented along **n** as along $-\mathbf{n}$ direction. The nematic material behaves optically as uniaxial medium with the optical axis along **n**.

In bulk nematic, the director does not change its direction. In real materials, however, the confining surfaces distort the director field. The resulting changes in the structure can be observed

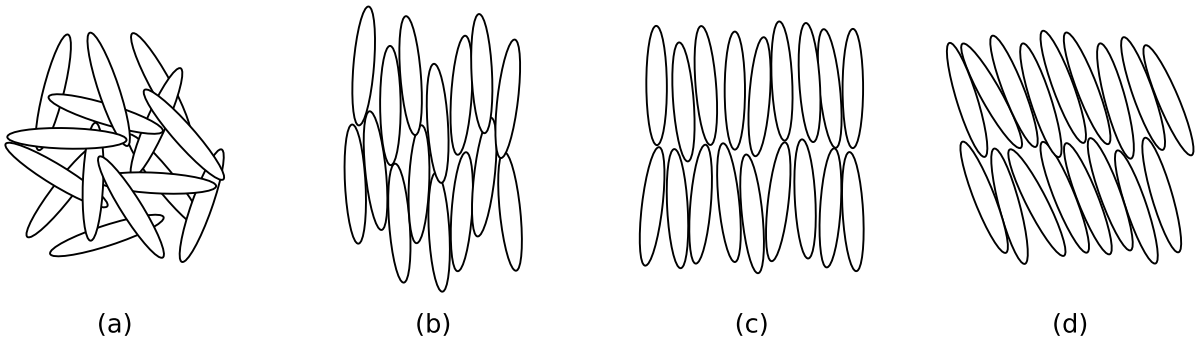

Figure 1.2 *Some of the possible phases of a liquid crystalline material: isotropic (a), nematic (b), smectic A (c) and smectic C (d).*

under a polarization microscope and appear as threads. The molecules that form nematic phase must be achiral which means that each molecule is identical to its mirror image. If this is not a case, then the nematic phase only exists in racemic (1:1) mixtures of left- and right-handed species. As mentioned before, there is no long range positional order a in nematic material. However, short range order may be present as in ordinary liquids.

In some materials, the lowering of temperature causes the formation of smectic phases. The main characteristic of smectic phases is the arrangement of molecules into layers with a well defined interlayer spacing. There are many types of smectic phases depending on the configuration and orientation of molecules inside each layer. A layer in the smectic A phase (see Fig. 1.2c) is essentially a two-dimensional liquid with no positional long range order. The long axes of the molecules are normal to the layer plane. This kind of material is optically uniaxial. On the contrary, smectic C phase (Fig. 1.2d) is optically biaxial because the molecules in each layer are tilted with respect to the normal of the layers. However, there is still no positional long range order inside the layers. This is not the case in smectic B phase where the molecules are locally distributed on a triangular lattice. This positional order extends to distances about a few 10 nm. The orientation of the molecules is the same as in the smectic A phase.

Besides the perpendicular and tilted orientation, a special case of molecular ordering appears when the mesogens are chiral. The molecules start to twist around the preferred axis so that the long axis of the molecule is perpendicular to the same axis. The phase with this kind of ordering is cholesteric. The twist of the molecules is periodical, characterized by the pitch of the director which is typically of the order of 1 μm. The actual spatial period of molecules is half the pitch since the directions $\mathbf{n}$ and $-\mathbf{n}$ are indistinguishable. It is interesting to note that the nematic structure is only a limiting case of cholesteric with infinite pitch. The described structure also appears in mixtures of chiral and achiral molecules and in mixtures of left- and right-handed chiral molecules if it is not racemic. By adding chiral dopants to the smectic liquid crystal it is possible to obtain chiral smectic structures. It is therefore possible to get chiral smectic A^* phase from simple smectic A.

Liquid crystals discussed so far were thermotropic which means that their configuration changes with temperature. The other important class are lyotropic liquid crystals where the concentration of mesogen in a solution is the primary parameter for phase transitions. The temperature is the secondary parameter for this kind of materials whereas the secondary parameter for thermotropic liquid crystals is the pressure. The most common lyotropic systems are amphiphilic molecules dissolved in water. It is possible to observe many phases in such systems including simple spherical micelles, cylindrical micelles and inverse micelles. At higher concentrations hierarchically organized superstructures can be observed. The knowledge about

this kind of systems is of high importance in biological research.

1.1.2 Order parameter

To quantitatively describe the ordering of liquid crystalline molecules, an appropriate order parameter has to be introduced. It has to be noted that different order parameters are used for different liquid crystalline phases. The nematic order parameter must have a non-zero value in the nematic phase and must vanish in the isotropic phase. Assuming that liquid crystal molecules are small rigid rods, we can specify the orientation of an i-th molecule by a unit vector $\mathbf{m}^i$ pointing along the long axis of the rod. The orientation vector can be defined by azimuthal and polar angles (ϑ, φ):

$$\begin{aligned} m_x^i &= \sin\vartheta\cos\varphi \\ m_y^i &= \sin\vartheta\sin\varphi \\ m_z^i &= \cos\vartheta \end{aligned} \tag{1.1}$$

The arrangement of rods can be described by a probability distribution function $f(\vartheta, \varphi)$ which gives the probability of finding a rod oriented in a small solid angle $d\Omega = \sin\vartheta\, d\vartheta\, d\varphi$ around the direction specified by ϑ and φ. It is tempting to define a vector order parameter similar to the one found in ferromagnetic materials. However, since nematic LC phase has a center of symmetry, the average $\mathbf{m}^i$ vanishes. Therefore, to describe the nematic ordering, an order tensor has to be used:

$$\mathbf{Q} = \frac{1}{2} < 3\mathbf{m}\otimes\mathbf{m} - \mathbf{I} > \tag{1.2}$$

Angle brackets denote the average over all the molecular orientations. To construct a second rank tensor, identity matrix $\mathbf{I}$ and direct product of unit vectors $\mathbf{m}^i$ are used. The order tensor is:

- traceless
- zero in the isotropic phase
- invariant to the sign of $\mathbf{m}$.

Eq. (1.2) gives a general expression for the order tensor. A specific coordinate system can be chosen in which the tensor has a diagonal form:

$$\mathbf{Q} = \begin{pmatrix} Q_{xx} & 0 & 0 \\ 0 & Q_{yy} & 0 \\ 0 & 0 & Q_{zz} \end{pmatrix} \tag{1.3}$$

The direction of the principal axis of the order tensor is the nematic director $\mathbf{n}$. Expression (1.3) is usually modified by taking into account the following relations:

$$\begin{aligned} S &= Q_{zz} \\ \eta &= \frac{Q_{xx} - Q_{yy}}{Q_{zz}} \end{aligned} \tag{1.4}$$

We have introduced the phase biaxiality η and the largest eigenvalue was denoted by S. The order tensor can now be written in its final form:

$$\mathbf{Q} = \begin{pmatrix} -\frac{S}{2}(1-\eta) & 0 & 0 \\ 0 & -\frac{S}{2}(1+\eta) & 0 \\ 0 & 0 & S \end{pmatrix} \tag{1.5}$$

The order tensor can be calculated for some specific molecular distributions. In the isotropic phase the probability distribution function is a constant $f(\vartheta,\varphi) = 1/4\pi$. From Eq. (1.2) it then follows:

$$Q_{ab} = \frac{1}{4\pi}\int_0^{2\pi} d\varphi \int_0^{\pi} \frac{1}{2}\left(3m_a m_b - \delta_{ab}\right)\sin\vartheta\, d\vartheta \tag{1.6}$$

The off-diagonal terms Q_{xy}, Q_{xz} and Q_{yz} include functions $\sin\varphi$ and $\cos\varphi$ that are integrated over the full period. These terms are therefore zero. It can be shown that the diagonal terms vanish as well. If we take Q_{zz} for example:

$$Q_{zz} = \frac{2}{4\pi}\int_0^{2\pi} d\varphi \int_0^{\frac{\pi}{2}} \frac{1}{2}\left(3\cos^2\vartheta - 1\right)\sin\vartheta\, d\vartheta = \frac{1}{2}(\cos\vartheta - \cos^3\vartheta)\Big|_0^{\frac{\pi}{2}} = 0 \tag{1.7}$$

It should be noted that the integration over ϑ from 0 to π was replaced by twice the integral from 0 to $\pi/2$ which is due to the fact that directions $\mathbf{m}$ and $-\mathbf{m}$ are indistinguishable.

In the case of a perfectly ordered nematic material all the molecules are oriented along the z axis. The Q_{zz} element in this case is $Q_{zz} = (3m_z m_z - 1)/2 = (3-1)/2 = 1$. Since the order tensor is traceless and there is cylindrical symmetry, it then follows:

$$\mathbf{Q} = \begin{pmatrix} -\frac{1}{2} & 0 & 0 \\ 0 & -\frac{1}{2} & 0 \\ 0 & 0 & 1 \end{pmatrix} \tag{1.8}$$

Another limiting case is when all the molecules are perfectly aligned perpendicular to the z axis. The order tensor in this case is:

$$\mathbf{Q} = \begin{pmatrix} \frac{1}{4} & 0 & 0 \\ 0 & \frac{1}{4} & 0 \\ 0 & 0 & -\frac{1}{2} \end{pmatrix} \tag{1.9}$$

In the uniaxial nematic phase, the biaxiality is zero and the nematic order tensor is defined solely by its largest eigenvalue S. It can be calculated according to Eq. (1.6). When the azimuthal angle ϑ is measured from the preferred direction $\mathbf{n}$ we can write a short form:

$$S = \frac{1}{2}\left\langle 3\cos^2\vartheta - 1\right\rangle \tag{1.10}$$

We have defined a scalar order parameter which is the only quantity needed to measure the degree of alignment of the molecules in the nematic phase. It is zero in the isotropic and between zero and one in the nematic phase. The value $S = 1$ can never be reached in real systems since it would mean all the molecules would have to be perfectly aligned. It is however possible for order parameter to be less than 0. According to Eq. (1.10) the negative values down to $-1/2$ correspond to molecules that orient perpendicular to the preferred direction.

1.1.3 Free energy

Equilibrium physical properties of a liquid crystalline phase can be calculated by minimizing the thermodynamic potentials such as Helmholtz free energy F or Gibbs free energy G with respect to the order parameter. For nematic liquid crystals, the calculation of free energies from phenomenological Landau-de Gennes model is the most common approach [36]. An assumption is made that the free energy is an analytic function of the order tensor as defined in Eq. (1.2). In

the vicinity of the phase transition, the order parameter has a small value and can be expanded in series. Up to the fourth order, the free energy density is:

$$f = f_0 + \frac{3}{2}AQ_{ab}Q_{ab} - \frac{9}{2}BQ_{ab}Q_{bc}Q_{ca} + \frac{9}{4}CQ_{ab}Q_{ab}Q_{cd}Q_{cd} \tag{1.11}$$

The summation is taken over repeated indices and the free energy density of the isotropic phase is denoted by f_0. There is no term linear in $\mathbf{S}$ because it is forbidden by symmetry. In the presence of external fields such term is possible, however, the isotropic phase does not exist at finite temperature in such case. The coefficients A, B and C are in general functions of temperature T and pressure p. A simple linear temperature dependence is assumed for coefficient A:

$$A = a(T - T^*) \tag{1.12}$$

Coefficients a, B and C are taken to be constant. Temperature T^* is not the actual phase transition temperature T_{NI}, but rather determines the limit of metastable supercooled isotropic phase. It is important to note that f is the free energy density and has to be integrated over the sample volume to obtain the free energy F. Furthermore, the difference between Helmholtz and Gibbs free energy should be noted. The former evolves to its minimum at constant temperature and volume while the latter at constant temperature and pressure. However, since the usual changes in density at the phase transition are only about 0.3 %, the difference between them is negligible [37]. For an uniaxial nematic material with an order parameter S, the free energy density can be expressed in a much simpler way as:

$$f = f_0 + \frac{1}{2}a(T - T^*)S^2 - \frac{1}{3}BS^3 + \frac{1}{4}CS^4 \tag{1.13}$$

In the case when the order parameter is not spatially homogeneous, additional terms have to be added to the free energy density. These terms depend on the gradient of the order parameter, must be scalars and must be invariant to symmetry operations of the nematic phase. Up to the second order, additional terms can be written as:

$$f_{el} = \frac{1}{2}L_1\frac{\partial Q_{ab}\partial Q_{ab}}{\partial x_c \partial x_c} + \frac{1}{2}L_2\frac{\partial Q_{ab}\partial Q_{ac}}{\partial x_b \partial x_c} \tag{1.14}$$

The coefficients L_1 and L_2 are the elastic constants.

The values of the coefficients for typical materials are given in table 1.1.

Table 1.1 *Typical material constants for cyanobiphenyls [38].*

	T_{NI} (K)	T^*(K)	$a\,(\mathrm{J/m^3K})$	$B\,(\mathrm{J/m^3})$	$C\,(\mathrm{J/m^3})$	$L_1\,(\mathrm{J/m})$	$L_2\,(\mathrm{J/m})$
5CB	308.3	307.2	$0.13\cdot10^6$	$1.6\cdot10^6$	$3.9\cdot10^6$	$6\cdot10^{-12}$	$12\cdot10^{-12}$
6CB	302.3	301	$0.15\cdot10^6$	$2.3\cdot10^6$	$6.2\cdot10^6$	—	—
7CB	315.2	313.8	$0.21\cdot10^6$	$3.3\cdot10^6$	$8.1\cdot10^6$	—	—
8CB	313.8	312.5	$0.18\cdot10^6$	$2.3\cdot10^6$	$5.2\cdot10^6$	—	—

The free energy density changes when external fields are present. In the case of external magnetic field, one has to take into account the magnetic susceptibility of liquid crystal. Since nematic material is anisotropic, the magnetic susceptibility is also anisotropic. For uniaxial nematic, the magnetic susceptibility tensor χ has two components: $\chi_\parallel$ along the axis and $\chi_\perp$ perpendicular to the axis. The anisotropy of magnetic susceptibility is defined as:

$$\Delta\chi = \chi_\parallel - \chi_\perp \tag{1.15}$$

The magnetic coupling contribution to the free energy density due to external magnetic field can be expressed as:

$$f_{ex} = -\frac{1}{2}\chi_{ab} H_a H_b = -\frac{1}{2}\chi_{\perp} H^2 - \frac{1}{2}\Delta\chi(\mathbf{n}\cdot\mathbf{H})^2 \tag{1.16}$$

The magnetic field vector is denoted by **H**. Similar expression can be derived for electric field.

1.1.4 Confined liquid crystals

The main difference between bulk and confined liquid crystals is a high surface-to-volume ratio of the latter. The surface affects the orientation of confined liquid crystalline molecules significantly. One of the main effects of surface potential is the change of the character of the phase transition from first to second order type [5]. In addition, a number of pretransitional effects have been observed such as the growth of disordered layer in the nematic phase and the growth of planar-oriented layer in the isotropic phase [6]. Moreover, surface-induced smectic phase has been predicted to exist at the interface between the ordering substrate and an otherwise uniaxial nematic material [39].

The confinement effects can be observed in various geometries including submicron liquid crystalline films and simple planar liquid crystal-wall interface [8, 40, 41]. Usually however, controlled porosity materials such as Nucleopore and Anopore membranes are used [9, 32]. These membranes consist of parallel cylindrical cavities ranging from few 10 nm to micrometer in diameter and can be easily filled with liquid crystalline materials. This kind of materials have pores of well known topology but random matrices such as silica aerogel [11] and controlled pore glass [42] can also be used.

There are two basic orientations of molecules at the surface of cylindrical membranes: homeotropic and planar. Homeotropically aligned molecules are perpendicular to the surface while the planar alignment occurs when the molecules are parallel to the cylinder axis. In general, molecules at the surface can be tilted and the orientation can then be described by a polar angle φ and azimuthal angle ϑ measured from the normal of the surface. The anchoring of the molecules on the surface distorts the director field, giving rise to a variety of different structures inside the pores [4].

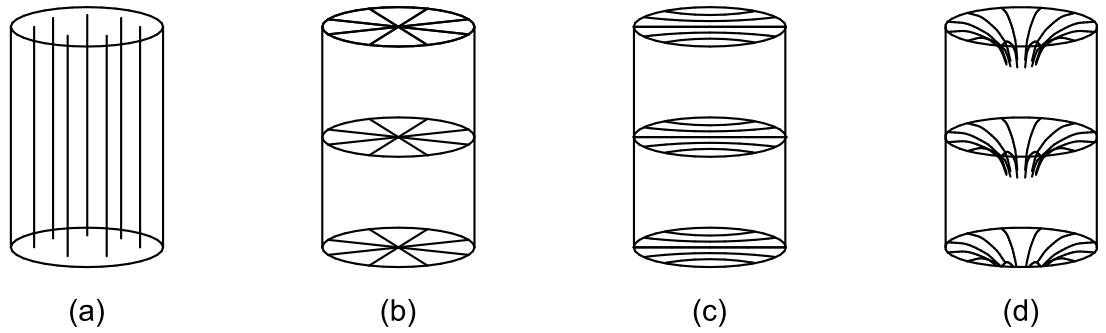

Figure 1.3 *Some of the possible director fields in cylindrical membranes: axial (a), radial (b), planar polar (c) and escaped radial (d).*

Some possible structures are schematically shown in Fig. 1.3. The most simple structure is axial where all the molecules are oriented along the cylinder axis. The next most common is radial or planar radial structure where the molecules are perpendicular to the cylinder axis. Planar polar, escaped radial and escaped radial configurations are also possible [32, 43]. Moreover, a whole new set of director fields can be introduced by applying electric field perpendicular to the pores which introduces another preferential direction. The configuration inside cylindrical pores

depends on the type of mesomorphic molecules. By varying the molecular length either axial or planar radial configuration can be obtained [44]. Many more configurations are possible with smectic materials. Examples are smectic planar radial, chevron, bookshelf and hybrid structures [45].

The anchoring of molecules can be changed by different surface treatments. A widely used substance for imposing homeotropic boundary conditions is lecithin [46]. The orientation at the surface can depend on the length of the surfactant. When aliphatic acids of variable length are chemically bonded to the pore surface, nematic-to-smectic transition occurrs in layers close to the surface in isotropic phase [47]. The transition is either continuous or discrete, depending on the liquid crystal type, surfactant length and surfactant surface coverage.

The interface effects of confined liquid crystals can be theoretically modeled by taking into account spatial inhomogeneity of the order parameter in Landau-de Gennes theory [8, 9, 41]. The model must include the elastic energy terms of Eq. (1.14) and the surface energy. Another approach is a modified Maier-Saupe theory which must include similar terms [48]. Recently, molecular simulations and Monte-Carlo studies were employed to study such systems [49, 50].

In particular, one of the most important parameters when predicting the behavior of confined systems is the anchoring energy. It is associated with the difference between bulk molecular orientation and orientation at the surface. To describe the anchoring free energy density, the Rapini-Papoular expression can be used:

$$f_s = \frac{1}{2} W \sin^2 \alpha \tag{1.17}$$

The angle between the actual and preferred anchoring directions is denoted by α and W is the molecular anchoring strength. It measures how easily the molecules can orient away from the preferred bulk direction. The expression is valid only when there is homeotropic anchoring. In other cases a more general form has to be considered, taking into account the tilt which is described by polar W_φ and azimuthal W_ϑ anchoring strengths.

To describe the pretransitional effects, a phenomenological surface free energy density is often used:

$$f_s = -GS\,\delta(z) \tag{1.18}$$

The surface energy is linear in order parameter S with a proportionality constant G. The interaction is short-range as can be seen from expression $\delta(z)$ where z measures the distance from the surface. With Eq. (1.18), pretransitional ordering and boundary layer phase transition can be predicted [41]. The expression for the surface energy density can be extended to include the disordering effects of the surface:

$$f_s = (-GS + \frac{1}{2} U S^2)\delta(z) \tag{1.19}$$

The disordering is described by the quadratic term with the coupling constant U.

It has been suggested that a more realistic surface potential should be used to describe liquid crystal-wall interface [51]. This approach considers Van der Waals forces between liquid crystal molecules and the surface:

$$V_s(z) = -\frac{g}{z^3} P_2(\cos\vartheta) \tag{1.20}$$

The angular dependence is described by the second Legendre polynomial P_2.

The pretransitional growth of ordered layers at the surface in the isotropic phase is called orientational wetting. The wetting regime can be described by the adsorption parameter:

$$\Gamma = \int_0^\infty (S(z) - S_b) dz \tag{1.21}$$

The parameter takes into account the difference between the actual order parameter $S(z)$ at the distance z from the surface and the preferred bulk order parameter S_b. There are two wetting regimes: partial and complete. The difference can be seen when the material is cooled from the isotropic phase and approaches the nematic-to-isotropic transition. When the adsorption parameter diverges to infinity the wetting is complete. On the other hand, finite adsorption parameter shows partial wetting.

The confinement effects can be investigated by various experimental methods. The obvious choice are optical methods such as birefringence measurements [5] or evanescent wave ellipsometry [6]. To study the nematic field inside cylindrical pores of the membranes, deuterium NMR was successfully employed since the nematic structure can be deduced from the NMR spectrum [32, 52]. Other methods such as calorimetry can also be used [42].

One of the most interesting phenomena associated with confined liquid crystals is the modification of nematic-to-isotropic phase transition. It was predicted theoretically, that on confining the material below the critical thickness of about 100 nm in at least one direction, a boundary layer phase transition occurs [41]. The transition exhibits critical behavior where the nematic phase continuously converts to the paranematic phase. The critical temperature is calculated to be 0.17 K above the bulk first-order phase transition temperature. The predictions were made using Landau-de Gennes theory with an arbitrary strength short-range potential [8]. Similar results were obtained using a modified Maier-Saupe model [48].

Probably the most widely known application of confined mesogens are polymer-dispersed liquid crystals [4]. They are easily prepared by mixing a liquid crystal with a prepolymer having a low molecular weight. When the solution is slowly cured, submicron nematic droplets form. Since the orientation of nematic director in the droplets is random, the material strongly scatters light and is therefore opaque. Under electric field the director reorients which results in a transparent material.

1.1.5 Mixtures of liquid crystals

The main interest in nematic mixtures is due to display technology, where the temperature range of nematic phase is of great importance [3]. A generalized phase diagram of two nematics is shown in Fig. 1.4. By mixing two nematogens, an eutectic composition can be obtained where the melting point is the lowest. This transition temperature is lower than in any of the components alone whereas the nematic-to-isotropic transition temperature is not much reduced. Another important application of mixtures are nematics with cholesteric additives where a twisted structure is created in an otherwise nematic material. Such mixtures are used in twisted nematic displays which are now in general use [53].

From a more basic point of view, miscibility studies can be used to obtain new phases. Such experiments can easily be carried out in a concentration gradient. By observing the mixture under a microscope, new phases can be identified. The nematic species A and B usually show continuous miscibility. If they are chemically similar, the solution can be ideal with zero enthalpy of mixing. This is true even when one of the species is not nematic.

The most simple case where only one of the components is nematic is a binary mixture of rod-like and spherical molecules [54]. Spherical molecules act as impurities and reduce the anisotropic interactions between nematic molecules. The phase diagram of such mixture exhibits three regions. At low temperature and low concentration of spherical molecules the material is nematic. At higher concentrations a separate region occurs where nematic phase coexists with the isotropic phase. As expected, the material is completely isotropic at high temperatures. The coexistence region appears because of demixing of two types of molecules. It has to be

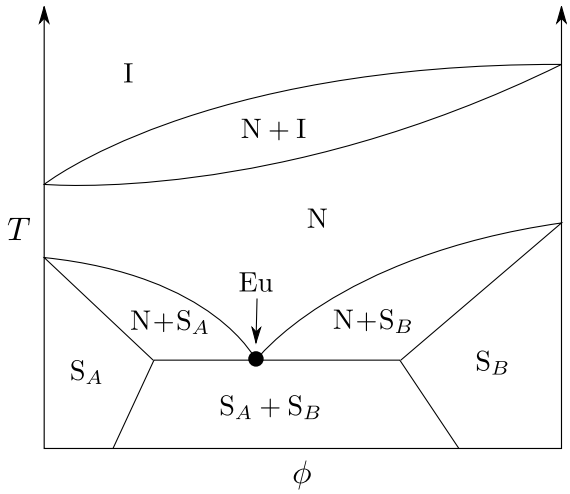

Figure 1.4 *Generalized phase diagram showing isotropic (I), nematic (N) and smectic (S_A, S_B) phases. At a certain concentration ϕ, eutectic point (Eu) can be seen.*

stressed however, that the coexisting isotropic and nematic phase do not consist of only one type of molecules. Only the concentrations of the two molecular species are different so that the nematic phase is rich in rods while the isotropic phase is rich in spherically shaped molecules. The nematic-to-isotropic transition temperature is generally lowered in such systems [55].

Mixtures of liquid crystals are important because they give insight into molecular interactions which are responsible for liquid crystalline behavior. Due to interactions between different kind of molecules it is possible for a mixture to have more ordered phases than individual components. An example is a mixture of two nematic components that form smectic phase in a limited concentration and temperature interval [56]. This kind of system was predicted theoretically using a combination of Flory-Huggins model for isotropic mixing and Maier-Saupe model of nematic ordering [57]. Another approach to describing demixing behavior are Parsons-Lee and Onsager type theories which take into account the steric effects associated to the particular molecular geometries [58].

1.2 Photoisomerization of azobenzene

In general, photoisomerization is a photochemical phenomenon originating from the interaction of atoms and small molecules with light. The first step of any photochemical reaction is photoexcitation. In this process, a photon of electromagnetic radiation with energy $E = h\nu$ is absorbed by the reactant directly or by a photosensitizer which then transfers the energy to the reactant. The reactant transforms to an excited energy state which can be deactivated by a process called quenching. In general, photochemical reactions are not reversible. A typical examples of such reactions are photodegradation of materials, photocuring and photoresistance. However, photochemically or thermally reversible reactions are also possible. These reactions are photochromic.

1.2.1 Photochromism

The first reports on reversible change of color are from 1867 when Fritsche observed that orange colored tetracene, when illuminated, changed to colorless material which converted back to tetracene with heating [59]. The effect was named photochromism using Greek words for light

and color. There is considerable interest in photochromism because of potential applications and importance in biological phenomena. Photochromic materials are used for ophthalmic lenses, photoimaging, information storage, holography, non-linear optics etc.

There are two conditions for a photochromic reaction [60]. It has to be a reversible transformation between two states of a single chemical species, which is at least in one direction induced by electromagnetic radiation. In addition, the two states must have different absorption spectra.

Common photochromic reactions are unimolecular. The starting material A transforms under UV, visible or IR illumination to the product P. The back reaction where the starting material is formed again can be induced photochemically (P-type) or thermally (T-type). This can be written as:

$$\begin{aligned} \mathrm{A} &\xrightarrow{h\nu} \mathrm{P} \\ \mathrm{P} &\xrightarrow{h\nu'} \mathrm{A} \\ \mathrm{P} &\xrightarrow{kT} \mathrm{A} \end{aligned} \tag{1.22}$$

Besides unimolecular reactions, bimolecular processes are also possible:

$$\mathrm{A} + \mathrm{B} \xrightarrow{h\nu} \mathrm{P} \tag{1.23}$$

The back reaction for this type of process can be unimolecular or bimolecular.

Photochromic reaction can significantly impact the physical properties of the reactant. Besides the change in absorption spectrum, changes in quantum yield, refractive index, and dielectric constant of the material can be observed. These changes can then in turn induce changes in the surrounding solvent or polymer.

So far we have discussed only processes where one photon is absorbed. It is however possible for a photochromic system to absorb two photons of the same or different frequencies simultaneously [61]. Since this kind of process is much weaker than one-photon absorption, high intensity light such as that from a laser has to be used. Two-photon absorption is a non-linear process, since the probability for absorption changes as the square of the light intensity. This property is exploited in holography and optical recording systems [62].

The absorption of electromagnetic radiation in a certain substance is possible only when the energy of a photon matches the splitting between the energy levels. In order to calculate the energy levels of a molecule, molecular orbital theory has to be employed. A molecular orbital is a one-electron wavefunction smeared throughout the molecule [63]. The strength of every bond depends on all electrons in the molecule. Molecular orbitals are in general very complex functions. However, they can be approximated mathematically by linear combinations of atomic orbitals. For a diatomic molecule this can be written as:

$$\psi = c_A \psi_A + c_B \psi_B \tag{1.24}$$

Eq. (1.24) can be further simplified in the case of a simple homonuclear molecule such as H_2^+, where the probability of finding an electron in orbital A or orbital B has to be the same ($c_A^2 = c_B^2$):

$$\psi = \psi_A \pm \psi_B \tag{1.25}$$

In the case of addition of atomic wavefunctions there is constructive interference of the wavefunctions between the nuclei. The probability of finding an electron between the nuclei is high which lowers the energy of the molecule compared to the energy of separate atoms. This is an example of a bonding orbital which increases the bond strength of a molecule. On the contrary, if

the atomic wavefunctions are subtracted we get an antibonding orbital because the wavefunctions destructively interfere. Therefore, the probability of finding an electron between the nuclei is zero and the energy of the molecule is higher. This kind of orbital, if occupied, lowers the bond strength of the molecule. In addition, non-bonding orbitals are possible which do not change the stability of the molecule.

In the example above, the bonding and antibonding orbitals are denoted by 1σ and $1\sigma^*$ respectively. The Greek letter σ is used in analogy with the electron orbital s since both have zero orbital angular momentum and number 1 represents the σ orbital with the lowest energy. Likewise, π bonding and π^* antibonding orbitals can be constructed by constructive or destructive linear combination of p electron orbitals. The σ and π orbitals occupied with two electrons are called σ-bond and π-bond respectively. An important parameter that describes the bond strength is the bond order $b = (N - N^*)/2$, where N counts the electrons in bonding orbitals and N^* is the number of electrons in antibonding orbitals. Bonds with high bond order are stronger and shorter than ones with low bond order.

The principles of determining the ground electron configuration in molecules are similar to ones valid for the interacting electrons of an atom. The valence electrons of the atoms in the molecule have to occupy the lowest energy orbitals while obeying Pauli exclusion principle. When there are degenerate orbitals, these have to be occupied by a single electron before double occupancy occurs. According to the Hund's rule, electrons occupying degenerate orbitals have parallel spins. This gives rise to two term systems: a singlet and a triplet system. The singlet system is the usual ground state of normal organic molecules while the triplet can be mostly found in inorganic molecules that have degenerate energy levels.

The configuration of electrons in orbitals is changed when a molecule absorbs electromagnetic radiation. The typical energy needed is of the order of a few electronvolts. This means that the wavelength of radiation usually lies in the visible or UV range of the spectrum. When an electronic transition occurs, the electron density is rapidly changed which excites vibrations of the molecule. This gives rise to vibrational structure of electronic transition where absorption spectrum consists of multiple lines. In gaseous phase these lines can readily be observed, whereas in liquid or solid state they merge into a broad absorption band.

In organic molecules $n - \pi^*$ and $\pi - \pi^*$ electronic transitions are common. The former occurs when an electron is excited from a non-bonding orbital to an antibonding π^* orbital. An example is the lone pair of electrons in an O atom where one of them is excited to an empty π^* orbital. The typical absorption energy for the transition is around 4 eV [63]. The $\pi - \pi^*$ transition occurs when an electron is excited from a bonding π to an antibonding π^* orbital with a typical absorption energy of about 7 eV. The absorption energies can be changed significantly if a solvent is used. This is especially true for polar solvents which interact with the molecules and cause a red shift for $\pi - \pi^*$ and blue shift for $n - \pi^*$ transitions.

An excited molecule can return to the ground state by thermal dissipation of its energy which is the most common process. In some cases, however, the excitation energy can be released by radiative decay where a photon is emitted while the molecule relaxes to the ground state. There are two types of radiative decay: fluorescence and phosphorescence. The main difference is that in fluorescence photons are emitted immediately whereas in phosphorescence the emission can persist for longer time after the absorption.

Energy levels and relaxation of excited molecule can be represented graphically by drawing a Jablonski diagram. It is important to note that the energy of the molecule is the sum of the following contributions:

- the electronic energy

- the vibrational energy
- the rotational energy.

In Jablonski diagram, the electronic states are arranged vertically with thick lines representing electronic states and thin lines representing excited vibrational states. Horizontally, the electronic states are grouped by spin multiplicity. Radiative transitions are represented by straight arrows whereas non-radiative transitions are marked by wavy arrows. Besides internal conversion, which is a transition between two electronic states, vibrational relaxation and intersystem crossing are possible. The former is a relaxation from higher to lower vibrational level of the same electronic state whereas the latter is a transition to a state with different spin multiplicity.

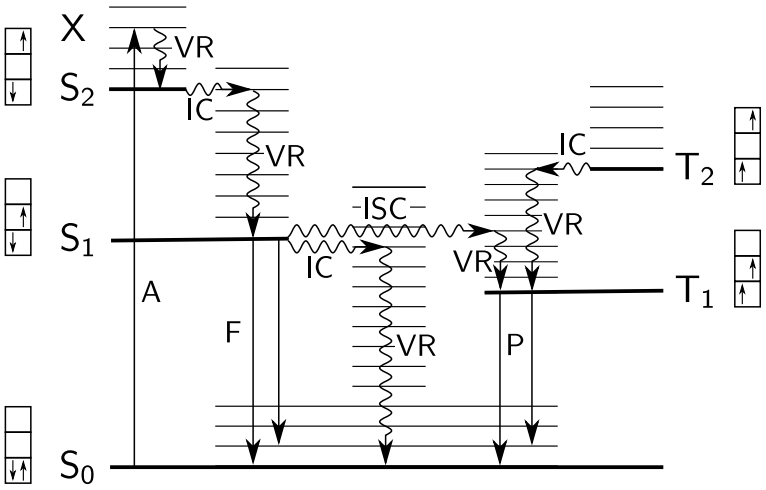

Figure 1.5 *Jablonski diagram showing the possible relaxation processes after initial absorption (A) of a photon: vibrational relaxation (VR), internal conversion (IC), intersystem crossing (ISC), fluorescence (F) and phosphorescence (P).*

An example of Jablonski diagram is shown in Fig. 1.5. The system absorbs a photon within about 10^{-15} s and moves to an excited state X [64]. Next, the vibrational relaxation process starts and within typically $10^{-14} - 10^{-11}$ s the ground vibrational state S_2 is reached. The system then relaxes to the ground vibrational state S_1 by internal conversion and further vibrational relaxation. This non-radiative step can be repeated once more to reach the ground state S_0. However, the ground state can be reached also radiatively by fluorescence which is usually on the timescale of $10^{-9} - 10^{-7}$ s. The third possibility is the intersystem crossing where the system first converts to the triplet state and then relaxes radiatively by phosphorescence within about $10^{-3} - 10^{-2}$ s. The last option is a photoreaction which changes the molecular structure.

Photoreactions usually start from the singlet S_1 or the triplet T_1 excited state. The primary photochemical processes of a photoreaction can be classified into the following groups:

- spontaneous monomolecular deactivations:

$$A \longrightarrow B + C$$

- reactions with the other reactants:

$$A + B \longrightarrow C$$

- photopolimerizations:

$$A + A_2 \longrightarrow A_3$$

- rearrangements:

$$A \longrightarrow B$$

A typical example of a rearrangement is the trans-to-cis photoisomerization which occurs in a variety of substances including stilbenes, azines and azo compounds.

1.2.2 Trans-to-cis photoisomerization

Trans-to-cis photoisomerization is typical for azobenzene which is characterized by two phenyl rings separated by an azo bond: $-N=N-$ [65]. This kind of structure is the basis for a broad range of azo compounds or diazenes. The primary use of diazenes was for dyes and colorants due to the strong electronic absorption maximum that can be anywhere between UV and visible region depending on the molecular structure. However, because of the rigid shape of the molecule, liquid crystalline phases are often formed making the material useful for doping into liquid crystals and polymers. Furthermore, azo materials can be incorporated into amorphous glasses, sol-gel silica glasses, self-assembled monolayers and various biomaterials.

Diazenes can be separated into three distinct spectroscopic classes [66]:

- azobenzenes
- aminoazobenzenes
- pseudo stilbenes.

Qualitatively they can be distinguished by their typical colors which are yellow, orange and red, respectively. Quantitatively, the classification depends on the positions of absorption peaks (Fig. 1.6).

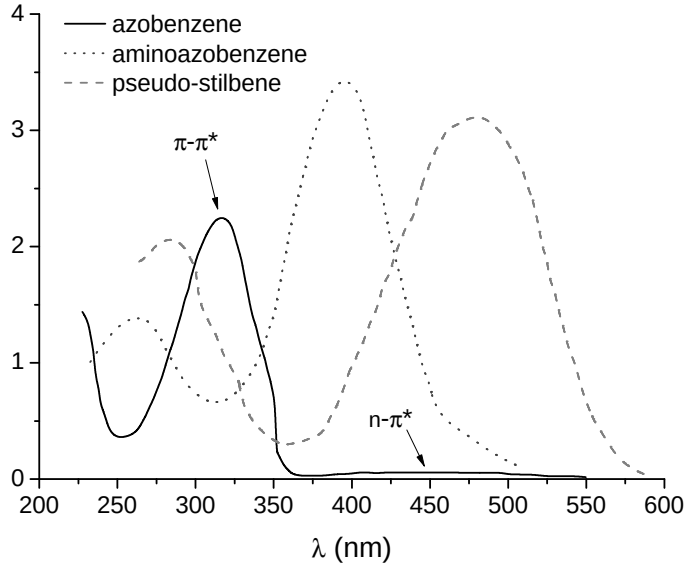

Figure 1.6 *Typical absorption peaks of the three spectroscopic classes of diazenes.*

Azobenzene type molecules have a high intensity $\pi - \pi^*$ band in the UV region and a low intensity $n - \pi^*$ band in the visible region of the spectrum [67]. The energy gap between bands is large. In aminoazobenzene type molecules, the absorption bands are close together and often the $n - \pi^*$ absorption is hidden below much stronger $\pi - \pi^*$ absorption band. The third type of

molecules, pseudo stilbenes, are characterized by completely reversed absorption bands with $\pi - \pi^*$ absorption in the visible region.

In general, azobenzene molecules do not emit, however there are some exceptions where weak fluorescence was observed on a picosecond timescale [68]. Fluorescence is possible also in aminoazobenzenes [69] and is common in pseudo stilbenes [70]. Although triplet states were detected in aminoazobenzene and pseudo stilbene type molecules [71], no phosphorescence was reported in any type of diazene.

While solvent polarity has little effect on azobenzenes, the absorption bands shift considerably in aminoazobenzenes. In nonpolar solvents, aminoazobenzenes absorb at higher energy and in polar solvents at lower energy. Depending on the solvent, this type of molecule may therefore behave as azobenzene or pseudo stilbene type. Of all three types, pseudo stilbene molecules show the strongest dependence on solvent polarity. Besides the solvent, packing and aggregation can influence the absorption bands significantly. The band shift depends on the alignment of azo dipoles and is redshift if they are oriented parallel or blueshift if they are antiparallel.

The photoisomerization of diazenes is a completely reversible conversion between trans (E) and cis (Z) geometric isomers. The process is free from side reactions and can be induced in both directions by light and in cis-to-trans direction thermally. The trans isomer has lower energy by ~ 0.5 eV and is thus more stable [72]. The energy barrier for the photoisomerization is about 2 eV [73]. In the dark, most molecules are therefore in the trans form so that the cis concentration is usually not detectable.

Upon absorption of a photon, the trans form is converted to the cis form on a picosecond timescale [74]. The resulting cis isomer has phenyl rings twisted at 90° relative to the $-\mathrm{N}=\mathrm{N}-$ plane and the distance between 4 and $4'$ atoms is reduced from 0.99 nm to 0.55 nm [75, 76, 77]. This displacement is very large on molecular scale and generates molecular forces on the pN scale which were measured by single-molecule force spectroscopy experiments [78]. In addition, the dipole moment is increased from zero to 3.1 Debye [79].

Backisomerization can occur by absorption of a photon of a different wavelength or thermally. In the latter case, the energy barrier for backisomerization is about 0.9 eV [80]. In the dark, the rate of conversion to the trans state is typically measured in hours, minutes and seconds for azobenzenes, aminoazobenzenes and pseudo stilbenes, respectively. The lifetime of diazenes can be prolonged by bulky ring substituents and the cis-to-trans conversion can be completely stopped by attachment to surface or crystallization [81, 82].

Under illumination, the steady state will be reached when the number of molecules that undergo photoisomerization in a given time is the same as the number of molecules that are backisomerized either optically or thermally. The steady-state cis and trans concentrations depend on the quantum yields of the cis-to-trans process, trans-to-cis process and the thermal relaxation rate. These in turn depend on the intensity and wavelength of incident light, the temperature and the matrix into which the molecules are incorporated. The quantum yields for the azobenzene molecule are around 0.6 in cis-to-trans and 0.25 in trans-to-cis direction [83, 84]. In aminoazobenzenes and pseudo stilbenes the quantum yield for the trans-to-cis photoisomerization can be as high as 0.8 [85]. In this case, the cis-to-trans quantum yield is hard to determine because of the fast thermal relaxation. Due to different relaxation rates, the photostationary state under moderate illumination is predominantly cis for azobenzenes, mixed for aminoazobenzenes and mostly trans for pseudo stilbenes. The relaxation to the trans state and the steady-state concentrations in a solution can be determined by absorption spectroscopy [86, 87].

There has been much debate about the mechanism of photoisomerization. The change in conformation occurs after initial absorption of a photon and subsequent relaxation to a ground

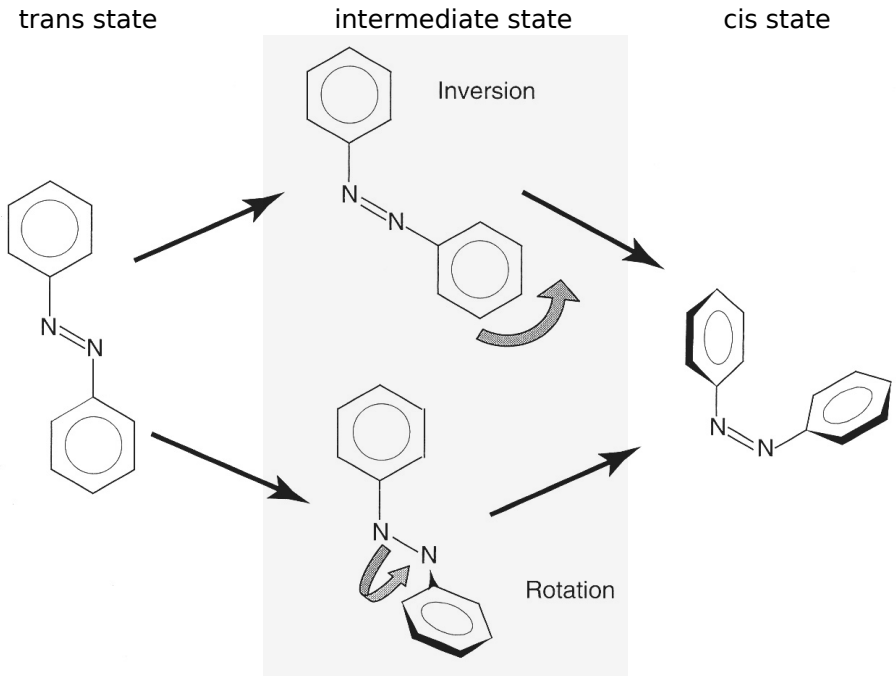

Figure 1.7 *The two possible photoisomerization pathways of azobenzene compounds.*

vibrational state (see Fig. 1.5). The two possible mechanisms, rotation and inversion are schematically represented in Fig. 1.7. The rotation mechanism is a rotation about the N = N bond which breaks the π bond. On the contrary, the π bond remains intact when inversion mechanism takes place. In this case only the C − N = N angle changes and the transition state is planar. One of the main arguments for two photoisomerization pathways are the measured trans-to-cis quantum yields, which are different if the electronic transition is $n-\pi^*$ or $\pi-\pi^*$. The former is excitation into S_1 state and relaxes via inversion while the latter corresponds to S_2 state and relaxes through rotation [88]. There is however evidence that challenges this model. The picosecond Raman and femtosecond fluorescence spectroscopy showed that a double N = N bond remains intact in the excited state which opposes the rotation mechanism [89, 90]. Theoretically, ab initio calculations showed that both pathways are energetically possible [91]. The free volume requirement for photoisomerization via rotational pathway is estimated around 0.3 nm^3 which is much larger than 0.1 nm^3 required for inversion [92, 93]. This suggests that inversion pathway is preferred in rigid matrices such as polymers.

1.2.3 Photokinetics

Any quantitative analysis of photoreactions requires knowledge about the amount of absorbed light. In the most simple case when the sample is homogeneous and there is low concentration of absorbing species, absorption can be described by Beer-Lambert law. The law states that the absorbance of a sample is proportional to the optical path length through the sample and the number or concentration of the absorbing molecules.

The decrease of intensity of light through the sample is schematically presented in Fig. 1.8. A thin layer with volume V contains N absorbing molecules. The optical path through this element is dx and the irradiance at the position of the element x is $I(x)$. When the light passes through this element the intensity is decreased by:

$$dI = -\kappa I n dx \tag{1.26}$$

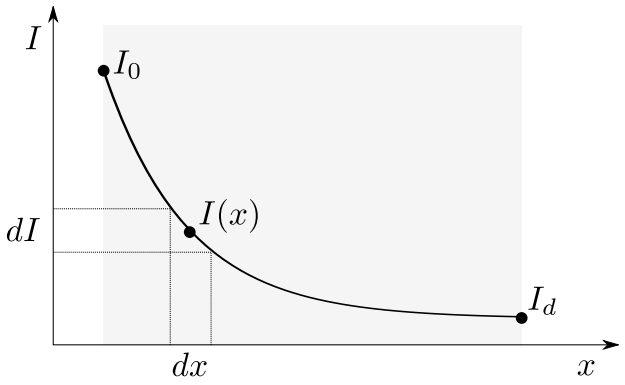

Figure 1.8 *Intensity profile in a sample of thickness d.*

The proportionality factor κ is the natural absorptivity and $n = N/V$ is the concentration of the absorbing species. The solution of Eq. (1.26) gives us the exponential intensity profile:

$$I(x) = I_0 e^{-\kappa n x} = I_0 10^{-\varepsilon n x} \tag{1.27}$$

The intensity of light incident on the sample is denoted by I_0 and ε is the molar absorption coefficient or molar absorptivity. This coefficient is an intrinsic property of the absorbing species and changes with the wavelength of the incident light $\varepsilon = \varepsilon_\lambda$. It is connected to natural absorptivity κ by a simple relation $\varepsilon = \kappa \log e$.

When there is more than one type of absorbing molecules, the total absorption in a sample of thickness d can be written as:

$$E = d \sum_i \varepsilon_i n_i = \log e \, d \sum_i \kappa_i n_i = K \log e \tag{1.28}$$

By inserting this expression into Eq. (1.27) we obtain the new expression for the intensity profile through the sample:

$$I(x) = I_0 e^{-K x/d} = I_0 10^{-E x/d} \tag{1.29}$$

From this equation the total amount of absorbed light in the sample can be calculated. However, to describe photoreactions with many absorbing species, the amount of light absorbed by any one of them has to be known. For species A with concentration n_A and absorptivity κ_A we can write:

$$dI_A = -\kappa_A n_A I(x)\, dx \tag{1.30}$$

The solution of equations (1.29) and (1.30) is the amount of light that is absorbed by species A:

$$I_A = I_0 \kappa_A n_A \frac{1 - e^{-K}}{K} d = I_0 \kappa_A n_A F d \tag{1.31}$$

The expression $F = (1 - \exp(-K))/K$ is the photokinetic factor which takes into account that only some of the totally absorbed light is absorbed by one species.

Beer-Lambert law has many limitations. It is valid only for diluted solutions. As a rule of thumb we can use it for concentrations up to 10^{-3} mol/l or when there is more than 10% light transmission. Furthermore, the absorbers in the solution should act independent of each other and should not be influenced by incident light. Since the absorptivity is wavelength dependent, the incident light must be monochromatic. In addition, the incoming beam should be collimated and uniform. Nevertheless, in many cases these conditions are fulfilled and we can calculate the absorbed light to a good precision.

Only some of absorbed photons induce a photoreaction. It is therefore necessary to define quantum yield of a photoprocess which is the ratio between the number of events occurring and the amount of absorbed photons in a given time interval. However, as discussed before, one has to be careful about defining the amount of absorbed photons when there are more types of absorbing molecules. True quantum yield should take into account only the photons which are absorbed by a single species. This should be distinguished from apparent quantum yield where all the absorbed light is calculated. Instead of the number of photons and the number of events it is more convenient to define the quantum yields with measurable quantities such as light irradiance and the number density of absorbing species. In total, three expressions for true quantum yields can be written [60]:

$$\Phi_A = \frac{n_A(t) - n_A(0)}{\int I_A(t)dt} \tag{1.32}$$

$$\phi_A = \frac{\dot{n}_A}{I_A} \tag{1.33}$$

$$\varphi_A^k = \frac{\dot{x}_k}{I_A} \tag{1.34}$$

They are true integral quantum yield Φ_A, true differential quantum yield ϕ_A and partial quantum yield φ_A^k, respectively. The partial quantum yield is necessary for photoreactions that consist of many steps and is defined for each linear independent step k of the reaction.

With known quantum yields the rate equations for photoreactions can be derived. In the case of trans-to-cis photoisomerization, which is a photoreaction of type (1.22) the following holds:

$$\dot{n}_{tr} = -\phi_{tr} I_{tr}(t) + \phi_c I_c(t) + k_c n_c(t) \tag{1.35}$$

The index tr corresponds to trans-to-cis and index c to cis-to-trans photoisomerization. The concentration of trans molecules decreases proportionally to the light absorbed by the trans molecules and increases proportionally to the light absorbed by cis molecules. The last term is the increase in trans concentration because of thermal backisomerization of cis molecules and linearly depends on cis concentration with coefficient k_c. Eq. (1.35) can be further simplified by considering the fact that the number of molecules in the system is constant. The sum of concentrations therefore equals the starting trans concentration $n_{tr}(t) + n_c(t) = n_{tr}(0)$. Moreover, by inserting expression (1.31) for the amount of absorbed light we obtain:

$$\dot{n}_{tr} = -\left[I_0 d\, F(t)(\kappa_{tr}\phi_{tr} + \kappa_c\phi_c) + k_c\right] n_{tr}(t) + \left[I_0 d\, F(t)\kappa_c\phi_c + k_c\right] n_{tr}(0) \tag{1.36}$$

So far we discussed only systems where the concentration of absorbing species in the sample was homogeneous. This can be achieved by efficient stirring. When the sample is not in a solution this is not possible and the concentration depends on the position inside the sample. This in turn changes the amount of absorbed light which can not be taken into account by the simple photokinetic factor. This kind of system can be described by the following partial differential equations [60]:

$$\begin{aligned}
\frac{\partial n_{tr}(x,t)}{\partial t} &= -\kappa_{tr}\phi_{tr} n_{tr}(x,t) I(x,t) + \kappa_c\phi_c n_c(x,t) I(x,t) + k_c n_c(x,t) \\
\frac{\partial I(x,t)}{\partial x} &= -\kappa_{tr} n_{tr}(x,t) I(x,t) - \kappa_c n_c(x,t) I(x,t) \\
\frac{\partial n_{tr}(x,t)}{\partial t} &= -\frac{\partial n_c(x,t)}{\partial t}
\end{aligned} \tag{1.37}$$

To determine the rate constants of a photoprocess, absorption spectroscopy is the method of choice because it is exact and relatively fast. Absorption spectroscopy measures the reaction

spectrum which is an overlay of spectra recorded at different times during the process (see Fig. 1.9). The full wavelength range of the spectrometer is usually used because it gives more information than a single wavelength measurement. By recording full spectra it is possible to determine points where absorption changes are largest as well as isobestic points, where there is no change in absorption.

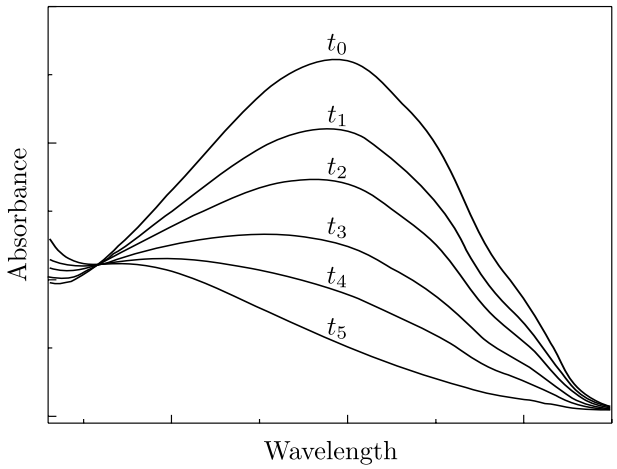

Figure 1.9 *A schematics of a reaction spectrum showing two isobestic points.*

1.3 Nuclear magnetic resonance

The basic requirement for nuclear magnetic resonance (NMR) is that the nucleus has spin different from zero. This is normally the case when either or both the number of protons and the number of neutrons in the nucleus are odd. NMR is a spectroscopic method that measures the absorption of electromagnetic radiation related to magnetic transitions between energy levels of a nucleus. It is therefore important to understand the interactions between the nucleus and its environment which affect the energy levels. The full Hamiltonian of the system is composed of many different interactions [94]:

$$H = H_Z + H_D + H_Q + H_{CS} \tag{1.38}$$

The first term is the Zeeman interaction and is specific for magnetic resonance spectroscopy. Its static part is due to the presence of external magnetic field B_0, whereas dynamic part arises from the oscillating magnetic fields produced by radiofrequency (RF) pulses. The static Zeeman Hamiltonian can be written as a product of the external field and the magnetic moment of the nucleus:

$$H_Z = \mu B_0 = -\gamma \hbar m B_0 \tag{1.39}$$

The gyromagnetic ratio is denoted by γ and the magnetic quantum number by m. The possible values for magnetic quantum number are $m = -I, -I+1, ..., I$ where I is the spin of the nucleus. According to the selection rules the only possible transitions are those that change the magnetic quantum number by one. These transitions are induced by RF pulses at Larmor frequency ω_L that can be determined from Eq. (1.39) by taking into account that $\Delta m = 1$ and $\Delta H_Z = \hbar \omega_L$:

$$\omega_L = \gamma B_0 \tag{1.40}$$

The other contributions to the Hamiltonian in Eq. (1.38) are found in rigid nonmetallic solids. H_D is the dipole-dipole interaction between spins, H_Q the interaction of nuclear quadrupole

moment with electric field gradients and H_{CS} the chemical shift produced by electron shielding effects. However, all the interactions can not be easily deduced from the spectra since some dominate over the others.

Nuclear magnetic resonance is a powerful tool to study the behavior of liquid crystals [95]. One of its key strengths is the possibility to measure molecular orientations. In some cases the order parameter can be directly extracted from the spectrum. In complex geometries, NMR can be used to determine the director configuration [96]. Furthermore, the measurements of molecular dynamics are possible such as the mobility of molecules near the liquid crystal-wall interface.

Usually, protons or deuterons are used as a probe to determine the molecular orientation. The main advantage of using deuteron instead of proton NMR is that the quadrupolar contribution to the energy prevails over the dipolar contribution. Hence, the energy levels are predominantly determined by the orientation of deuterium nucleus under investigation whereas the contributions of the surrounding nuclei can be disregarded. The disadvantage of deuteron NMR is the difficult deuteration process in which the molecule is labeled at a certain position by replacing hydrogen atom with deuterium. In liquid crystals, the hydrogens of the first or second carbon on the aliphatic chain are typically replaced, which is called α or β labeling, respectively. The deuteration has its own advantages. Since the molecule can be selectively labeled at equivalent positions there is only one line in the NMR spectrum. On the contrary, the proton NMR spectrum is a superposition of spectra of all hydrogen atoms in the molecule.

1.3.1 Deuteron NMR spectroscopy

In the case of deuteron NMR spectroscopy, quadrupolar interactions are predominant. The requirement for quadrupole perturbed NMR is a nonzero quadrupole moment of the nucleus. This is the case in nuclei with spin $I \geq 1$. Nuclei with spin 1/2 do not possess quadrupole moment because of their spherical symmetry.

The quadrupolar interaction originates from the coupling between nuclear charge distribution $\rho(\mathbf{r})$ with the surrounding potential $V(\mathbf{r})$. In the classical picture we can write [97]:

$$E = \int \rho(\mathbf{r}) V(\mathbf{r}) d^3r \tag{1.41}$$

This expression can be expanded in terms of nuclear electric moments:

$$E = V(0) \int \rho(\mathbf{r}) d^3r + \sum_{\alpha} V_{\alpha} \int r_{\alpha} \rho(\mathbf{r}) d^3r + \frac{1}{2} \sum_{\alpha,\beta} V_{\alpha\beta} \int r_{\alpha} r_{\beta} \rho(\mathbf{r}) d^3r + \ldots \tag{1.42}$$

The coordinates are denoted by r_{α} where indices $\alpha, \beta = x, y, z$ mark separate components. The derivatives of the potential taken at $\mathbf{r} = 0$ are $V_{\alpha} = \partial V / \partial x_{\alpha}$ but similar expression holds for higher orders $V_{\alpha\beta}$. The first term in the series is simply the charge of the nucleus multiplied by the potential at the center. The second term is the coupling between dipole moment of the nucleus with electric field. However, since nuclei do not have dipole moments this term vanishes. The third term describes the electric quadrupole moment connected with the electric field gradient tensor. This term can be rewritten to include the conventional definition of the quadrupole tensor:

$$Q_{\alpha\beta} = \int \rho(\mathbf{r}) (3 r_{\alpha} r_{\beta} - \delta_{\alpha\beta} r^2) d^3r \tag{1.43}$$

The quadrupolar expression in Eq. (1.42) is therefore:

$$\frac{1}{6} \sum_{\alpha,\beta} V_{\alpha\beta} Q_{\alpha\beta} + \frac{1}{6} \sum_{\alpha} \frac{\partial^2 V}{\partial r_{\alpha}^2} \int r^2 \rho(\mathbf{r}) d^3r \tag{1.44}$$

We should note that electric potential obeys the Laplace equation $\sum_\alpha V_{\alpha\alpha} = 0$. This yields the final form of the classic quadrupole interaction energy:

$$E_Q = \frac{1}{6}\sum_{\alpha,\beta} V_{\alpha\beta} Q_{\alpha\beta} \tag{1.45}$$

The classical expression (1.45) can be transformed to the quantum mechanical by replacing the potential and coordinates with appropriate operators. These operators can be connected to the total angular momentum of the nucleus by applying the Wiegner-Eckart theorem [98]. The following expression for quadrupolar Hamiltonian can be obtained:

$$H_Q = \frac{eQ}{6I(2I-1)}\sum_{\alpha,\beta} V_{\alpha\beta}\left(\frac{3}{2}(I_\alpha I_\beta + I_\beta I_\alpha) - \delta_{\alpha\beta} I^2\right) \tag{1.46}$$

The constant Q is the scalar quadrupole moment of the nucleus and is defined with the matrix element with magnetic quantum number $m = I$:

$$Q = < II | \sum_i 3r_{z,i}^2 - r_i^2 | II > \tag{1.47}$$

The sum is over all the nucleons. The quadrupolar Hamiltonian can be rewritten for the case when principal axes are chosen for the electric field gradient tensor. By using Laplace's equation we obtain:

$$H_Q = \frac{eQ}{4I(2I-1)}\left(V_{zz}(3I_z^2 - I^2) + (V_{xx} - V_{yy})(I_x^2 - I_y^2)\right) \tag{1.48}$$

We are now in a position to describe the spectrum of deuterium labeled molecules in external magnetic field. It is assumed that the EFG tensor has axial symmetry so that $V_{xx} = V_{yy}$. When the principal axis of EFG tensor is tilted toward the direction of the magnetic field by an angle ϑ' the following expression holds for the quadrupole perturbed Hamiltonian:

$$H = -\gamma\hbar m B_0 + \frac{e^2 qQ}{4I(2I-1)}[3m^2 - I(I+1)]P_2(\cos\vartheta') \tag{1.49}$$

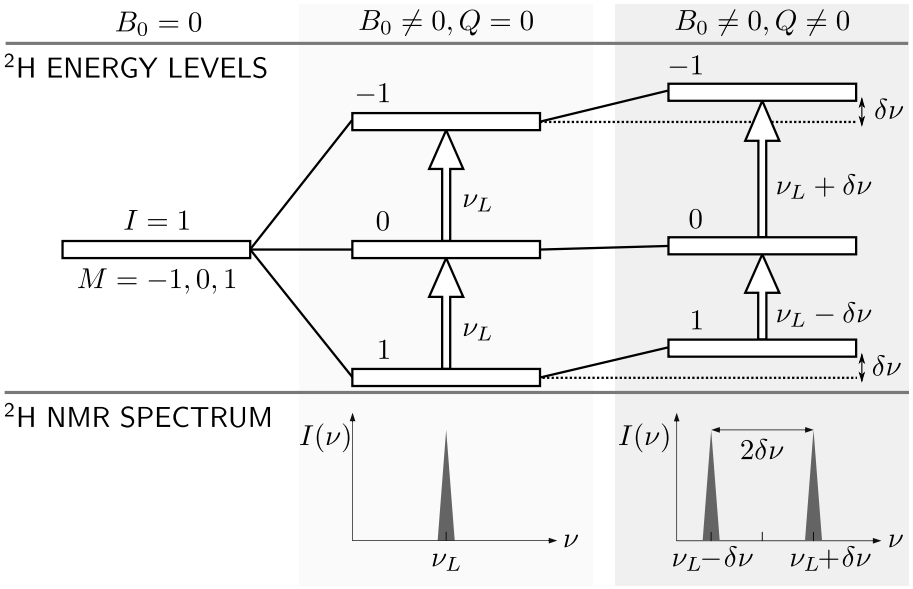

Figure 1.10 *The energy levels and corresponding splitting of quadrupole perturbed deuteron NMR.*

We have introduced the electric field gradient q as $V_{zz} = eq$, whereas the second Legendre polynomial is defined as $P_2(x) = (3x^2 - 1)/2$.

Deuteron is a nucleus with spin $I = 1$ therefore the allowed values of magnetic quantum number m are $-1, 0$ and 1. The energy levels of such system are schematically presented in Fig. 1.10. In the absence of the external magnetic field, the ground state is degenerate. In the magnetic field, the usual Zeeman splitting occurs, proportional to the strength of the magnetic field. However, because of deuteron quadrupole moment, the energy levels are additionally shifted. These shifts change the energy needed for transitions between the levels. In NMR spectrum this is reflected in changed frequencies of the spectral lines. Instead of a single line, a doublet is detected. The quadrupole splitting of the doublet is:

$$\Delta\nu = \frac{3}{2}\nu_Q P_2(\cos\vartheta') \tag{1.50}$$

The constant $\nu_Q = e^2qQ/h$ is the quadrupolar frequency.

1.3.2 Motional averaging

The motion of molecules has significant impact on the NMR spectrum when the timescale of molecular reorientations is fast compared to the NMR timescale. In elongated liquid crystalline molecules, there are two basic movements: the reorientation about the long axis and the reorientation of the long axis of the molecule.

As can be seen from Eq. (1.50) the quadrupolar splitting is affected by the angle between the direction of the magnetic field and the principal axis of the EFG tensor. This axis is in the case of α-deuterated liquid crystalline molecules aligned with the direction of the C-D bond, which is tilted away from the long axis of the molecule. As the molecule reorients about its long axis the C-D bond rotates with it and since the reorientation is fast, the EFG tensor is motionally averaged.

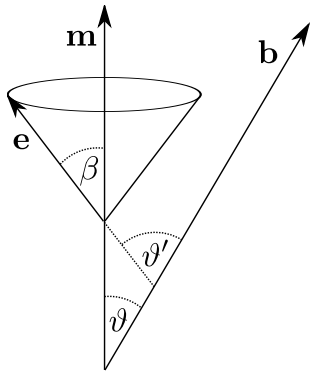

Figure 1.11 *The directions of the magnetic field, the molecular long axis and the principal axis of EFG tensor.*

To describe the motional averaging process we define three unit vectors: **b** that points in the direction of the external magnetic field, **m** which is aligned with the long axis of the molecule and **e** that shows the C-D bond direction and thus the direction of the principal axis of EFG tensor. As is shown in Fig. 1.11, the angle between **b** and **m** is denoted by ϑ, the angle between **b** and **e** by ϑ' and the angle between **m** and **e** by β. By choosing a coordinate system with the z

axis parallel to **m** we can write:

$$\begin{aligned} \mathbf{b} &= (\sin\vartheta, 0, \cos\vartheta) \\ \mathbf{e} &= (\sin\beta\cos\varphi, \sin\beta\sin\varphi, \cos\beta) \\ \cos\vartheta' &= \mathbf{b}\cdot\mathbf{e} \end{aligned} \tag{1.51}$$

The reorientation of the molecule is described by angle φ. The averaging of $P_2(\cos\vartheta')$ over φ yields a new expression for the line splitting:

$$\Delta\nu = \frac{3}{2}\nu_Q P_2(\cos\beta)P_2(\cos\vartheta) = \frac{3}{2}\overline{\nu}_Q P_2(\cos\vartheta) \tag{1.52}$$

Since the tilt of the bond β does not vary for the same type of molecule it can be treated as constant and included in the average quadrupole frequency $\overline{\nu}_Q$. For the C-D bond the coefficient $P_2(\cos\beta)$ is approximately $1/3$ and the typical measured quadrupolar constant $\overline{\nu}_Q$ is about 60 kHz.

The other type of motion, reorientation of the long axis is related to the order parameter of the nematogen. This can be seen by rewriting Eq. (1.52) into:

$$\Delta\nu = \frac{3}{2}\overline{\nu}_Q\frac{1}{2}[3(\mathbf{m}\cdot\mathbf{b})^2 - 1] = \frac{3}{4}\overline{\nu}_Q(3\sum_{\alpha,\beta} m_\alpha b_\alpha m_\beta b_\beta - 1) \tag{1.53}$$

The correct frequency splitting is obtained by averaging the product $m_\alpha m_\beta$ over the positions of the reorienting long axis. Expression $< m_\alpha m_\beta >$ was used in the definition of the order parameter (1.2). By substituting into above equation we obtain:

$$\Delta\nu = \frac{3}{2}\overline{\nu}_Q\sum_{\alpha,\beta} Q_{\alpha\beta} b_\alpha b_\beta \tag{1.54}$$

In the eigenframe of the order parameter tensor the off-diagonal elements are zero. In such case the direction of the magnetic field can be described by Eq. (1.51). This allows us to calculate the line splitting for the case of uniaxial nematic material in terms of the scalar order parameter, i.e. the nematic order parameter S:

$$\Delta\nu = \frac{3}{2}\overline{\nu}_Q S P_2(\cos\vartheta) \tag{1.55}$$

The equation above is important because it provides for the measurement of order parameter and director alignment of liquid crystals.

1.3.3 Influence of director distribution on the NMR spectra

The spectrum of the isotropic phase is completely averaged. The order parameter is zero and instead of nematic doublet, a single central line is obtained. The reorientational movement of the molecules in the nematic phase is limited to a relatively small angles around the director which causes two spectral lines according to Eq. (1.55). In these two cases the order parameter and the director are uniform throughout the medium.

When there is a nonuniform director field, the line splitting varies in space since the angle between the director and external magnetic field is changing. However, the NMR spectrum is a sum of signals from all parts of the sample which gives rise to different spectral patterns.

The simplest angular distribution of molecules is isotropic and produces a powder pattern. In contrast to the isotropic phase, the molecules are not allowed to move which occurs for example

in a frozen liquid crystal. To calculate the spectral distribution the angular distribution has to be known. In the isotropic case, the probability of finding a molecule oriented in a solid angle $d\Omega$ is constant:

$$\frac{dP}{d\Omega} = \frac{1}{4\pi} \tag{1.56}$$

The spectral distribution can now be determined through the use of the following relation:

$$\frac{dP}{d\nu} = \frac{dP}{d(\cos\vartheta)} \left| \frac{d\nu}{d(\cos\vartheta)} \right|^{-1} \tag{1.57}$$

The last derivative is obtained by using Eq. (1.50) which yields the final expression:

$$\frac{dP}{d\nu} = \frac{4}{3} \sqrt{\frac{1}{\nu_Q(8\nu + 3\nu_Q)}} \tag{1.58}$$

The powder pattern was calculated as an example of a simple angular distribution. However, a variety of spectral patterns can be obtained by using more complex director distributions. Especially in confined geometries, these patterns are important because they help in determining the director configuration inside the cavities. The spectral patterns for different director configurations inside cylindrical pores are shown in Fig. 1.12. They can be simulated using similar equations as for the powder pattern if the angular distribution is known. When trying to determine the director field experimentally, it is useful to rotate the sample since this changes the spectral pattern. It is thus possible to obtain a doublet when the pore axis is parallel and a radial pattern when the pore axis is perpendicular to the external magnetic field.

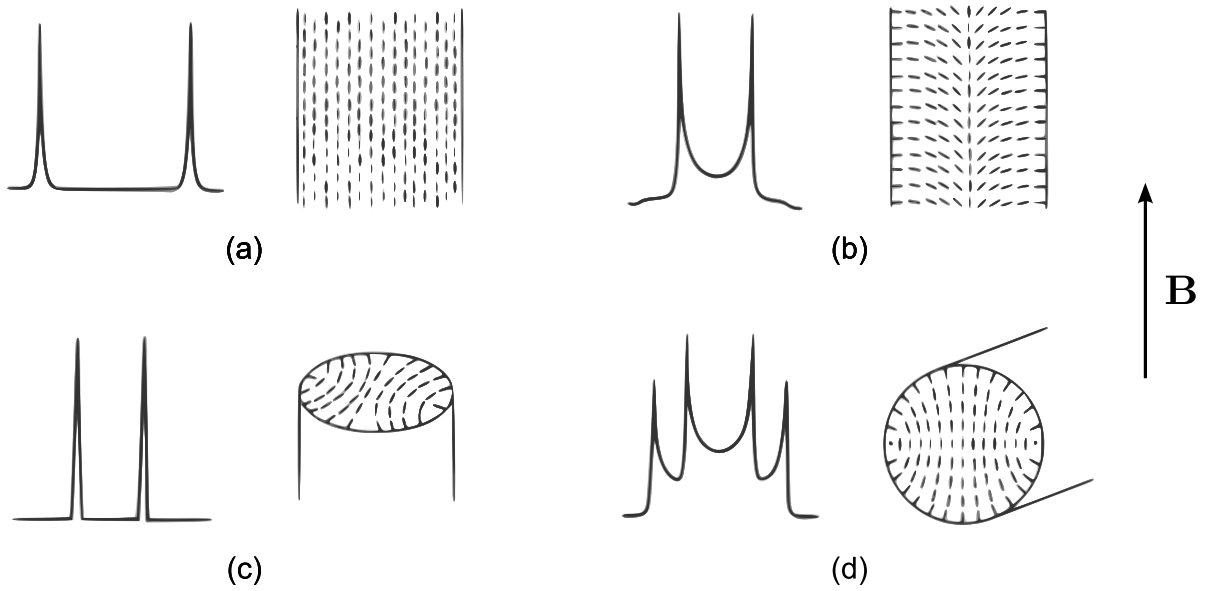

Figure 1.12 *The calculated spectral patterns corresponding to different director configurations and pore orientations. The axial configuration produces normal bulk line splitting (a). When all the molecules are perpendicular to the magnetic field* **B** *half the bulk splitting is observed (c). More complicated patterns can be found in complex director fields such as escaped radial (b) and planar polar with pore axis perpendicular to the field (d).*

2 Theory

The phase separation behavior and the order parameters of mesomorphic materials in binary mixtures can be successfully predicted by combining the theories for isotropic mixing and orientational ordering. We present here a model based on the Landau-de Gennes theory. First, a general introduction to the required theoretical background is given, followed by the derivation of our model. We have obtained the final theoretical predictions by extending the Landau-de Gennes model to include the varying concentration of cis molecules.

2.1 Theoretical background

2.1.1 Free energy of isotropic mixing

The free energy of mixing is composed of two parts as can be seen from the following well known expression:

$$F = U - T\Sigma \tag{2.1}$$

The first term is internal energy due to the interaction between constituent molecules whereas the second is the entropic contribution.

The increase in entropy is due to the change of the available volume per particle. For a solution of two species of similar size, one can consider that the molecules are arranged on a lattice, each occupying the same volume. The total number of molecules is $N = N_A + N_B$ and the number of possible states is $\Omega = N!/N_A!N_B!$ which allows for the calculation of the entropy using the Boltzmann equation:

$$\Sigma = -k \ln \Omega \tag{2.2}$$

The number of states Ω can be simplified by using Stirling approximation for large numbers $\ln N! = N \ln N - N$. By introducing the concentration of one component $\phi = V_A/V = N_A/N$ we obtain the final expression for the entropy of mixing:

$$\Sigma(\phi) = -k[\phi \ln \phi + (1-\phi)\ln(1-\phi)] \tag{2.3}$$

As expected, the entropy of mixing is zero when there is only one component ($\Sigma(0) = \Sigma(1) = 0$) and is maximum when there is equal amount of both components ($\phi = 1/2$).

There are three contributions to the energy term of Eq. (2.1). The interspecies interactions are described by interaction parameters W_{AA} and W_{BB} for type A and B molecules, respectively, whereas the interplay between dissimilar molecules is described by W_{AB}. The total energy per molecule is thus:

$$U = \frac{1}{2}[W_{AA}\phi^2 + W_{BB}(1-\phi)^2 + 2W_{AB}\phi(1-\phi)] \tag{2.4}$$

To obtain the change in energy due to mixing, the energies $U(\phi = 0)$ and $U(\phi = 1)$ have to be subtracted. This yields the following expression:

$$\begin{aligned} \Delta U &= U - \phi U(1) - (1-\phi)U(0) = U_0\phi(1-\phi) \\ U_0 &= W_{AB} - \frac{1}{2}(W_{AA} + W_{BB}) \end{aligned} \tag{2.5}$$

The energy of mixing can be described by a single interaction parameter U_0. When there is little interspecies interaction, the mixture is in a good-solvent regime as opposed to poor-solvent regime when there are strong attractive forces. Formally, the good-solvent regime occurs when $U_0 < kT/2$ and poor-solvent regime when $U_0 > kT/2$.

Equations (2.3) and (2.5) can be inserted into (2.1) to calculate the free energy of mixing per molecule. The dimensionless form of the equation is:

$$F_{mix} = \frac{kT}{U_0}[\phi \ln \phi + (1-\phi)\ln(1-\phi)] + \phi(1-\phi) \tag{2.6}$$

It should be noted that this is the free energy of isotropic mixing since only the isotropic part of the interactions is taken into account with parameter U_0. To fully describe the mixing of nematic materials, expanded model must be used which also takes into account the nematic ordering.

2.1.2 Maier-Saupe model

A generally accepted mean field theory that describes the nematic ordering is the Maier-Saupe model. It is based on the assumption about the anisotropic potential between liquid crystalline molecules. The interactions are of the Van der Waals type, therefore the pairwise potential between the molecules whose centers of mass are located at $\mathbf{r}$ and $\mathbf{r}'$ can be written as:

$$V_{rr'} \propto \frac{P_2(\cos\beta)}{|\mathbf{r}-\mathbf{r}'|^6} \tag{2.7}$$

The angle between the long axes of the molecules is denoted by β and P_2 is the second Legendre polynomial. In the mean field approximation, the intermolecular potential is averaged over all the molecules which yields the effective potential for a molecule tilted at an angle ϑ from the average direction $\mathbf{n}$:

$$V(\vartheta, S) = -V_0 S P_2(\cos\vartheta) \tag{2.8}$$

As usual, the nematic order parameter is denoted by S and V_0 is the interaction parameter.

Once the potential is known, the formalism of statistical mechanics can be used to calculate the nematic free energy according to (2.1). The probability distribution function is:

$$f(\vartheta, S) = \frac{1}{Z} e^{-\frac{V(\vartheta,S)}{kT}} \tag{2.9}$$

The partition function is denoted by Z. The average value of a variable x can then be calculated as:

$$< x >= \int_0^{2\pi} d\varphi \int_0^{\pi} x f(\vartheta, S) \sin\vartheta d\vartheta \tag{2.10}$$

In order not to double-count the intermolecular interactions, the resulting internal energy is divided by two:

$$U = -\frac{1}{2} V_0 S^2 \tag{2.11}$$

When determining the decrease in entropy due to orientational ordering no such correction factor is necessary. The expression obtained is:

$$\Sigma = -\frac{V_0 S^2}{T} - k \ln \frac{4\pi}{Z} \tag{2.12}$$

By combining equations (2.11) and (2.12) the nematic free energy is obtained:

$$F = \frac{1}{2}V_0 S^2 + kT \ln 4\pi Z \tag{2.13}$$

Thermodynamic equilibrium of the system corresponds to minimum free energy. The order parameter can thus be calculated by minimization of Eq. (2.13). From equation $\partial F/\partial S = 0$ the final result of the model is represented as a self-consistent equation for the nematic order parameter S:

$$S = 2\pi \int_0^{\pi} P_2(\cos\vartheta) f(\vartheta, S) \sin\vartheta d\vartheta \tag{2.14}$$

The calculation of $S(T)$ is performed by recursively inserting S into effective potential (2.8) which in turn is used to calculate the next approximation of S. At the phase transition temperature this leads to an universal value of the order parameter $S = 0.43$.

The main advantage of Maier-Saupe theory is that it can be easily extended to cover the mixtures of nematic materials [99, 100]. The volume fractions of the materials have to be included in the free energy expression (2.13). Furthermore, the interaction parameter V_0 is different for each component and interaction parameters between species have to be added. In case of a binary mixture there are three parameters: U_{AA}, U_{BB} and U_{AB}. The volume fraction of the first component is ϕ and of the second component $1-\phi$. This leads to the following expression:

$$F = -T\Sigma_A\phi - T\Sigma_B(1-\phi) - \frac{1}{2}U_{AA}S_A^2\phi^2 - \frac{1}{2}U_{BB}S_B^2(1-\phi)^2 - U_{AB}S_AS_B\phi(1-\phi) \tag{2.15}$$

It is important to note that the two components can have different order parameters S_A and S_B. Since the entropy depends on the orientational order, this results in different entropies Σ_A and Σ_B. The entropy changes linearly with the volume fraction. On the contrary, the terms that describe interaction between two molecules scale quadratically with the volume fraction. The entropy of each component can be calculated according to Eq. (2.12). The order parameters can then be obtained by minimizing the free energy:

$$\begin{aligned} \frac{\partial F}{\partial S_A} &= 0 \\ \frac{\partial F}{\partial S_B} &= 0 \end{aligned} \tag{2.16}$$

The minimization results in a set of coupled self-consistent equations for $S_A(T)$ and $S_B(T)$. Once the order parameters are known the free energy can be calculated by using expression (2.15).

2.1.3 Landau-de Gennes model

The confinement of liquid crystals results in a surface-induced order above the nematic-isotropic transition, a scenario not addressed in the original Maier-Saupe model. Some attempts to include the ordering above the transition have already been made [51]. However, a better approach is to use the Landau-de Gennes theory.

The free energy density calculated using the Landau-de Gennes approach was introduced in Eq. (1.13). However, for an adequate theoretical reproduction of the experimentally determined $S(T)$ at temperatures several K below T_{NI}, the free energy needs to be expanded up to the S^6 term:

$$F = \frac{a}{2}(T - T^*)S^2 - \frac{B}{3}S^3 + \frac{E}{6}S^6 \tag{2.17}$$

This is an alternative formulation of the nematic-to-isotropic transition with $C = D = 0$ [101]. This form proved to be more appropriate to the specific case of 7AB isotropic-nematic transition than the conventional formulation with $D = E = 0$.

Expression (2.17) describes the free energy per molecule divided by U_0 and can be directly compared to the energy of mixing (2.6). Parameters B and E are dimensionless whereas a has units K^{-1}. The value of the order parameter can be determined by the usual free energy minimization $\partial F/\partial S = 0$. The nematic to isotropic transition temperature is calculated to be:

$$T_{NI} = T^* + \frac{1}{4a}\sqrt[3]{\frac{4B^4}{E}} \tag{2.18}$$

In order to calculate the surface-induced order of a confined liquid crystal, a more general form of Landau-de Gennes free energy density is used, allowing for spatially dependent order parameter [8]:

$$f = \frac{a'}{2}(T - T^*)S(r)^2 + \frac{L'}{2}\left(\nabla S(r)\right)^2 - G'S(r)\delta(r - R) \tag{2.19}$$

The expression is adapted to cylindrical geometry of cavities found in e.g. Anopore and Nucleopore membranes, where r measures the distance from the center and R the radius of the pore. The elastic constant is denoted by L' and the surface coupling constant by G'. The parameters are marked by primes since they describe the free energy density and not the dimensionless free energy per molecule. We have neglected the terms higher than S^2 since the surface-induced order parameter in the isotropic phase is normally rather small.

The full free energy is obtained by integrating expression (2.19) over the volume of the sample:

$$F = \int_{(V)} f(S, \nabla S, r)dV \tag{2.20}$$

It is straightforward to observe that the free energy has the form of a functional, thus it can be minimized by using the Euler-Lagrange equations. The equilibrium order parameter function $S(r)$ calculated in cylindrical geometry is therefore:

$$S(r) = S_0\frac{J_0(ir/\xi)}{J_0(iR/\xi)} \tag{2.21}$$

The order parameter at the surface of the pore is S_0, J_0 is the Bessel function of the first kind and ξ is the characteristic length defined as:

$$\xi = \sqrt{\frac{L'}{a'(T - T^*)}} \tag{2.22}$$

Furthermore, it can be assumed that there is a thin layer of molecules with thickness r_0 and constant order parameter S_0 at the surface [46]. This leads to a slightly different form of Eq. (2.21) where R has to be replaced by $R - r_0$.

When NMR spectroscopy is used to measure the order parameter, the signal is a superposition of contributions from all molecules in the sample. During the measurement, the molecules diffuse around the sample. At different distances from the center r, the molecules experience different ordering $S(r)$ which would be measured as a superposition of different frequency splittings $\Delta\nu(r)$.

However, on the characteristic timescale of a NMR experiment, typically few milliseconds, the path of the molecules in radial direction is larger than the pore size. The measured frequency splitting is thus completely averaged out. This can be seen by calculating the average square of the path of molecules in time τ, which is $< x^2 >= 6D\tau$ with the diffusion constant characteristic for the isotropic phase $D = 10^{-10}$ m^2/s. Consequently, the radial dependence of the order parameter must be averaged across the pore cross-section:

$$< S >= \frac{2}{R^2}\int_0^{R-r_0} S(r) r dr + \frac{2}{R^2}\int_{R-r_0}^{R} S_0 r dr \tag{2.23}$$

2.2 Theoretical predictions

By combining the theories of isotropic mixing, nematic ordering and surface-induced ordering we are able to derive an appropriate model for the phase separation behavior of confined photoisomerizable liquid crystal. The free energy of such system can be written as a sum of three components:

$$F = F_{mix} + F_{nem} + F_{surf} \tag{2.24}$$

The free energy of isotropic mixing F_{mix} can be written according to Eq. (2.6) where the concentration (volume fraction) of cis molecules is represented by ϕ and the concentration of trans molecules by $1-\phi$. The last term F_{surf} is the free energy needed to determine the surface-induced ordering in the isotropic phase. However, since the surface-induced order parameter is close to zero, the F_{surf} term is small compared to the other two terms. When modeling the phase separation behavior where the full free energy is needed, the F_{surf} term can be neglected.

2.2.1 Order in bulk nematic binary mixture

To derive the nematic part of the free energy F_{nem} one has to note that the Maier-Saupe free energy (2.13) can be expanded in terms of S. In this way, an expression similar to Landau-de Gennes free energy can be obtained. Expansion to the fourth order gives:

$$F = \frac{V_0}{10}\left(5 - \frac{V_0}{kT}\right)S^2 - \frac{V_0^3}{105(kT)^2}S^3 + \frac{V_0^4}{700(kT)^3}S^4 \tag{2.25}$$

By comparing the two expressions we see that the term quadratic in S includes both the internal energy and entropy while the terms with higher powers describe the entropic part of the free energy. This allows us to modify the Landau-de Gennes free energy expression (2.17) to include the varying number of cis molecules. The derivation is completely analogous to the modification of Maier-Saupe free energy in Eq. (2.15). The energy scales quadratically with the concentration whereas the entropy is linear to the concentration. By denoting the cis component with index c and the trans component with index t, the nematic free energy can be written in the form:

$$\begin{aligned} F_{nem} &= -\frac{U_{cc}}{2}S_c^2\phi^2 + \left(\frac{a_c}{2}(T-T_c^*)S_c^2 + \frac{U_{cc}}{2}S_c^2 - \frac{B_c}{3}S_c^3 + \frac{E_c}{6}S_c^6\right)\phi - U_{ct}\phi(1-\phi)S_cS_t - \\ &\quad -\frac{U_{tt}}{2}S_t^2(1-\phi)^2 + \left(\frac{a_t}{2}(T-T_t^*)S_t^2 + \frac{U_{tt}}{2}S_t^2 - \frac{B_t}{3}S_t^3 + \frac{E_t}{6}S_t^6\right)(1-\phi) \end{aligned} \tag{2.26}$$

We have derived the most general Landau-de Gennes expression for a mixture of two nematic materials. The free energy was divided into two parts describing the energy and the entropy

of the system. The anisotropic interaction parameters between trans and cis molecules are U_{tt} and U_{cc}, respectively. The parameter U_{ct} describes the interspecies interaction. It has to be noted that in the limit when either $\phi = 0$ or $\phi = 1$, the standard Landau-de Gennes expression is obtained, i.e. the terms with U_{tt}, U_{cc} and U_{ct} vanish. In the intermediate region $0 < \phi < 1$, the temperature T^* is effectively modified for both species which changes the calculated order parameters depending on the concentration ϕ.

The order parameters of both components, S_t and S_c, can be determined by solving a system of equations:

$$\begin{aligned} -U_{cc}S_c\phi^2 + \left(a_c(T-T_c^*)S_c + U_{cc}S_c - B_cS_c^2 + E_cS_c^5\right)\phi - U_{ct}\phi(1-\phi)S_t = 0 \quad (2.27)\\ -U_{tt}S_t(1-\phi)^2 + \left(a_t(T-T_t^*)S_t + U_{tt}S_t - B_tS_t^2 + E_tS_t^5\right)(1-\phi) - U_{ct}\phi(1-\phi)S_c = 0 \end{aligned}$$

Within this model, the cis component of the mixture is treated as a nematic material with very low phase transition temperature. In practice, such material crystallizes before reaching the nematic phase.

A plot of the concentration dependence of order parameters for a set of typical parameters is given in Fig. 2.1. The multiple lines for trans and cis component were obtained by varying the interaction parameter U_{ct}. Expressions (2.27) show that it is solely U_{ct} term that couples both equations. If it were zero, then S_c and S_t could be calculated separately. As can be seen from Fig. 2.1, the increase or decrease of this coupling strength strongly influences the order of the cis molecules but has insignificant impact on the order of trans molecules. The temperature used in the calculation was 308 K, however, the main characteristics of the plot do not change with the temperature. We thus conclude that for an adequate description of the ordering of trans isomers, the ordering of cis molecules can be ignored by setting $S_c = 0$. In the following, cis molecules will be treated as an isotropic solute that influences the trans ordering solely due to changes in concentration ϕ.

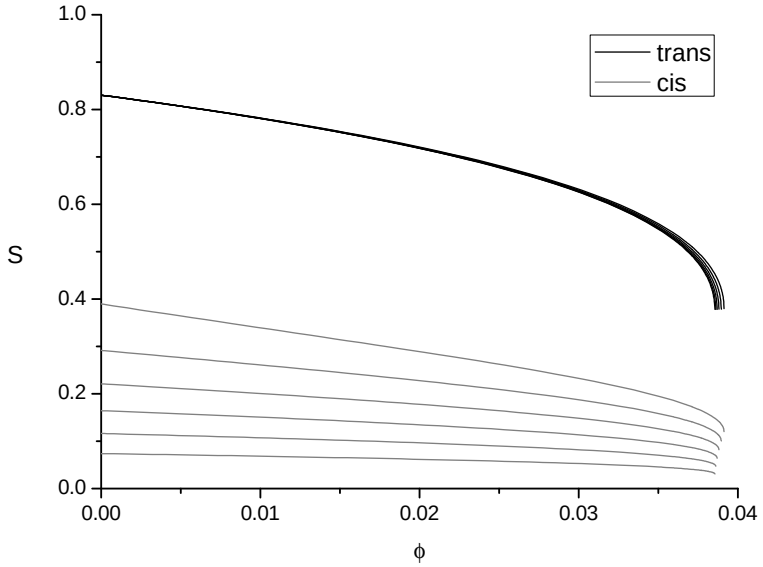

Figure 2.1 *Trans and cis nematic order parameters at* 308 *K. The interaction parameters are* $U_{tt} = 6.9$ *and* $U_{cc} = 0.1$. U_{ct} *was varied from* 0.1 *to* 0.35 *in* 0.05 *steps. All other parameters were similar to the data found in the literature (see table 1.1).*

2.2.2 Order in binary mixture with one nematic component

When only one component of a binary mixture is nematic, the calculation of $S(T)$ profile is straightforward. Eq. (2.26) can be rewritten by inserting $S_c = 0$ as discussed in the previous section. The nematic free energy is then:

$$F_{nem} = -\frac{U}{2}S^2(1-\phi)^2 + \left(\frac{a}{2}(T-T^*)S^2 + \frac{U}{2}S^2 - \frac{B}{3}S^3 + \frac{E}{6}S^6\right)(1-\phi) \tag{2.28}$$

The indices were omitted since all the parameters correspond to the trans component. The minimization of the free energy yields an analytical expression for the nematic order parameter:

$$\begin{aligned} S(T,\phi) &= \frac{1}{2}\left(\sqrt{X_1} + \sqrt{\frac{2B}{E\sqrt{X_1}} - X_1}\right) \\ X_1 &= \sqrt[3]{2/3}\frac{4(a(T-T^*)+U\phi)}{X_2} + \frac{X_2}{\sqrt[3]{18}E} \\ X_2 &= B^2E\left(9 + \sqrt{81 - 256(a(T-T^*)+U\phi)E/B}\right) \end{aligned} \tag{2.29}$$

The nematic to isotropic transition temperature can be written as:

$$T_{NI} = T^* + \frac{1}{4a}\sqrt[3]{\frac{4B^4}{E}} - \frac{U\phi}{a} \tag{2.30}$$

2.2.3 Surface-induced order in confined binary mixture

The surface-induced order parameter of the trans isomer can be calculated by extending Eq. (2.19) to cover the case of a trans-cis mixture. In analogy to expression (2.28) we can write:

$$\begin{aligned} f &= \left(\frac{U'}{2}S(r)^2 + \frac{a'}{2}(T-T^*)S(r)^2 - G'S(r)\delta(r-R)\right)(1-\phi) + \\ &+ \left(\frac{L'}{2}(\nabla S(r))^2 - \frac{U'}{2}S(r)^2\right)(1-\phi)^2 \end{aligned} \tag{2.31}$$

There are two new terms compared to Eq. (2.28) which describe the elastic energy between the molecules (L') and the molecule wall interaction (G'). The latter is proportional to the concentration while the former scales as $(1-\phi)^2$.

The total free energy is obtained by integrating over the volume. Eq. (2.20) yields:

$$\begin{aligned} F_{surf} &= \left(\frac{a}{2}(T-T^*)(1-\phi) + \frac{U}{2}(1-\phi) - \frac{U}{2}(1-\phi)^2\right) < S^2 > + \\ &+ \frac{L}{2}(1-\phi)^2 < \nabla S^2 > - GS_0(1-\phi) \end{aligned} \tag{2.32}$$

The average values are denoted by angle brackets. The following holds:

$$\begin{aligned} < S^2 > &= \frac{2}{R^2}\int_0^R S(r)^2 r\,dr \\ < \nabla S^2 > &= \frac{2}{R^2}\int_0^R (\nabla S(r))^2 r\,dr \end{aligned} \tag{2.33}$$

It should be noted that primes are not used to denote the parameters because new parameters describe the free energy while the old ones were used in the expression for free energy density. Since expression (2.32) is the dimensionless free energy per molecule the conversion between a and a' is simply $a = a'V/(U_0N)$ and similar for other parameters. V is the total volume of the sample, N the total number of molecules and U_0 the isotropic interaction parameter from Eq. (2.6). The parameters used in equations (2.6), (2.28) and (2.32) are therefore the same.

The order parameter dependence in the radial direction determined by Euler-Lagrange equation is:

$$S(r) = S_0 \frac{J_0(i\tilde{r}/\tilde{\xi})}{J_0(i(1-\tilde{r}_0)/\tilde{\xi})} \tag{2.34}$$

Eq. (2.21) was rewritten to include dimensionless variables $\tilde{r} = r/R$, $\tilde{r}_0 = r_0/R$ and $\tilde{\xi} = \xi/R$. Furthermore, it was modified to include the surface layer with the constant order parameter S_0. In contrast to expression (2.22), the dimensionless $\tilde{\xi}$ now depends on the concentration:

$$\tilde{\xi} = \sqrt{\frac{1-\phi}{R_1(T-T^*)+R_2\phi}} \tag{2.35}$$

Two new parameters were added: $R_1 = aR^2/L$ and $R_2 = UR^2/L$. Their ratio is completely determined by a and U, $R_1/R_2 = a/U$.

The radial dependence of the order parameter at different concentrations is shown in Fig. 2.2. Once $S(r)$ is known it is possible to predict the results of the measurements by averaging according to (2.23). The average order parameter that can be measured by NMR is:

$$< S >= S_0 \left(2\tilde{r}_0 - \tilde{r}_0^2 + 2\tilde{\xi}(1-\tilde{r}_0)\frac{I_1((1-\tilde{r}_0)/\tilde{\xi})}{I_0((1-\tilde{r}_0)/\tilde{\xi})} \right) \tag{2.36}$$

I_0 and I_1 are modified Bessel functions of the first kind, $I_n(x) = i^{-n}J_n(ix)$.

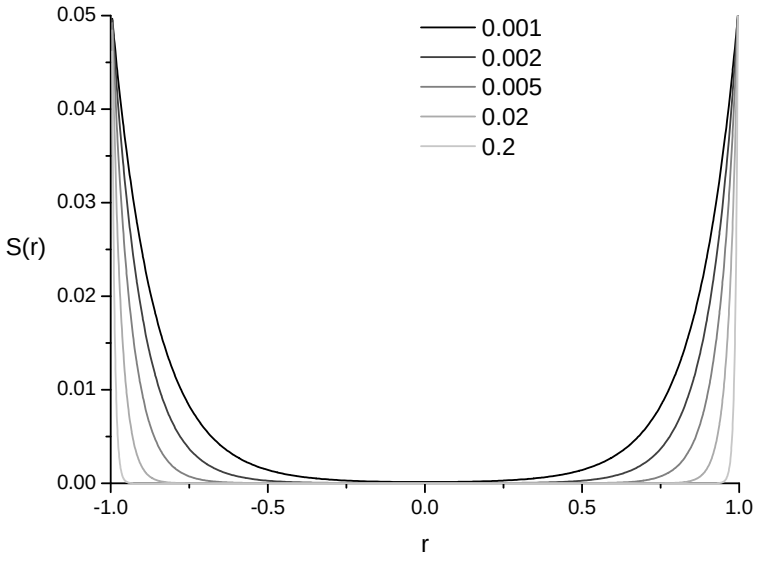

Figure 2.2 *Typical order parameter profiles inside a cylindrical cavity. The simulated temperature was fixed at* 319 *K while the concentration of cis molecules was varied from* 0.001 *to* 0.2.

2.2.4 Phase separation

At certain concentrations of cis isomers, it is energetically more favorable for the system to form two coexistent phases. In our case, isotropic and nematic phases can be in equilibrium when their chemical potentials match:

$$\begin{aligned} \mu_t^I &= \mu_t^N \\ \mu_c^I &= \mu_c^N \end{aligned} \tag{2.37}$$

The phase separation criteria can be most easily determined by plotting the total free energy (2.24) as a function of the concentration at the selected fixed temperature (see Fig. 2.3). When there exists a double tangent, connecting two points with concentrations ϕ_1 and ϕ_2, phase separation will occur. The condition for the bitangent to exist is:

$$\begin{aligned} F'(\phi_1) &= F'(\phi_2) \\ F(\phi_1) - \phi_1 F'(\phi_1) &= F(\phi_2) - \phi_2 F'(\phi_2) \end{aligned} \tag{2.38}$$

The set of equations (2.38) has to be solved numerically due to the complicated expression for the nematic order parameter (2.29).

Concentrations ϕ_1 and ϕ_2 are cis concentrations in cis-poor and cis-rich phase respectively and x is the volume fraction of nematic phase. In the coexistence region where $\phi_1 < \phi < \phi_2$ the following holds:

$$\phi = \phi_1 x + \phi_2 (1 - x) \tag{2.39}$$

When the total cis concentration ϕ is changing due to either photoisomerization or thermal backisomerization, only the ratio between the phases changes, whereas the concentrations ϕ_1 and ϕ_2 remain constant. In this region, the order parameters in both phases should remain constant as well.

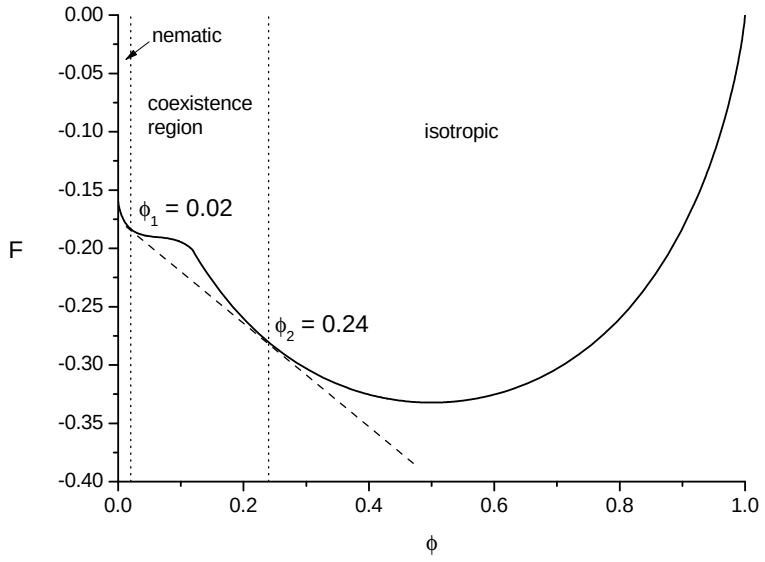

Figure 2.3 *Characteristic plot of free energy vs. concentration at a fixed temperature. Dashed line is a bitangent that determines the limiting concentrations ϕ_1 and ϕ_2 of the two phases in coexistence.*

3 Materials and methods

3.1 Diheptylazobenzene

The liquid crystalline material used in the study was diheptylazobenzene (7AB). The material has bulk nematic-to-isotropic transition point at 320.2 K and a melting point at 313.2 K [102]. However, supercooling of 7AB is possible down to about 300 K. The compound was custom synthesized and was deuterium labeled at alpha position to allow for deuteron NMR measurements.

The nematic phase of 7AB disappears when the sample is irradiated with UV light. This is due to trans-to-cis photoisomerization. At high cis concentrations, the material remains in the isotropic phase even at room temperatures. There seems to be no published data about the 7AB absorption peaks. However, for azobenzene solutions in isooctane, a typical trans-to-cis photoisomerization wavelength is 313 nm whereas backisomerization is strongest at 436 nm [103]. The structure of both trans and cis isomers is shown in Fig. 3.1.

For measurements of bulk samples, the material was put in a cuvette with 4 mm outer diameter and approximately 3 mm inner diameter. The length of the cuvette was 25 mm but the sample occupied only about 14 mm. The cuvette was made of quartz which is adequately transparent for light in the UV region. The sample was sealed with a two-component epoxy.

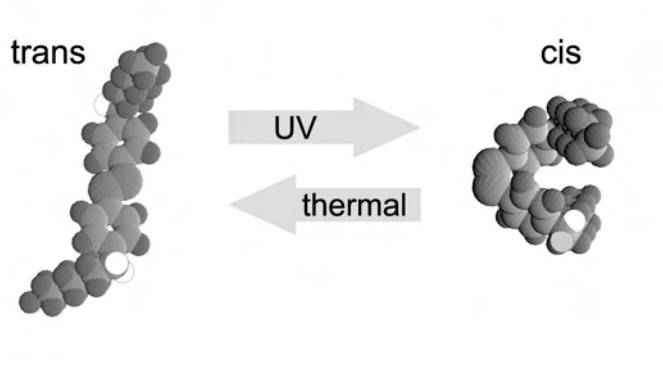

Figure 3.1 *Trans isomer of 7AB is converted to cis form with UV light. The backisomerization process can be photoinduced with a different wavelength of illumination, but thermal relaxation is also possible. Deuterium atoms are marked in white.*

3.2 Anopore membranes

To confine liquid crystalline material, a suitable substrate is needed. Anopore inorganic membranes are a good choice because they are made from high purity alumina and are commercially available. They are primarily intended for use in laboratory filtration applications. According to the specifications, the pores have a relatively well-defined cylindrical geometry, are almost

perfectly parallel and there is no lateral crossover between individual pores. The membranes are available in three different nominal pore sizes: 0.02 μm, 0.1 μm and 0.2 μm. The average thickness of a membrane is 60 μm and porosity from 25 to 50%.

In deuteron NMR studies, the exact geometry of pores is important. That is why we examined the membrane structure using scanning electron microscopy (SEM). The measurements confirmed previous results [104] which showed that the pores are asymmetrical (Fig. 3.2a and 3.2b). The cross-sections of the membranes are shown in Fig. 3.2c and 3.2d. The pores are effectively parallel tubes with a rather constant diameter along all of their length. Only at one end, the pores get narrower. Furthermore, the diameter of the pores is equal for different membrane types. From the point of view of NMR measurements, membranes of all available pore sizes are thus equivalent.

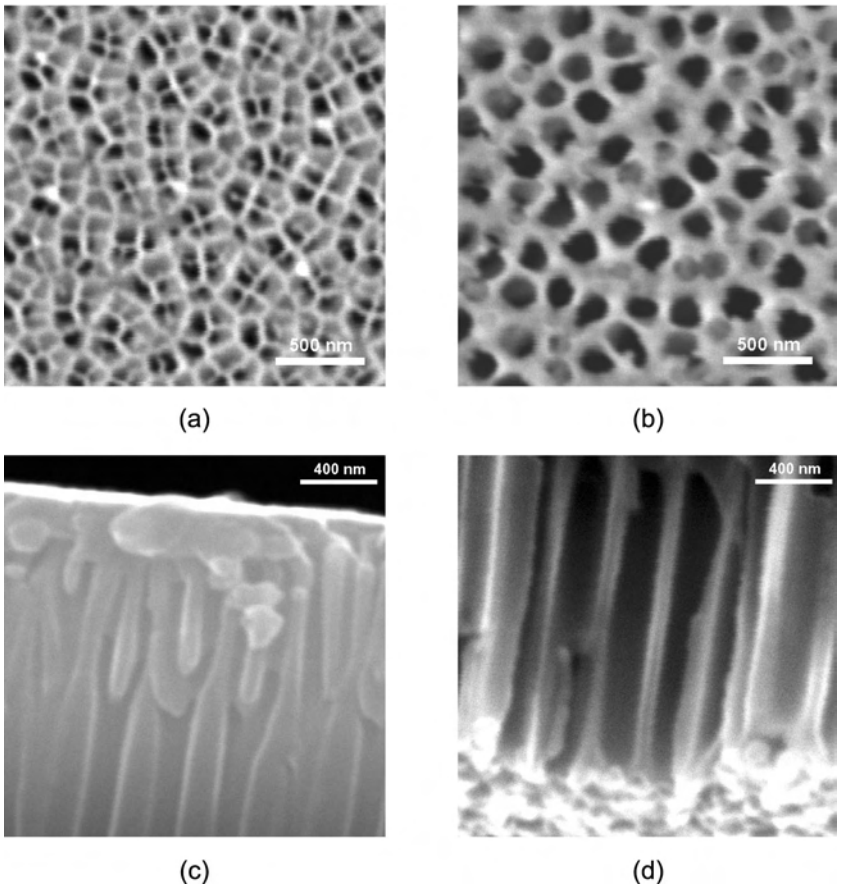

Figure 3.2 *SEM images of front (a) and back (b) side of Anopore membrane. The different structure at both ends is evident by looking at the cross sections (c) and (d). The pores are narrow only at one end.*

The original membranes are disc shaped and few centimeters in diameter. In order to fit them into small NMR coils, membranes had to be cut into approximately 4×5 mm pieces using a razor blade. Cut membranes were then filled with 7AB on a hotplate at around 350 K. This ensured that the liquid crystal was completely in the isotropic phase during the filling. Excess material was wiped off the surface of the membrane using nonabrasive low-lint wipers.

In order to provide for a complete photoisomerization of the whole sample, only a single piece of Anopore membrane was used for most measurements. To exclude effects due to atmosphere changes, the filled membrane was sealed in a glass cell using a standard two-component epoxy.

3.3 Wedge cells

The measurements of absorbance of photoisomerizable materials in a solution are straightforward. We used a standard quartz cuvette with 1 cm optical path length. Since a very small amount of absorbing material was dissolved in cyclohexane, the absorbance was low enough to be measured by a standard spectrophotometer. This is not the case when measurements of absorption in bulk 7AB are required. Thick samples absorb all the light and only at very short optical path lengths the measurements are possible. This is why wedge cells were built and the penetration depth of UV light in 7AB samples was determined.

Wedge cells were constructed from two 0.5 mm thick quartz slides with dimensions 18 $\times$ 10 mm. One slide was put on top of the other while at one end the spacing was increased by padding with a 10 μm thick foil. The slides were then pressed together and glued with two component epoxy. An opening was left at one side to allow for filling of the cell.

The spacing between glass slides had to be precisely known since it corresponds to the optical path length inside the cell. It can be determined by measuring the transmittance of an empty cell. When the cell is empty, the light is reflected from both glass slides. The two beams can then interfere constructively or destructively depending on the wavelength and the spacing inside the cell. The condition for a maximum can be written as:

$$2d = N\lambda \tag{3.1}$$

The spacing is denoted by d, the wavelength is λ and N is an integer. By measuring two adjacent maxima (N and $N+1$) the spacing can be determined. The results of such measurement are shown in Fig. 3.3. The cell was moved along the wedge direction (x) and at each point the spacing (z) was determined by recording the transmittance spectrum. After this calibration, the cell was filled with liquid crystal. Finally, the opening used for filling was sealed with epoxy.

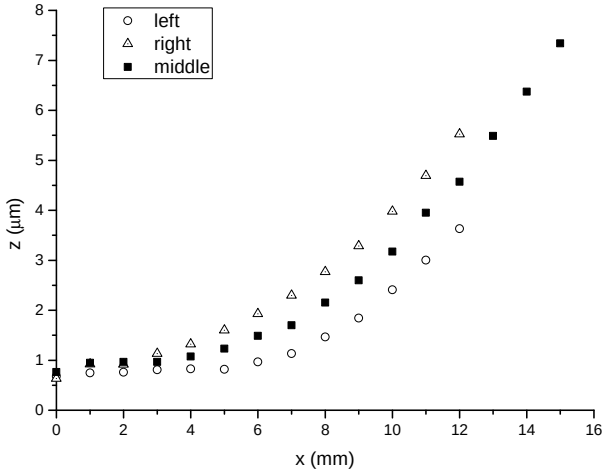

Figure 3.3 *The measurements of wedge cell spacing z. The spacing is different depending on the side of the cell where it was measured because the wedge is not perfectly aligned with the x direction.*

3.4 Illumination setup

To allow for illumination of the 7AB mesogen with different wavelengths, Oriel short-arc lamp housing was used. Mercury or xenon short-arc lamps of 100 W and 150 W, respectively, were

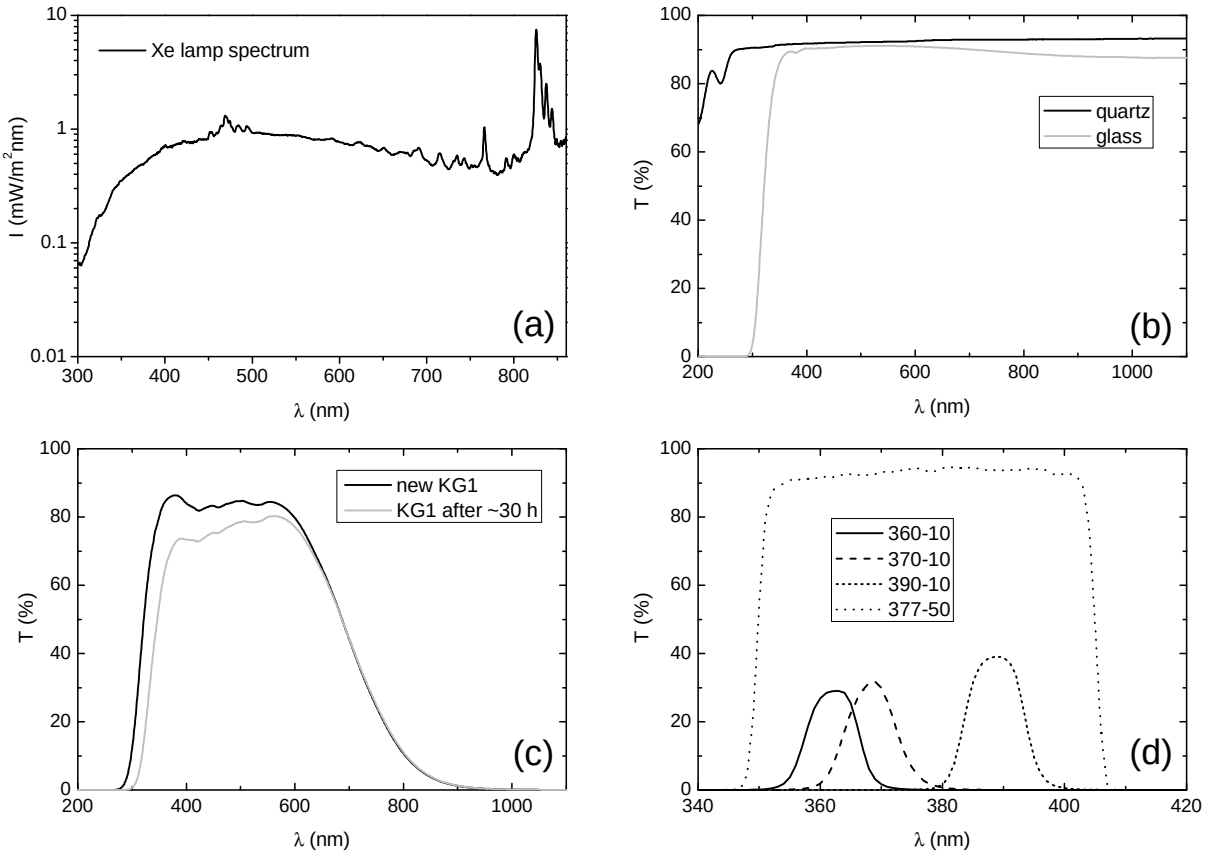

Figure 3.4 *The spectral irradiance of xenon short-arc lamp (a). To ensure maximum transmission in UV, quartz has to be used instead of glass components (b). Deterioration of heat absorbing glass (c). Bandpass filters used to select appropriate wavelength interval (d).*

used as a light source. To allow for long running experiments the light source power supply was remotely controlled via computer.

For some experimental setups, it was more convenient to have a fiber illuminator instead of an ordinary lamp. For this reason, a Newport fiber focusing assembly was added to the system. This allowed for an easy switching between the light focused to a 1 mm diameter optical fiber and the direct collimated light beam.

The output of the lamp was examined using a calibrated Ocean Optics USB2000 spectrophotometer. Results for xenon lamp are shown in Fig. 3.4a. We observe that there is still high enough UV output down to 300 nm. To maintain this output, all the optical components have to be made from quartz because normal glass has poor transmittance for UV below 350 nm (see Fig. 3.4b). However, this was not a big problem since we mostly worked in the $350-400$ nm range.

One of the main difficulties in sample illumination is the heating of the sample due to incident light. Unfortunately, short-arc lamps have high infrared (IR) output which has to be filtered out, not only because of sample heating, but also because other optical components could be damaged. The IR filtering was achieved by using KG1 heat absorbing glass. Since this filter is absorbing, forced-air cooling was employed to maintain the filter temperature at a reasonable level. Since transmittance of KG1 filters in the UV range decreases during long time use as is shown in Fig. 3.4c, they need to be regularly replaced with new ones.

The photoisomerization experiments are not influenced only by heating due to IR light. Visible light also heats the samples. Furthermore, there are unwanted backisomerization effects when

long wavelength light is present. This is why we used bandpass filters to allow only narrow wavelength ranges to pass. The measured transmittance of the applied filters is plotted in Fig. 3.4d. Three filters with 10 nm FWHM and center wavelengths of 360, 370 and 390 nm were used. These filters have about 30 % peak transmittance. When higher light intensity was needed, a high performance filter with central frequency of 377 nm and 50 nm bandwidth was used. This filter has 85 % maximum transmission and broader wavelength band, which is useful when the maximum absorption wavelength of the sample is not precisely known.

In certain situations, lower light intensities were required, e.g. to establish photostationary states with low concentration of cis isomers. Since the photoisomerization rate is much higher than the backisomerization rate, weak light must be used to keep the cis concentration low. This can be achieved by filtering with neutral density filters. The transmittance of filters with absorbances 0.3, 1 and 2 is shown in Fig. 3.5. These absorbances correspond to 50%, 10% and 1% of transmitted light. If even lower intensities were required, different combinations of filters could be used.

When light output from an optical fiber is used, the irradiance can be precisely controlled by using an iris diaphragm mounted in front of the fiber focusing lens. The dependence of light intensity on the nominal diameter of the iris opening is shown in Fig. 3.5.

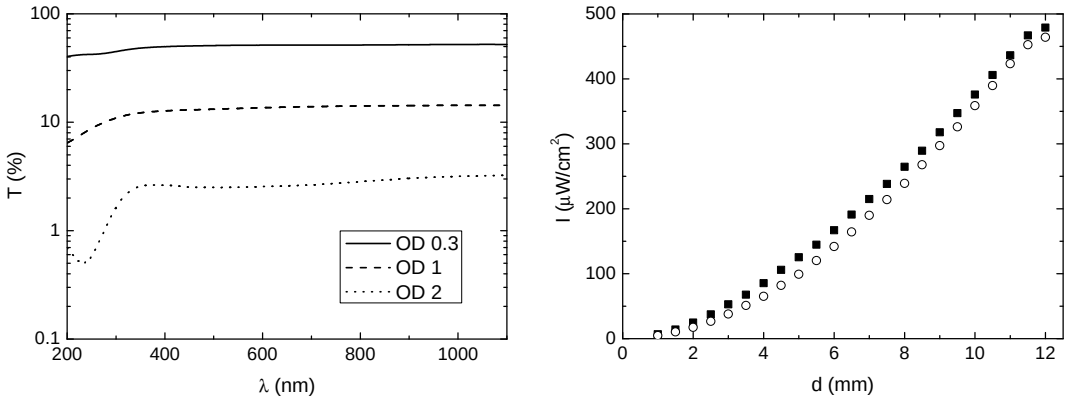

Figure 3.5 *The measured transmittance of neutral density filters with different optical densities (left). The intensity of light was controlled by using iris diaphragm with a variable diameter d (right). A small hysteresis of the iris is present.*

3.5 Digital imaging setup

The photoisomerization and phase separation processes can easily be observed by naked eye during the illumination, because the isotropic phase is transparent whereas the nematic phase is opaque. To obtain a more quantitative data, a digital camera was used to take images at regular intervals. The camera used was Canon D30, connected to a computer and remotely controlled. Extension tubes were used to allow for macro imaging of the sample. A schematics of experimental setup is shown in Fig. 3.6.

In order to resolve the photoisomerization-induced effects from the temperature-induced effects, a good control of the sample temperature is mandatory. Thermal stabilization was ensured by using a home-built temperature-controlled bath which used water as a cooling fluid. To control the temperature, we used a heating element and a PT100 sensor that were connected to an Oxford ITC 503 temperature controller. Temperature gradients were significantly reduced

by mixing the water with a magnetic stirrer. In this way, temperature stability of about 0.1 K was achieved.

The sample was illuminated with a setup described before. The lamp output was collimated to produce a parallel beam. A special quartz window built into the temperature-controlled bath was used to allow for short wavelengths of UV to pass through. The transmittance of water in UV range was checked on a UV-VIS spectrophotometer. Irradiance of UV light incident on the sample was estimated to be 4 mW/cm^2.

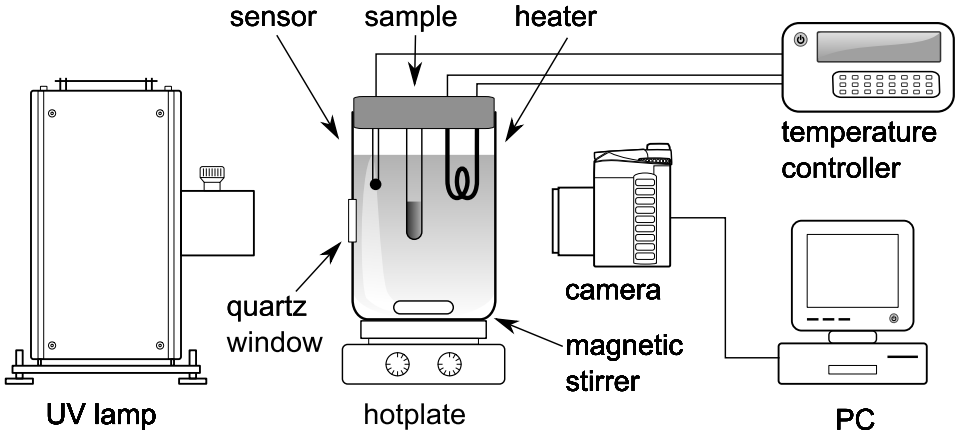

Figure 3.6 *Digital imaging setup.*

3.6 UV-VIS spectroscopy setup

The transmittance of all optical components and absorbance of the sample in a solution was measured by a standard spectrophotometer. The device used was Shimadzu UV-1650 which has a range from 200 to 1100 nm and allows for the measurements at room temperature. There are two issues with standard spectrophotometric equipment: (i) light sources are usually built in, (ii) there is no option to control or stabilize the temperature of the sample. The first problem was solved by using an Ocean Optics USB 2000 spectrophotometer utilizing an optical fiber as a probe for incoming light, providing for direct measurements of the output of the illumination setup. To obtain absolute irradiance measurements, the spectrophotometer was calibrated with a tungsten halogen radiometric standard source.

The problem of non-availability of temperature stabilization was solved using a home-built temperature-controlled chamber. The setup for temperature stabilized absorption measurements is schematically shown in Fig. 3.7. A continuous gas flow of nitrogen was used to regulate the temperature of the sample. An Oxford ITC 503 temperature controller was utilized in a feedback loop to measure the temperature inside the chamber with a PT100 sensor and to heat the gas to obtain the set temperature. A thick layer of polystyrene surrounded the cylindrical cavity for additional thermal insulation. This helped in reducing the temperature gradients which were measured to be about 0.3 K/cm in the vertical and less than 0.1 K/cm in the horizontal direction at 360 K.

The sample was mounted on a translation stage with a range of 20 mm in the horizontal direction, matching the size of the wedge cell. The light from the lamp was guided through an optical fiber and was collimated with Ocean Optics 74-UV lens. The irradiance of light incident on the sample was estimated to be about 0.5 mW/cm^2. Finally, the light transmitted from the sample was collected by another optical fiber and analyzed by USB 2000 spectrophotometer.

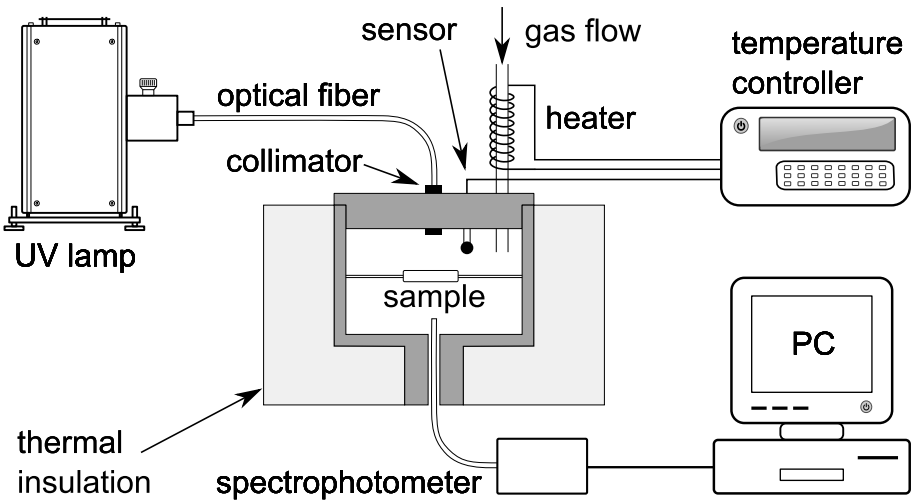

Figure 3.7 *UV-VIS spectroscopy setup.*

3.7 In-situ illumination setup

One of the biggest challenges with NMR of photoisomerizable materials is the illumination of samples directly inside the bore of a superconducting magnet. The main advantage of in-situ illumination is the possibility to observe the photoisomerization and not only the thermal backisomerization process. The temperature stabilization of the sample is better as well since the sample does not have to be moved from the external temperature-controlled chamber into the temperature-stabilized NMR probe.

The light was guided into the magnet with a 5 m long optical fiber. Availability of a fiber of sufficient length is important because illumination equipment is made from magnetic materials and should therefore be as far away from high magnetic fields as possible. O-rings were used to seal the space between the fiber and the entrance of the NMR probe to allow for the temperature of the sample to be regulated using a gas flow cryostat.

One of the main requirements in the measurements of photoisomerization is uniform illumination. When the light beam is non-uniform, different parts of the sample exhibit different photoisomerization rates which leads to inhomogeneity. This is to be avoided in NMR experiment where the whole sample is probed. Unfortunately, the output of the fiber is not flat but rather bell-shaped in the radial direction from the center of the beam (see Fig. 3.8a). The uniformity can be improved by applying a UV-transparent diffuser as can be seen in Fig. 3.8b. To further improve the beam uniformity, we designed a collimator with built-in diffuser and a UV lens. The collimator was manufactured using Vespel plastic because it is durable, temperature stable and non-magnetic. The output from the collimator is shown in Fig. 3.8c. On the edges of 4×5 mm area, which is a typical size of samples under investigation, the light intensity drops only for about 10%.

There is another issue regarding beam uniformity. The usual way of preparing samples is to seal them into a cylindrical cuvette. However, when a uniform beam passes through a glass tube it gets distorted, as is shown in Fig. 3.8d. To overcome this problem, the sample was enclosed between two parallel microscope slides that were sealed at the edges.

When the sample is put inside the NMR coil, the wires block the incident light. This can be avoided by using a sparse coil where there is enough space between the wires to let the light pass through. Residual shadows are however still present (see Fig. 3.9). Another approach is to use a double coil. In this case, the light is not blocked at all. However, the excitation magnetic field

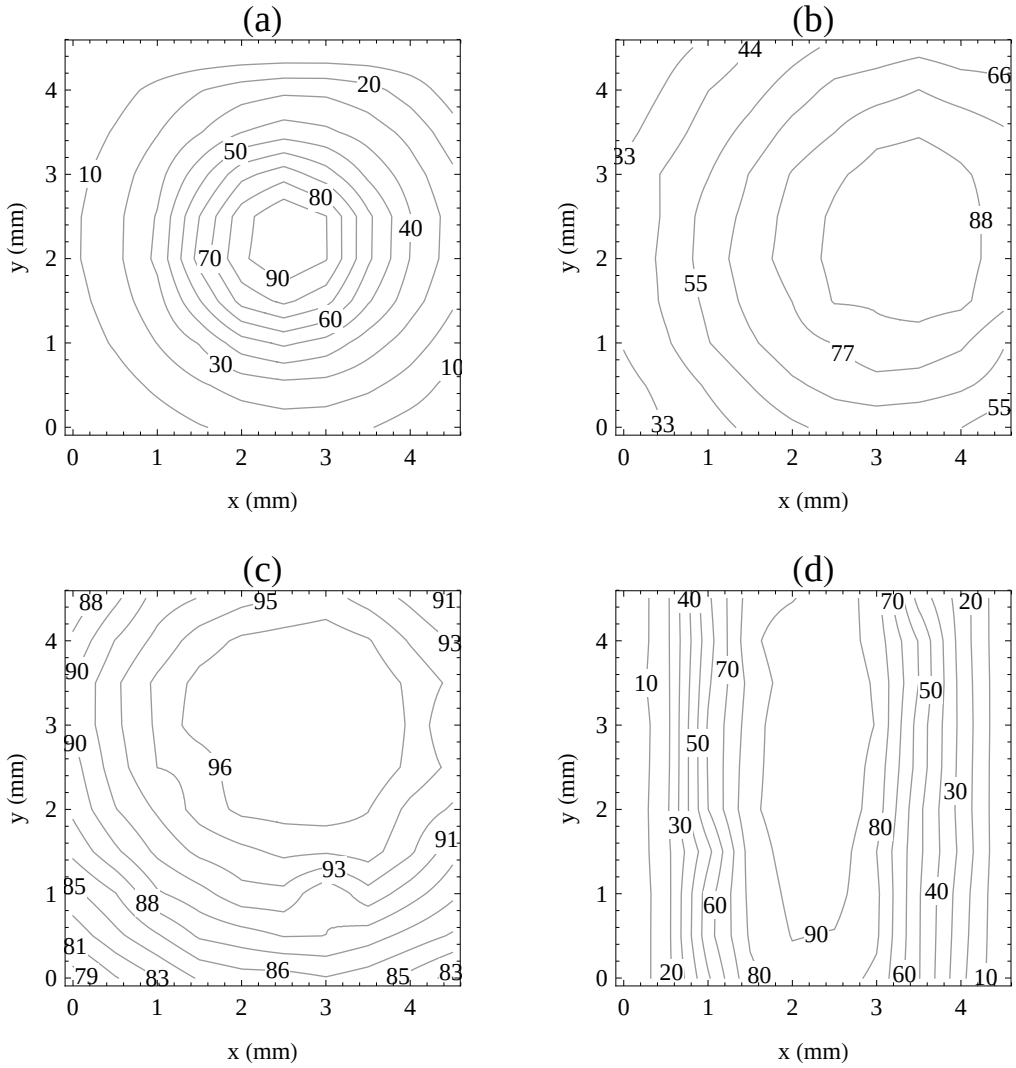

Figure 3.8 *Relative irradiance profiles of light from a fiber (a), fiber and diffuser (b) and home-built collimator (c). The light intensity inside a cylindrical cuvette is shown in (d).*

is significantly reduced at the center of the coil. Nevertheless, such a coil was used for most measurements to achieve the flattest intensity profile of incident light.

3.8 NMR measurements

Deuteron NMR measurements were performed on a 380 MHz Oxford Instruments superconducting magnet equipped with a home-built spectrometer. The measurements were taken at Larmor frequency 58.336 Mhz. Solid echo sequence was used with two $\pi/2$ pulses ranging from 4 to 7 μs, depending on the coil used. In experiments where the double coil was used, the $\pi/2$ pulses were about 9 μs. A typical delay between pulses was 40 μs and the repetition rate of the pulse sequence was 100 ms.

"Exorcycle" phase cycling scheme was used whenever possible [105]. This kind of phase cycling is designed to compensate for imperfect pulses in spin-echo sequences but reduces the signal to one half. It was therefore not appropriate for experiments where very little signal was present. The quality of the signal was additionally improved by reducing the noise with an analog 100 kHz low-pass filter.

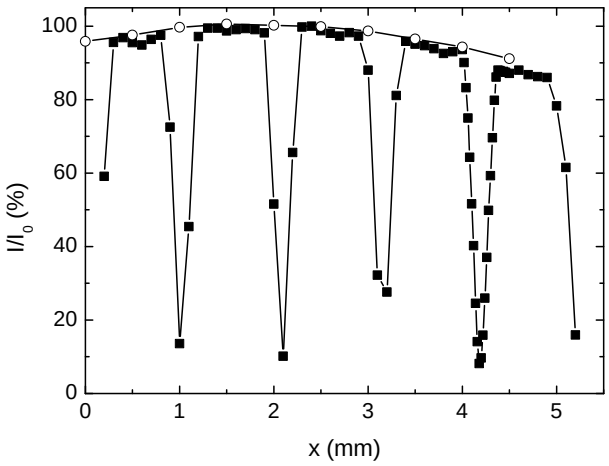

Figure 3.9 *The relative intensity profile of light incident on a sample (white circles). When the sample is inside a coil, the shadows from the wires can clearly be seen (black squares). The lines are drawn only as a guide to the eye.*

The temperature of the sample was regulated in a Oxford Instruments cryostat connected to a Pfeiffer turbo-molecular vacuum pump. Constant nitrogen gas flow of about 1.5 L/min was used to heat or cool the sample. The temperature was controlled by Oxford Instruments ITC.

In a typical photoisomerization experiment, the sample was first illuminated for few hours after which the lamp was switched off and the spectra were taken at regular intervals. Since the acquisition time for one spectrum had to be much shorter than the cis-to-trans relaxation time, the spectra were averaged 8500 times (15 min) at higher and 17000 times (30 min) at lower temperatures.

4 Results and discussion

In this chapter, the measurements of phase separation in diheptylazobenzene are presented. Although NMR was the preferred method since it provides for precise measurements of phase ratios and order parameters, important information was obtained by digital imaging and UV-VIS spectroscopy as well. Hence, the results of these measurements are presented first, followed by the analysis of NMR measurements in bulk and confined 7AB.

4.1 Phase separation in UV-controlled binary LC mixture

When researching new materials, it is important to first acquire the basic physical and chemical characteristics of the substance at hand. For photoisomerizable materials, these are certainly the wavelengths of the absorption peaks. The molar absorption coefficients are also important since they determine the penetration depth of incident light into the sample. However, the starting information about the phase separation behavior in UV-illuminated 7AB was the ratio between nematic and isotropic phases which was obtained by digitally imaging the photoisomerization process.

4.1.1 Digital imaging of biphasic states

The phase separation of UV-illuminated diheptylazobenzene can be observed in a transparent cuvette since the material is liquid crystalline. The nematic and isotropic phases can easily be resolved, because the isotropic phase is transparent whereas the nematic is opaque.

A sequence of images taken during the illumination and the back-relaxation is shown in Fig. 4.1. Before the measurement the sample was kept in the dark at a constant temperature well below the nematic-to-isotropic transition. At this temperature, the cis concentration is negligible as can be calculated from the ratio $N_c/N_t = \exp(-\Delta E/kT)$, where $\Delta E \sim 0.5$ eV is the energy difference between cis and trans isomers [72]. At the start of the measurement, the material is therefore completely nematic. During the illumination, cis isomers are formed, which at high enough concentrations result in a creation of the isotropic phase. This phase is separated from the nematic phase due to a difference in density and can be seen as the dark colored region filling the top part of the cuvette.

It should be noted that even in nematic part there is a thin layer of isotropic phase near the side of cuvette which is illuminated. This shows that the cis isomers are generated along the entire length of the sample, yet only at the illuminated surface. The cis-rich isotropic phase then migrates towards the top part of the cuvette.

The behavior is even more complex when the lamp is switched off after 1 h. The amount of the isotropic phase is not reduced instantaneously. On the contrary, the phase separation process continues for some time before the backisomerization effects are visible. This indicates that phase separation is slow. There is an excess amount of cis isomers in the nematic phase which

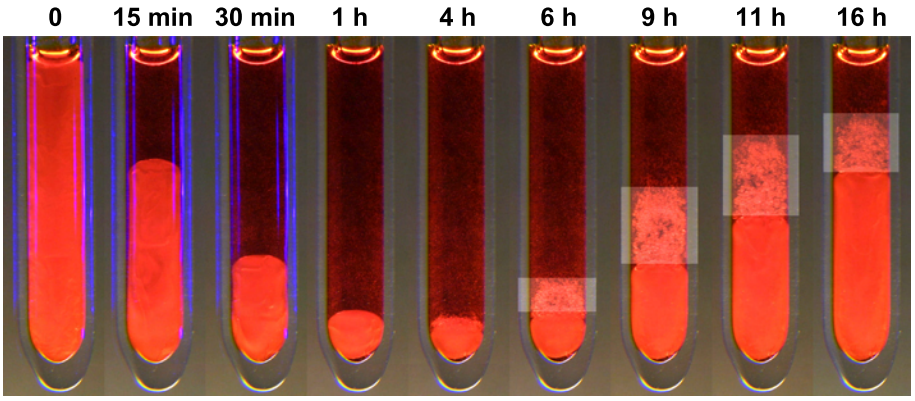

Figure 4.1 *A sequence of digital images of the photoisomerization process at* 315 *K. The image at* 1 *h shows the sample immediately after the lamp was switched off. The biphasic regions are highlighted in the last four images.*

tend to phase separate into the isotropic phase. During this time, the amount of isotropic phase is still increasing.

Due to thermal backisomerization, the cis concentration reduces and droplets of nematic material start forming in the isotropic phase. This is clearly seen in the last four images in Fig. 4.1. The formation of nematic droplets confirms that we deal with the nucleation and growth mechanism of the phase separation process [37]. In contrast to the alternative scenario, spinodal decomposition, the system is not unstable, therefore the nematic phase starts forming only when a nucleus is present with low enough cis concentration. The appearance of droplets only at the lower end of isotropic phase suggests that small concentration gradient may be present. Moreover, very small nematic domains do not scatter light and are invisible, although they may be present at the top of the sample. The backisomerization process is much slower than photoisomerization and can last for several hours.

To obtain a more quantitative picture of the experiment we plotted the volume fraction of the isotropic component versus time. The volume fraction was estimated from the images simply by dividing the area of isotropic phase with the area of the whole sample. Fig. 4.2 shows a

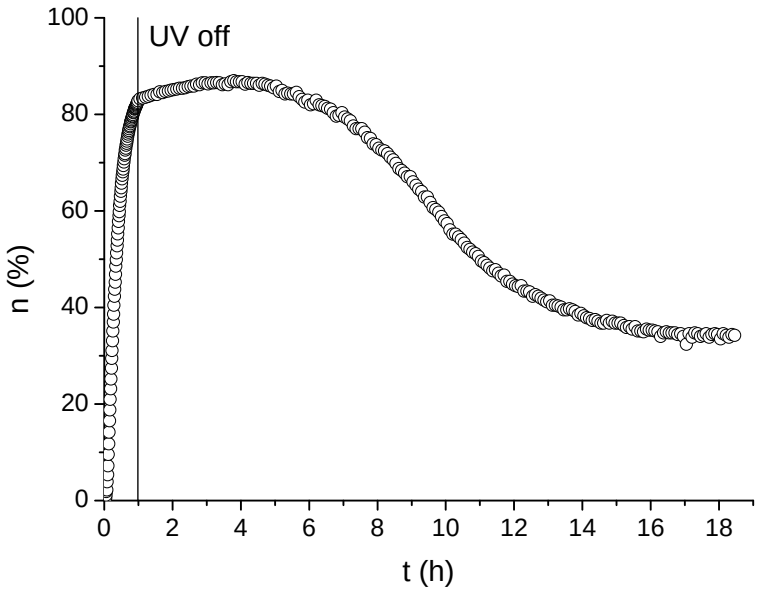

Figure 4.2 *The volume fraction of the isotropic phase vs. time at* 315 *K. Illumination started at* $t = 0$.

rapid growth of isotropic phase during the illumination. After the lamp is switched off, the phase separation rate is much slower and in approximately 3 h the isotropic phase reaches its maximum volume. This is due to a finite phase separation rate of the isotropic phase as explained previously.

In the backisomerization stage of the above experiment, the isotropic phase does not vanish completely, but rather saturates at about 35% volume fraction. This is because a separate lamp was used to illuminate the sample for taking the images. The irradiance of this lamp in the UV region was about 20 μW/cm^2 which is negligible compared to 4 mW/cm^2 of the main light source. An important conclusion can be drawn from this experiment. At constant irradiance and temperature the system reaches a stationary state where the number of newly created cis molecules equals the number of backisomerized trans molecules. When the light intensity is very low, this occurs in a phase coexistence region and the ratio between phase volumes remains constant. Therefore, it should be possible to dynamically adjust the ratio between phases by changing the light intensity. We shall exploit this fact for a detailed investigation of the temperature-concentration (T- ϕ) phase diagram of trans-cis 7AB binary mixture.

Due to extra light source, the backisomerization process is slower than it would be in the dark. The cis-to-trans conversion rate, however, can not be determined by looking at the disappearance of the isotropic phase. Cis molecules are present not only in the isotropic phase but also in the nematic phase. The decay in Fig. 4.2 does therefore not directly correspond to the decay of cis concentration.

4.1.2 Absorbance measurements

Performing UV-VIS spectroscopy of a photoisomerizable dye in a solution is the easiest way of measuring dye's absorption peaks. However, since the behavior of material in a solution is different from bulk material, the measured absorption peaks do not necessarily correspond to those of bulk dye. An example where the surrounding matrix shifts the absorption peaks are dyes incorporated into elastomers where peak shifts of about 25 nm were detected [106]. Nevertheless, we measured the absorbance spectrum of 7AB in cyclohexane to obtain at least approximate positions of absorption peaks.

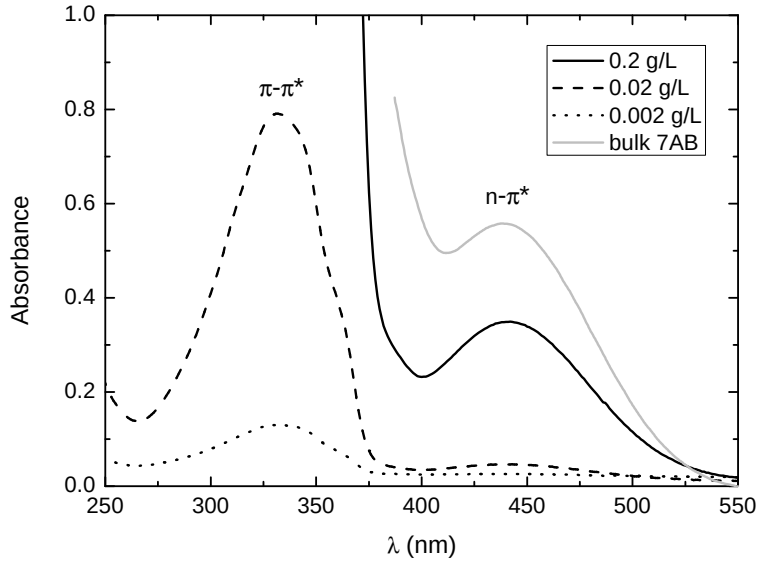

Figure 4.3 *Absorbance spectra of bulk 7AB and 7AB in a solution.*

Results of measurements at three different concentrations are presented in Fig. 4.3. The measurements were taken with a standard spectrophotometer at room temperature. The absorption peak around 440 nm that corresponds to $n-\pi^*$ transition is visible at all three concentrations. On the contrary, the 330 nm absorption peak can not be detected at the highest concentration because of high absorbance of the $\pi-\pi^*$ transition. This peak has a maximum absorbance above 4 which is the limit of the detector sensitivity.

The fourth measurement in Fig. 4.3 is the absorbance of non-diluted 7AB. This spectrum was recorded using UV-VIS spectroscopy setup described in section 3.6. The temperature was stabilized at 330 K so that the material was in the isotropic phase. For the same reasons as in highly concentrated 7AB solution, the $\pi-\pi^*$ absorption peak could not be observed.

Exact positions of the observed peaks are presented in table 4.1. The position of $n-\pi^*$ absorption peak in diluted 7AB does not change considerably. Furthermore, the values obtained for solutions are similar to the value for bulk 7AB which means that there is no significant peak shift. We can assume that the same is true for $\pi-\pi^*$ absorption peak which is located at 332 nm. We therefore estimate this value to be the optimal wavelength for the stimulation of trans-to-cis photoisomerization.

Table 4.1 *Positions of the absorption peaks.*

	0.2 g/L	0.02 g/L	0.002 g/L	bulk 7AB
$\lambda_{\pi-\pi^*}$ (nm)	—	332	332	—
$\lambda_{n-\pi^*}$ (nm)	442	440	434	439

4.1.3 Determination of the penetration depth

Penetration depth is an important parameter of a photoisomerizable material since it determines the amount of sample actually exposed to illumination. Data from the absorption measurements show that there is very strong absorption at optimal photoisomerization wavelength, suggesting that only the surface layers of the sample are affected by light.

In the simplest model, the intensity profile of light inside the sample is exponential as described by Eq. (1.27):

$$I(z) = I_0 e^{-z/\zeta} \tag{4.1}$$

The penetration depth is $\zeta = 1/(\kappa n)$ where z denotes the distance from the surface. By plotting the logarithm of transmittance versus the distance z, a straight line crossing the origin should be obtained.

We determined the penetration depth by measuring the transmittance of a wedge cell described in section 3.3. The cell was moved on a translation stage in the horizontal direction. Since the cells were calibrated, the optical path length of a vertical beam passing through the cell was known at each point. One of the main problems of such a measurement is the determination of incident light I_0. Besides attenuation by the sample, the irradiance is decreased by the two quartz slides the wedge cell is built of. To measure the transmittance of the quartz slides, the cell must be empty. In this case, however, the light is reflected from the surfaces which gives inaccurate I_0. In practice only the attenuation of one quartz slide was taken into account. This leads to an error in I_0 which can be written as $I_0 = xI_0'$. The light incident on the cell which can be measured is I_0'

and x a proportionality constant. The resulting equation for determining the penetration depth is:

$$-\ln\frac{I}{I_0'} = \frac{1}{\zeta}z - \ln x \tag{4.2}$$

Another problem when measuring the penetration depth was the phase separation behavior of photoisomerizable material. During the measurement, some of the material is converted to the cis form which is absorptive as well but has different absorptivity than the starting trans isomer. The penetration depth is therefore changing with illumination. To avoid this problem, the sample was first held in the dark to start with a completely trans state. When measuring, the wedge cell was quickly moved from one end to the other so that the measurement time was short as compared to the phase separation rate. The following results therefore determine the penetration depth of the trans-isomer 7AB.

The absorbances at different positions of the wedge cell are shown in Fig. 4.4. Two sets of data were taken: one at wavelengths around the $n-\pi^*$ absorption peak and the other one in the $\pi-\pi^*$ absorption peak region. Fitting with a straight line showed that the last term in Eq. (4.2) is negligible. The measured value I_0' was therefore close to the real I_0. Larger errors are found only at wavelengths below 380 nm. This is due to the low intensity of transmitted light which can not be accurately measured.

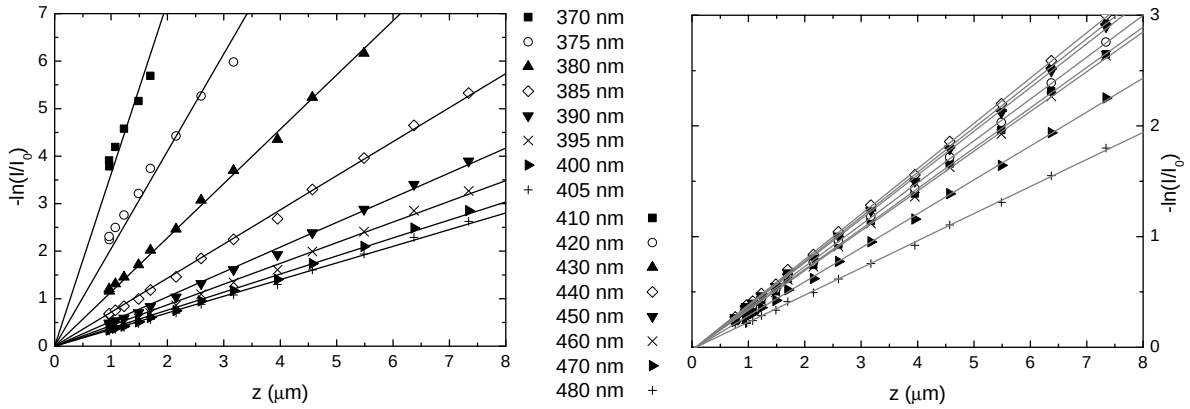

Figure 4.4 *Absorption measurements at different wavelengths and different positions of the wedge cell. The lines are linear fits through the origin.*

Penetration depths determined from the fits are shown in Fig. 4.5. The penetration depth strongly depends on the wavelength. It is shortest at the position of absorption peaks as can be seen from the local minimum near 440 nm. The penetration depth at $\pi-\pi^*$ absorption wavelength could not be measured because of strong absorbance exceeding the range of our experimental setup. A solution to this problem would be to build a wedge cell with a shorter optical path. However, it is difficult to build wedge cells with spacings below 1 μm. Nevertheless, we can estimate the penetration depth at $\pi-\pi^*$ absorption wavelength to be only a few 100 nm.

Obviously, a rather large volume of the sample can be photoisomerized in spite of a very short penetration depth. This is so since when the cis isomers are formed, the penetration depth is increased due to lower cis absorption in this wavelength range. Moreover, due to diffusion of trans and cis molecules, there are always some trans molecules available at the surface where trans-to-cis photoisomerization can take place.

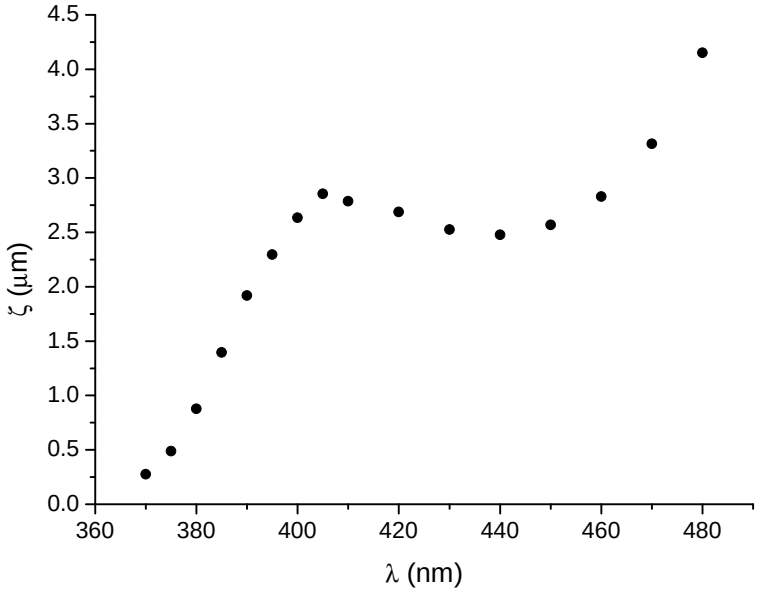

Figure 4.5 *Penetration depth strongly depends on the wavelength.*

4.2 ^{2}H NMR of bulk diheptylazobenzene

Deuteron NMR measurements presented in this section supplement the digital imaging measurements of bulk 7AB. The main advantage of NMR is the possibility to determine nematic order parameter as demonstrated in previous experiments with diheptylazobenzene [34]. However, an important improvement over the previous measurements was the use of in-situ illumination. This allowed for the observation of the sample during the photoisomerization stage and not only during the backisomerization stage.

4.2.1 Basic NMR parameters

Initially, some parameters that are important in NMR measurements were determined. The spin-lattice relaxation time T_1 measures the rate at which the magnetization relaxes back to initial state after being excited by radiofrequency pulses. The usual estimate is that 3-5 times T_1 is needed for the system to completely relax which determines the repetition rate in time-averaged NMR measurements. Optimization of the repetition rate is especially important in experiments where signal-to-noise ratio is low.

The measurement of longitudinal relaxation time T_1 is presented in Fig. 4.6. Inversion recovery sequence was used where the magnetization is first inverted by applying a π pulse. Next, there is a variable delay t after which the usual spin-echo sequence is used to acquire the signal. The strength of the signal versus the delay t was then fitted with a mono-exponential curve to obtain the T_1 values. The spin-lattice relaxation is slower in nematic and faster in isotropic phase. This is in agreement with previous measurements of relaxation in liquid crystals [107].

The order parameter S in the nematic phase can be determined by measuring the frequency splitting $\Delta\nu$ of deuteron NMR doublet. The two quantities are connected by Eq. (1.55). In bulk samples, the static magnetic field reorients the molecules so that nematic director is parallel to the field and angle ϑ is zero. Therefore, only one unknown variable has to be determined: the average quadrupolar frequency $\overline{\nu}_Q$. This parameter can be determined from the powder spectrum. The maximum spectral splittings in a powder spectrum correspond to deuterons with the largest

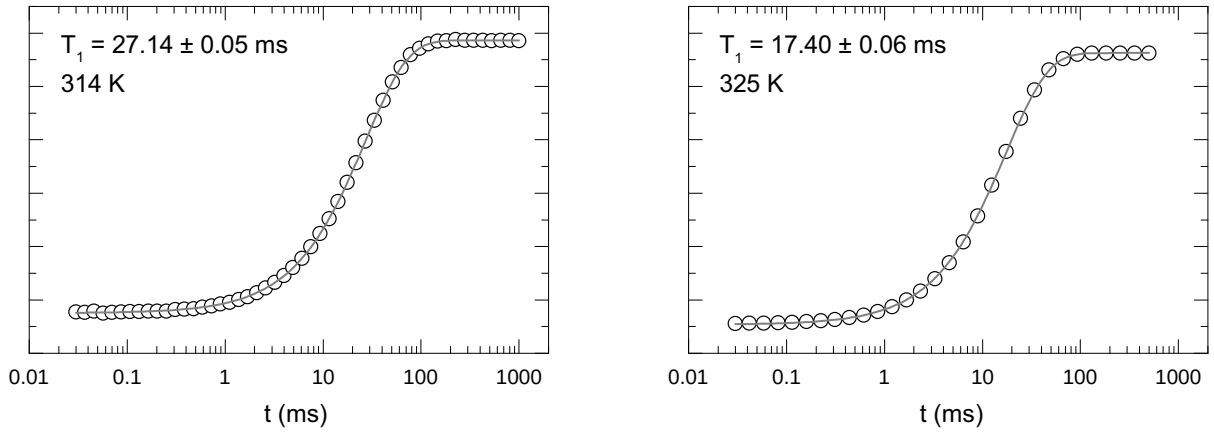

Figure 4.6 *The determination of spin-lattice relaxation time in nematic (left) and isotropic phase of trans-7AB (right).*

EFG eigenaxis oriented along the external magnetic field direction **b**, i.e. $\vartheta' = 0$.

The experimentally detected powder spectrum of 7AB is shown in Fig. 4.7. To obtain a powder pattern, molecular motion had to be frozen which was achieved by crystallization of the sample at 295 K. Due to a very broad spectrum, the signal intensity was low. The number of repetitions was about 10^5. We determined the maximum splitting to be 240 kHz. According to Eq. (1.50), the quadrupolar frequency ν_Q is $2/3$ of maximum splitting. The average quadrupolar frequency is then calculated as $\overline{\nu}_Q \approx \nu_Q/3$, yielding $\overline{\nu}_Q = 53$ kHz.

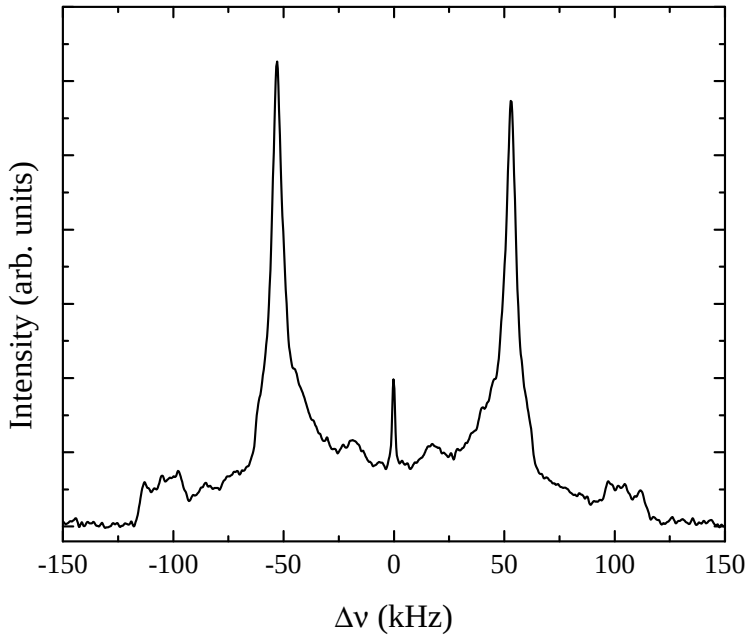

Figure 4.7 *7AB powder spectrum recorded at* 295 *K.*

4.2.2 Thermotropic behavior

A standard approach to characterize the thermotropic behavior (changes induced by temperature) of a liquid crystal is by measuring deuteron NMR spectrum (see section 1.3.1). Detailed measurements of the temperature dependence of the deuteron spectra can also help in differentiating thermal effects from the photoisomerization effects.

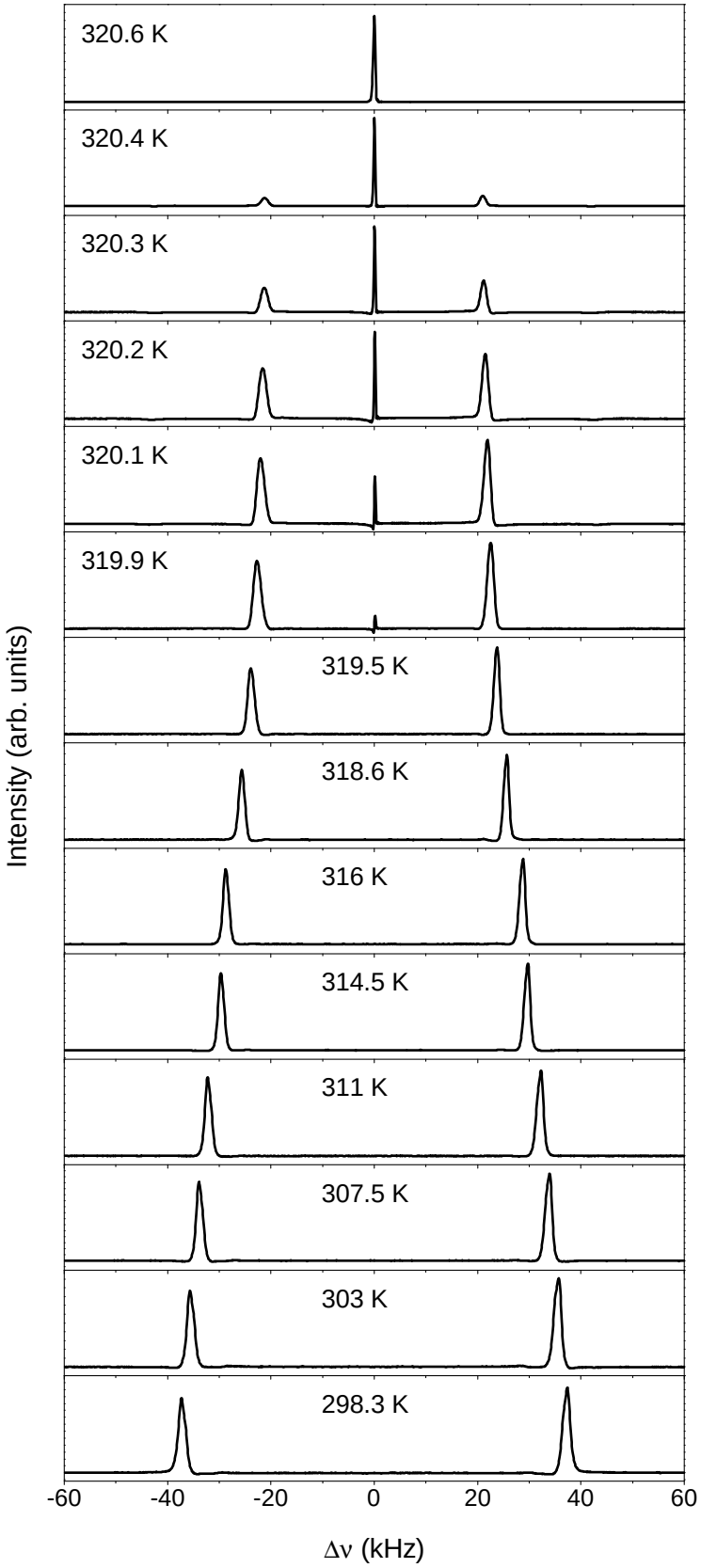

Figure 4.8 *Temperature dependence of 7AB spectra. The N-I phase transition takes place at* $T_{NI} \approx$ 320.2 *K.*

To record the temperature dependence, the sample was first held in the isotropic phase in the dark to obtain a well-defined zero-cis initial state. The temperature was then lowered in 0.5 K steps and stabilized for 15 min after each step. In the vicinity of the N-I phase transition, the temperature step was reduced to 0.1 K and the wait time to 5 min. At each temperature, NMR spectrum was recorded by averaging 1000 times.

A series of bulk 7AB spectra is shown in Fig. 4.8. At high temperatures, the phase is isotropic as is evident from a narrow central line. As the temperature is lowered, nematic doublet is formed. The splitting of the two nematic lines determines the order parameter as discussed in the previous section. It should be noted that there is a coexistence region where both phases are present. However, this region is very narrow and is estimated to be only about 0.3 K.

In order to determine the temperature dependence of the nematic order parameter, the spectra were fitted with a double Lorentzian curve. The line splitting calculated this way is presented in Fig. 4.9. The order parameter was then calculated using expression:

$$S = \frac{2}{3}\frac{\Delta\nu}{\overline{\nu}_Q} \tag{4.3}$$

The order parameter decreases on approaching the nematic-to-isotropic transition from below. At the T_{NI}, it reaches a minimum value of $S = 0.53$ which is slightly higher than the universal value of 0.43 predicted by Maier-Saupe theory. Nematic phase exists down to 298 K, far below the melting temperature, due to supercooling of the material.

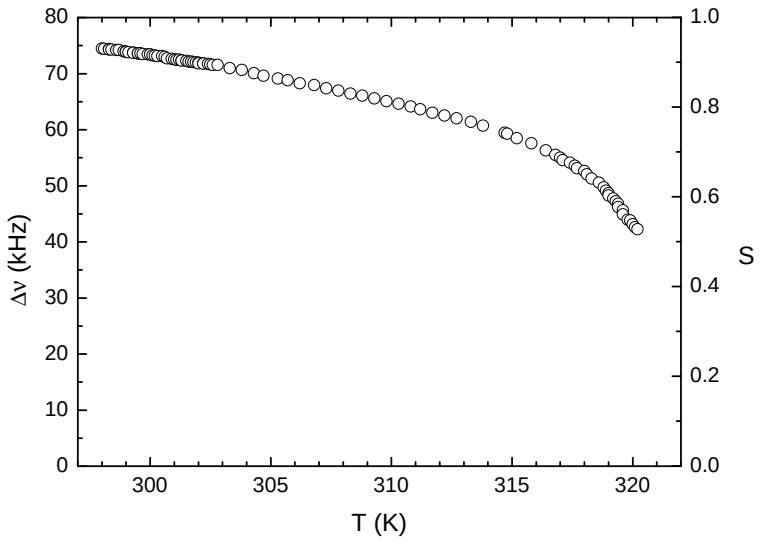

Figure 4.9 *The correlation between line splitting and nematic order parameter in bulk 7AB.*

4.2.3 Light induced N-I phase transition

The major part of bulk 7AB measurements were UV-illumination experiments. These measurements were performed using in-situ illumination. However, a collimating lens was not used because the cylindrical geometry of the sample did not allow for uniform illumination (see Fig. 3.8d). Furthermore, it has been shown previously that only a thin layer at the surface is directly affected by UV light. For these reasons only, the non-uniform UV output of a bare fiber was used to illuminate the sample inside a sparse coil. The sample was held at 310 K and illuminated for 8 h.

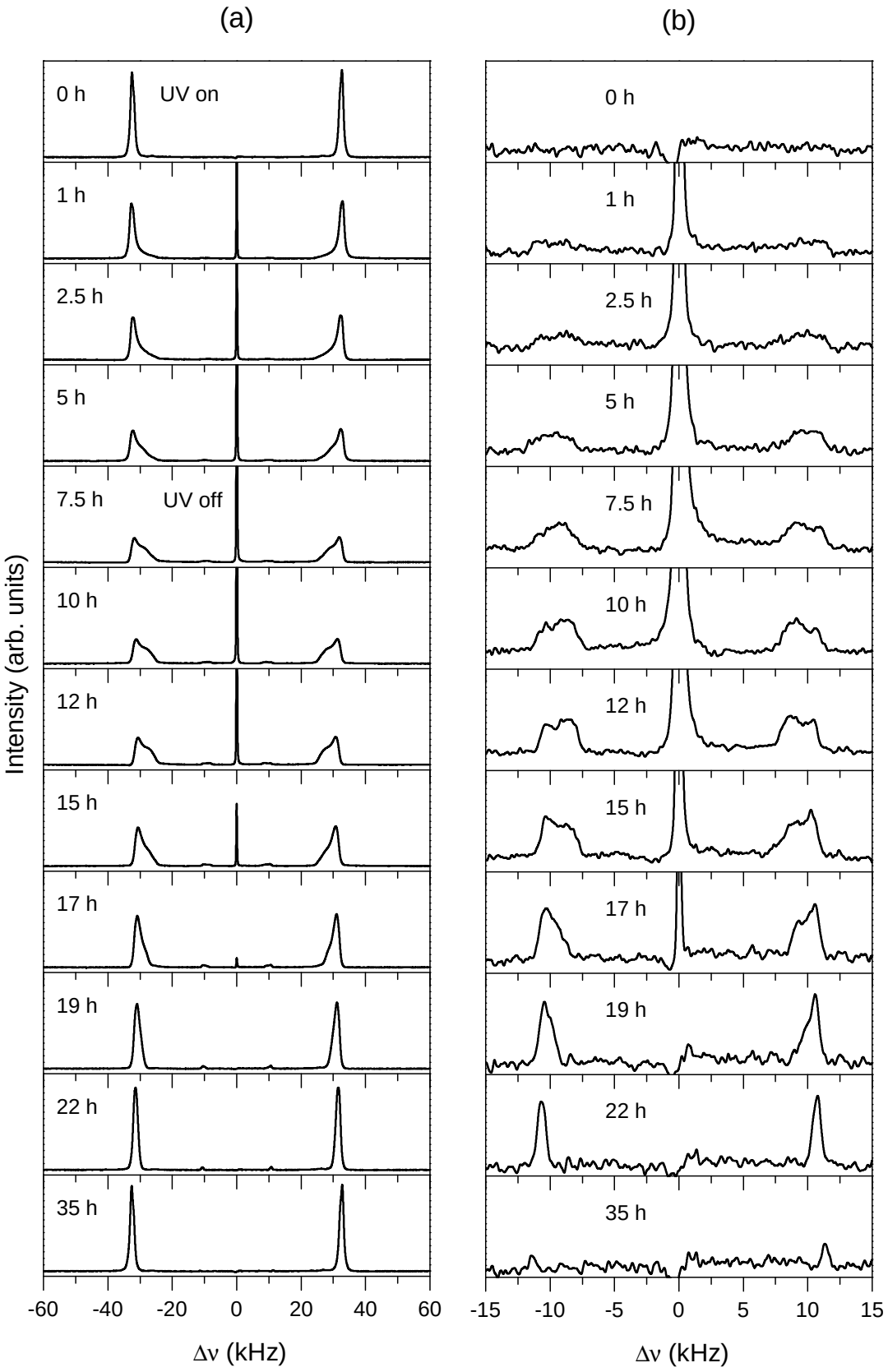

Figure 4.10 *Bulk 7AB spectra during and after illumination (a). Magnification reveals an additional doublet with roughly* $1/3$ *of normal nematic splitting (b). The spectra were recorded at* 310 *K.*

The measured spectra are shown in Fig. 4.10. As expected from digital imaging experiments, the disappearance of nematic doublet is accompanied by appearance of a central isotropic peak. However, the nematic lines are not narrow as in the case of temperature-dependence measurements of non-illuminated samples. This is due to the inhomogeneity caused by non-uniform illumination. The illuminated part of the sample exhibits high concentration of cis molecules. These molecules then migrate to other parts of the sample. Since migration is slow, the effect of concentration gradients is substantial. Consequently, the spatial distribution of order parameter values results in an inhomogeneously broadened spectrum.

In contrast to the case of thermotropic phase transition, the nematic-isotropic coexistence region is wide and easily observed. By our experimental setup, the increase of cis concentration to the level where only the isotropic phase would be present was unfeasible. However, it was also impossible to have only nematic phase since the isotropic phase was immediately produced at the illuminated surfaces. We note that the relatively low reachable cis concentration as well as the sample inhomogeneity are two main problems and a severe limiting factor, which prevented a more detailed quantitative analysis of the observed phase separation behavior in bulk samples.

By carefully inspecting the spectra, one can observe an additional doublet which is shown magnified in Fig. 4.10b. It has been demonstrated in previous studies that non-mesomorphic solutes or mesogens with low T_{NI} can be ordered by liquid crystalline solvent [108]. We therefore conclude that the non-mesomorphic cis isomer can be aligned by the mesomorphic trans molecule. This means that in the nematic phase there are two contributions to the NMR spectrum: the usual nematic trans doublet and the nematic cis doublet. The intensity of the latter is however much smaller than the intensity of the former.

Cis doublet starts to form during the illumination stage as a pair of very broad lines, a fact attributed to the inhomogeneous cis concentration in the sample. When the light is switched off and the isotropic phase disappears, the only mechanism left that drives the cis-to-trans conversion is the thermal backisomerization. The backisomerization rate is the same in all parts of the sample, therefore, concentration gradients vanish. The nematic cis spectral lines become narrower, reflecting the fact that orientational ordering is homogeneous throughout the sample. The cis doublet persists for a long time after the isotropic phase has vanished completely. This

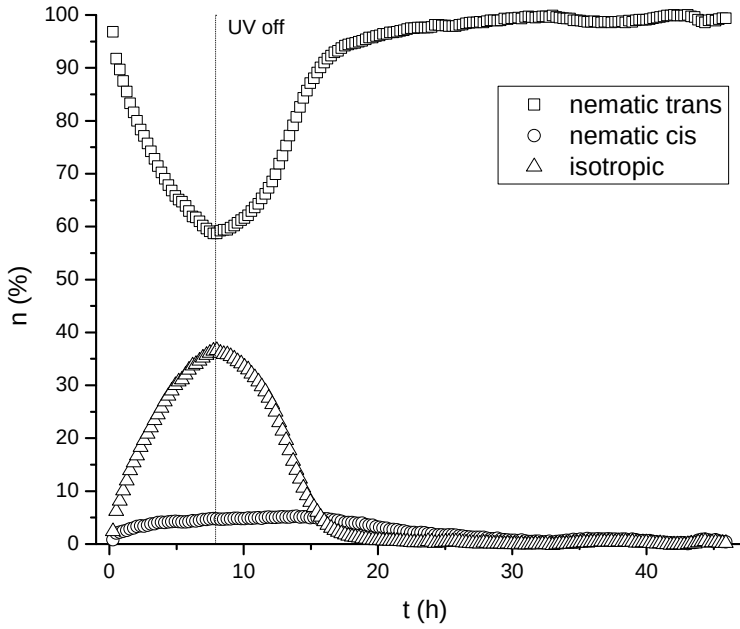

Figure 4.11 *The fraction of the isotropic phase and nematic trans and cis components at* 310 *K.*

confirms that the inner doublet is associated solely with the nematic phase and not with the presence of isotropic phase. Finally, all cis molecules are converted to trans form resulting in a disappearance of the cis doublet.

The time evolution of the isotropic and both nematic components is displayed in Fig. 4.11. The data was obtained by calculating the areas below the corresponding lines. Since the area under a certain NMR line is proportional to the number of respective molecules giving rise to this line, the volume fractions of different phases can be calculated.

The results obtained for the isotropic phase can be directly compared with data from digital imaging measurements (Fig. 4.2). The growth of the isotropic phase is much slower in NMR measurements due to about 10 times lower light intensity. For the same reason, the growth of the isotropic phase is not observed after the lamp is switched off, in contrast to what has been observed in digital imaging experiments. Since the number of cis molecules increases in the UV-illumination stage at a slow rate, any change in the cis concentration is immediately reflected in the ratio between the two phases. Therefore, after the illumination is switched off, the volume of the isotropic phase starts to decrease immediately.

It is interesting to observe the behavior of cis molecules. Their concentration in the nematic phase starts to decrease only after the isotropic phase vanishes. This is understandable, since in the coexistence region, the cis concentration in nematic and isotropic phases, respectively, should be constant. The observed behavior is in agreement with the theory of N-I phase coexistence of binary systems, discussed in section 2.2.4. The point at which the isotropic phase disappears is very important. Since the only phase left is nematic, the fraction of nematic cis component equals the concentration of cis molecules in the sample. From Fig. 4.11 we can determine that the concentration of cis isomers approximately 11 h after the illumination was switched off is about 2.4 %. This is a very important estimate because it determines the maximum cis concentration at which diheptylazobenzene still forms only nematic phase (at 310 K). We shall exploit this fact for direct determination of cis concentrations in the phase diagram.

In Fig. 4.12, the nematic splitting of trans and cis molecules is plotted versus time. During the illumination part of the measurement, the splitting of both components decreases. After the illumination is switched off, the splitting slowly relaxes back to the initial all-trans state. The results in Fig. 4.12 were obtained by fitting with a double Lorentzian line. This kind

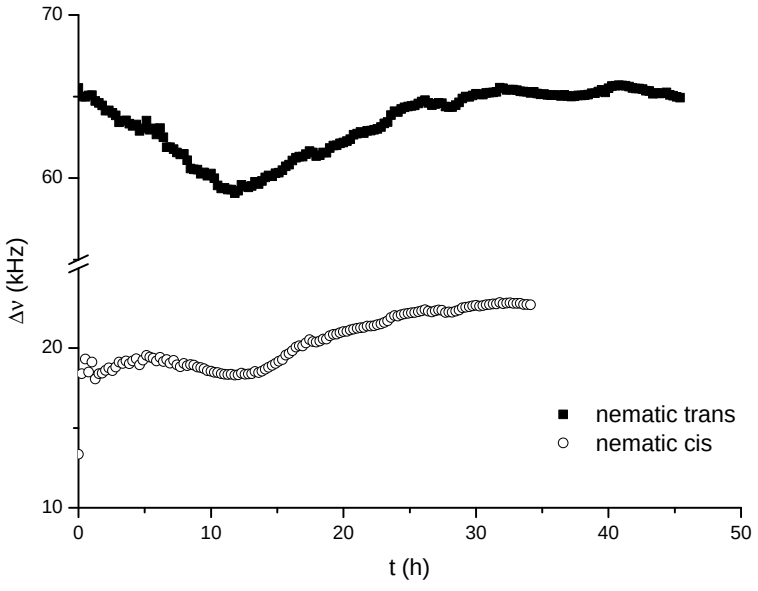

Figure 4.12 *Doublet splitting of nematic trans and nematic cis components in the NMR spectrum.*

of fit is however inaccurate since the lines are broadened due to sample inhomogeneities. Moreover, phase separation as predicted by Eq. (2.39) is not complete because cis concentration is dynamically changing and migration of molecules is slow. This is why a coexistence region with constant order parameters is not detected, i.e. the splitting is continuously changing. The presented result is therefore more accurate at longer times, whereas the first part during the illumination stage is useless for quantitative analysis.

By looking at the cis splitting in Fig. 4.12, a question arises about the connection between the splitting and the order parameter of cis molecules. Normally, the nematic order parameter was determined for elongated molecules with a well defined long axis. The definition of cis ordering is more subtle. The cis isomer is a boomerang shaped molecule which makes defining any preferential direction very difficult. On the other hand, we can treat the cis form as composed of two equivalent parts since the isomer is symmetric. Each part alone then has elongated shape and the preferred direction corresponds to the average direction of the rotating C-D bond. If the order parameter is defined for the two respective molecular segments, the usual Eq. (1.55) still applies and the calculation of the cis and trans order parameters is the same.

4.3 ^{2}H NMR of confined diheptylazobenzene

We shall show that by confining 7AB to cylindrical cavities of Anopore membranes, most problems encountered in the measurements of bulk 7AB can be overcome. This is why the experimental part of this thesis primarily deals with the analysis of behavior of 7AB in confined geometry. The temperature-dependence measurements were performed first, in order to compare the bulk behavior with the behavior of the confined system. Next, the photo-induced behavior of the material was examined by varying different experimental parameters. Finally, the phase diagram and the order parameters were determined.

4.3.1 Thermotropic phase transition

The temperature-dependence measurements of confined 7AB were recorded using the same procedure as for bulk 7AB. The results presented in Fig. 4.13 reveal a behavior similar to bulk, with coexisting nematic doublet and isotropic central line. However, there exists a major difference. When the central line is magnified a small but well-resolved splitting is revealed (see Fig. 4.13b). This is in agreement with previous measurements of liquid crystals confined to Anopore membranes [46]. The splitting arises from the surface-induced order and is visible due to a large surface-to-volume ratio of the confining material. The surface-induced order is not easily destroyed and persists deep into the isotropic phase.

Temperature dependence of the line splitting was obtained by fitting the spectra with a double Lorentzian curve. The results are shown in Fig. 4.14. Around the phase transition temperature, the surface-induced order is maximal with a value $S = 0.014$. When the temperature rises, the surface-induced order decreases. Such behavior is characteristic for the nematic-to-isotropic transition in the presence of external aligning fields [101].

In Fig. 4.14b, a comparison between nematic order in confined and bulk material is shown. Temperature profiles of the doublet splitting, equivalently of the nematic order parameter are almost identical. No shift of T_{NI} is observed within the experimental accuracy. A slightly lower frequency splitting of the confined material could be due to the misalignment of the sample which was difficult to orient perfectly in the magnetic field. Another difference is the supercooling limit which was determined to be higher in confined material.

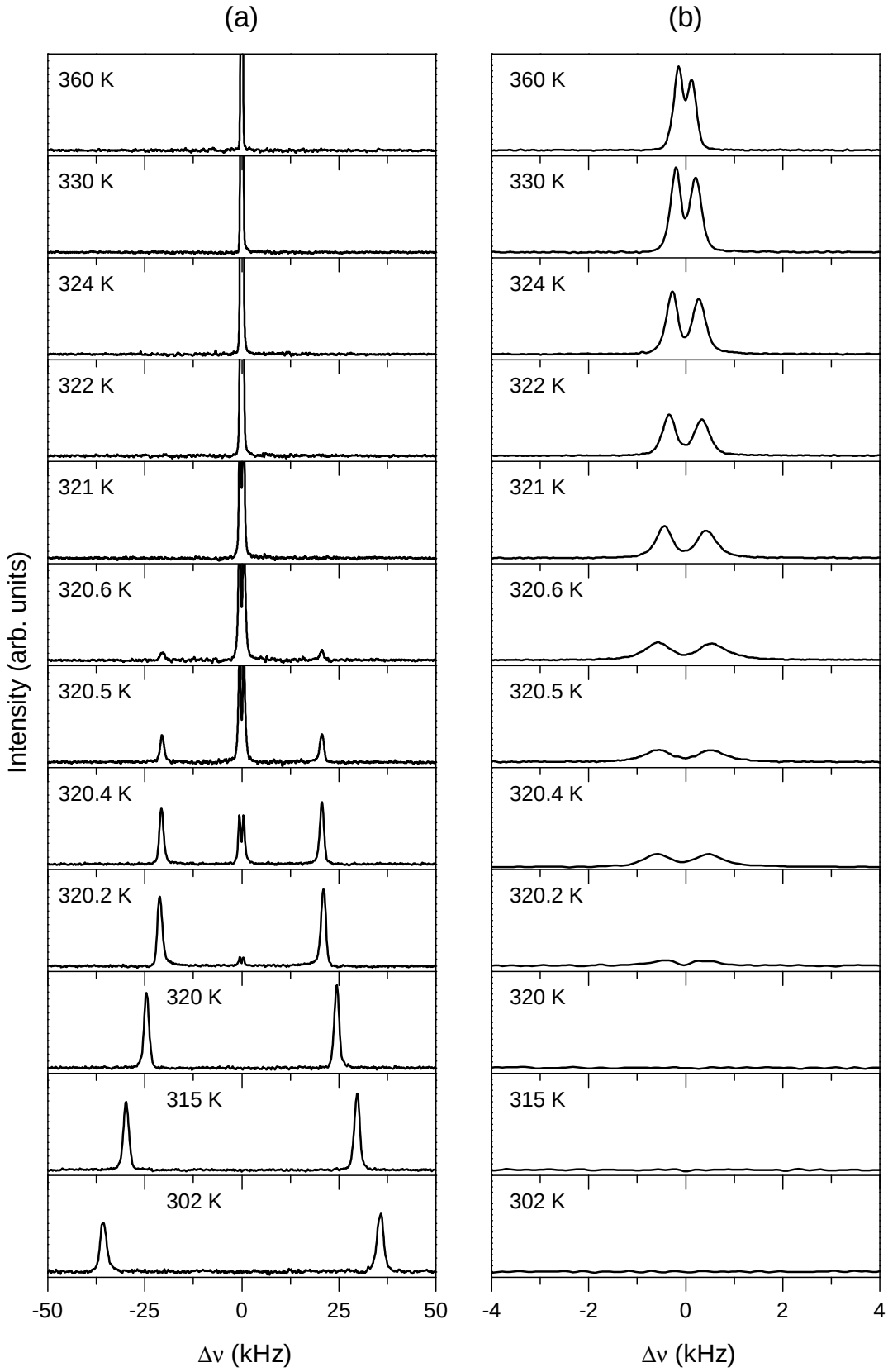

Figure 4.13 *Temperature-dependence of deuteron NMR spectra of confined 7AB (a). The magnified isotropic central line reveals a small splitting (b).*

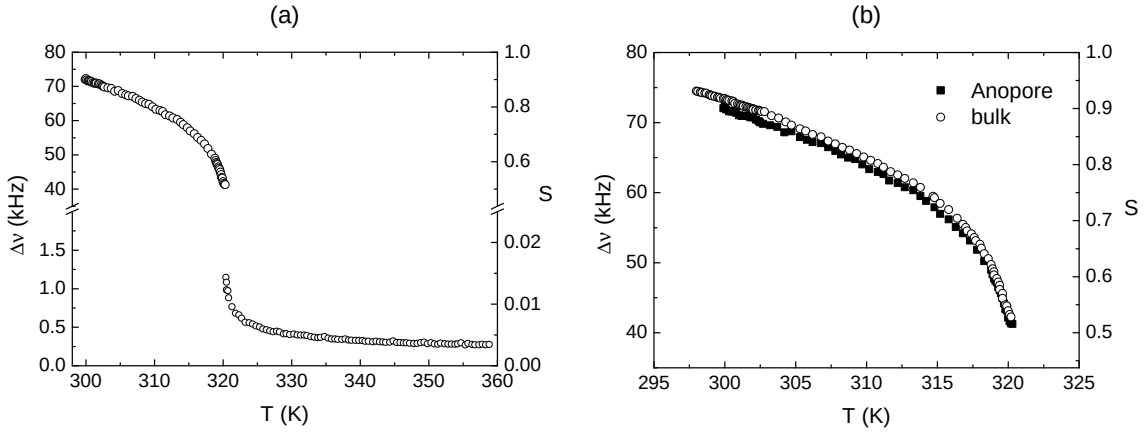

Figure 4.14 *Confined 7AB exhibits surface-induced order even high above the nematic-isotropic phase transition (a). The comparison of order parameters of bulk and confined 7AB in nematic phase (b).*

One of the basic questions when dealing with liquid crystals inside cylindrical cavities is the structure of the director field. As opposed to bulk measurement where the molecules are always aligned by the external magnetic field, the director field in confined samples can be reoriented with respect to external magnetic field by rotating the sample. This rotation results in the angular dependency of the NMR spectrum, providing information on the structure of the director field. Fig. 4.15 shows the spectra at various orientations of the Anopore membranes with respect to the external magnetic field, recorded in the nematic and in the isotropic phases. In both phases, a doublet can be seen. Its splitting strongly changes with orientation. This can be attributed to the presence of the $P_2(\cos\vartheta)$ term in Eq. (1.55). In the isotropic phase a single line is visible around the magic angle because of low resolution of the spectrometer. By comparing this result with the predicted angular patterns (see Fig. 1.12) we conclude that the structure inside the cavities is axial [4]. When the pores are reoriented to be perpendicular to the external magnetic field, the splitting is reduced by half, as expected for axial alignment.

4.3.2 Behavior of UV-illuminated confined diheptylazobenzene

Before the attempt to determine the temperature-concentration phase diagram, the behavior of UV-illuminated samples had to be examined in terms of impact of numerous experimental parameters. An experiment with confined photoisomerizable liquid crystal has a long list of parameters which can substantially alter the behavior:

- number of Anopore membranes
- atmosphere (air or nitrogen)
- wavelength of UV light
- illumination time
- illumination uniformity (improved by collimation)
- irradiance

The experiments which are described in the following were mandatory in order to assure a satisfactory control over the above parameters. All the measurements were performed in the same

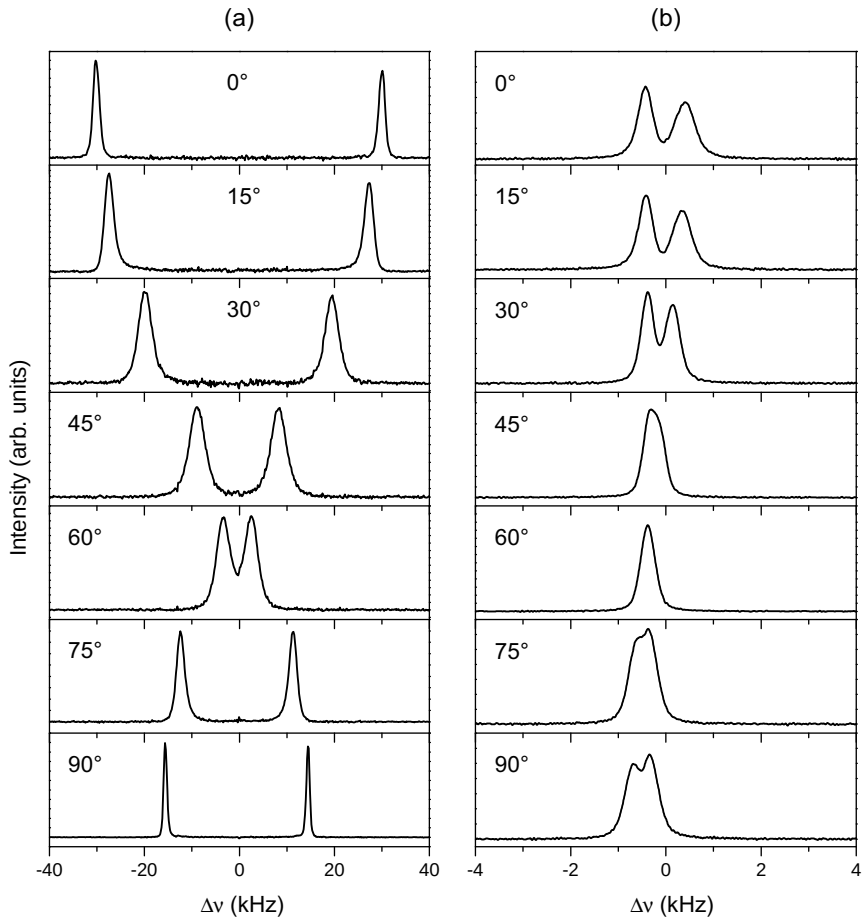

Figure 4.15 *Angular dependence of the deuteron NMR spectra of Anopore confined 7AB in the nematic phase at* 315 *K (a) and in the isotropic phase at* 322 *K (b).*

manner: the sample was initially illuminated for a certain period after which the measurements were continued until the sample relaxed back to initial zero-cis state. From the acquired spectra, the volume fraction n of the isotropic phase was calculated and plotted versus time.

Let us emphasize that the volume fraction $n = 100\%$ corresponds to a complete disappearance of nematic phase, i.e. in the deuteron NMR spectrum only the isotropic phase is visible. However, in general the isotropic phase consists of a mixture of trans and cis molecules. As we shall show in the following, experimental conditions have to be controlled carefully in order to provide for complete cis saturation in the isotropic phase.

First, we determined a suitable number of stacked Anopore membranes. Since the stack is only illuminated from one side, it is anticipated that in a thick stack, photoisomerization would only take place in the upper membranes. On the other hand, it is desirable from the point of view of experimental sensitivity, to have as many membranes as possible.

Two samples with different number of Anopore pieces were compared: the first sample consisted of 8 Anopore membranes (sample #1) whereas the second had only 5 Anopore membranes (sample #2). There are three important things to be noted in Fig. 4.16. First, there is a sudden drop in the volume of the isotropic phase when the light is switched off. This is attributed to the heating of the sample due to UV light. When the light is switched off, the sample quickly cools down which reduces the amount of the isotropic phase. The temperature effect can clearly be distinguished from the backisomerization since the latter has much longer timescale. Next thing to be noted is the different volume fraction of the isotropic phase in the two samples.

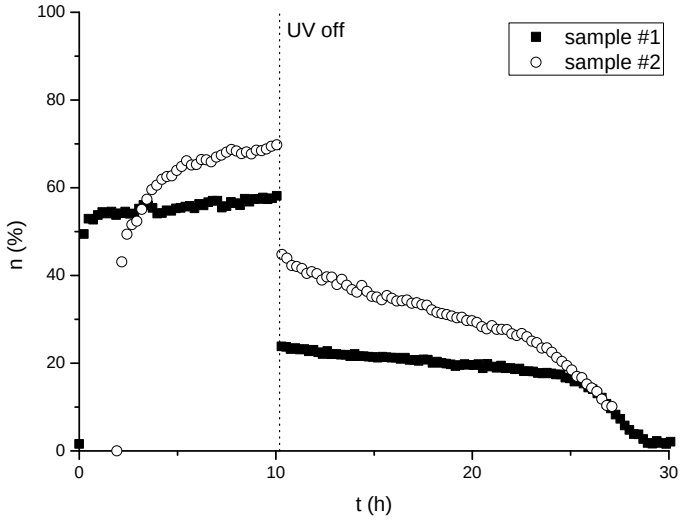

Figure 4.16 *Comparison of two samples with a different number of Anopore membranes. The temperature was held constant at* 318 *K and the UV filter used was 377-50. The time axis of sample #2 is shifted so that the start of relaxation of both samples is shown at the same time.*

Since we know that the penetration depth of UV light is only a few 100 nm, we conclude that most of the Anopore membranes do not get illuminated. The membranes at the non-illuminated side thus stay in the nematic phase which is why the total volume of the isotropic phase never reaches 100%. The last conclusion that can be drawn from Fig. 4.16 is about the relaxation process. Although the samples were different and illuminated for different amount of time (10 h for sample #1 and 8 h for sample #2), they both show similar relaxation times.

Experimental reproducibility was further tested with sample #1. Two consecutive measurements were taken with the same experimental parameters. As shown in Fig. 4.17, the measurement is fully reproducible even though the relaxation process lasts for more than 30 h.

Since it is impossible to homogeneously illuminate multiple Anopore membranes, all further measurements were conducted with a third sample (sample #3) consisting of a single Anopore

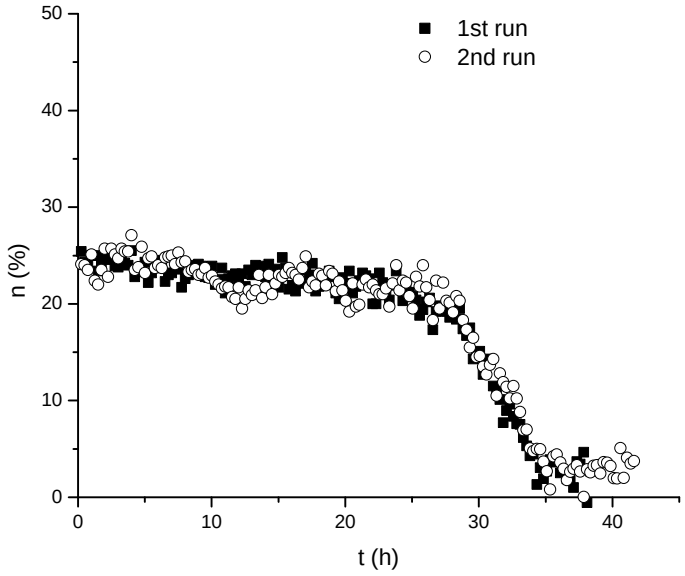

Figure 4.17 *Test of the reproducibility of photoisomerization behavior at* 310 *K. The lamp was switched off at* $t = 0$.

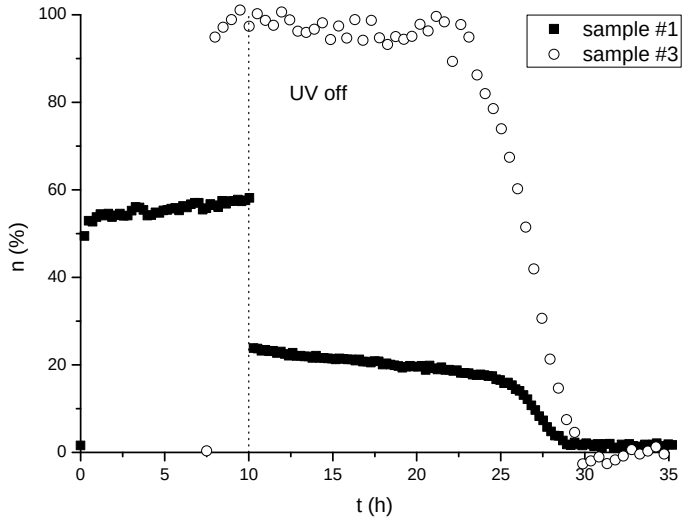

Figure 4.18 *To fully photoisomerize the material a single Anopore piece had to be used. The data was acquired at* 318 *K.*

membrane. The comparison of sample #3 and sample #1 is shown in Fig. 4.18. We can see that with the single-membrane sample, the volume fraction of isotropic phase easily reaches 100%. Furthermore, there is no discontinuous jump. Since the material is fully photoisomerized when UV is switched off, the change in temperature due to UV heating can not be detected, although it is probably still present. The use of a single Anopore membrane has its drawbacks. Because the amount of material is reduced, the signal-to-noise ratio of NMR measurements is significantly lower. Nonetheless, it was still possible to acquire NMR spectra with reasonably good S/N ratio.

Another experimental parameter that changes the behavior of confined samples is the atmosphere around the samples. Since the NMR temperature control uses nitrogen gas flow, one obvious choice is to leave the sample open and in contact with the nitrogen gas during the measurement. On the contrary, when the sample is sealed before the measurement, it remains unaffected by the later change of the environment. As can be seen from Fig. 4.19, the environment strongly affects the relaxation process. Even though the sample exposed to nitrogen atmosphere was illuminated for 6 h compared to only 2.5 h for sealed sample, the isotropic phase started to

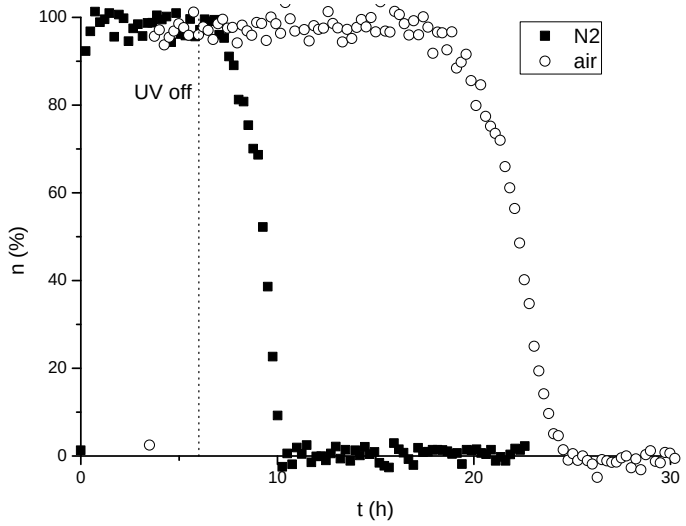

Figure 4.19 *The comparison of open (N_2) and sealed (air) sample at* 318 *K.*

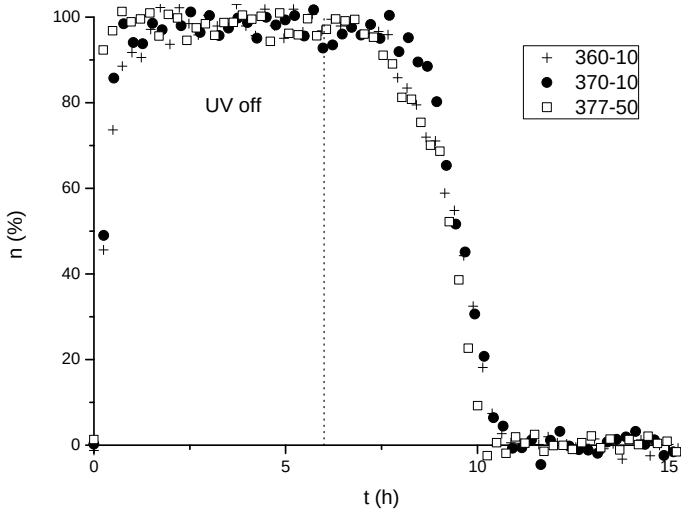

Figure 4.20 *The effect of different UV bandpass filters on the isotropic-nematic conversion behavior of sample #3 in nitrogen atmosphere. The sample was illuminated three times for* 6 *h at* 318 *K.*

vanish almost immediately after the illumination was switched off. On the contrary, the sealed sample stayed in the isotropic phase for about 15 h before the conversion to the nematic phase started.

One possible explanation of such a huge difference in relaxation is the presence of moisture in the air. The water molecules get dissolved in the liquid crystal or adsorbed at the Anopore inner surfaces and can change the interactions between liquid crystalline molecules, resulting in a change of phase diagram. Therefore, to obtain reproducible results, the environment of the sample has to be held constant. To allow for comparison with bulk samples that had to be sealed, confined samples in air environment were used in all subsequent measurements if not stated otherwise. We note that the dependence of the behavior on the atmosphere deserves further examination, but we decided to keep it out of scope of this study.

The effects of different wavelengths of UV light were investigated by changing the bandpass filters. Three filters were used with central wavelengths of 360, 370 and 377 nm, respectively, while all other experimental conditions were kept constant. The bandwidth of 377 nm filter was 50 nm while the bandwidth of the other two filters was 10 nm. The results are shown in Fig. 4.20. By carefully looking at the first hour of the illumination one notices that the nematic phase vanishes much faster when the filter with 50 nm bandwidth is used. This is expected since higher light intensity leads to faster photoisomerization. However, the type of the bandpass filter appears to have no effect on the relaxation process. We can thus assume that the concentration of cis molecules after many hours of illumination if fully saturated at 100%. All three filters therefore produce an initial state where there are mostly cis molecules in the sample. Consequently, the relaxation behavior of the sample is the same for all three types of filters.

Since the cis concentration is affected by the illumination time it was interesting to compare the measurements when this time was varied. The sample in Fig. 4.21 was illuminated at 318 K for different lengths of time. The 377-50 bandpass filter was used in all three cases. It can immediately be seen that the isotropic-to-nematic transition is much slower at short illumination times. The effect is due to non-uniformity of the incident light beam. Since the sample is not uniformly illuminated, different parts of the sample reach different cis concentrations. Each part then relaxes differently which leads to smearing-out of the isotropic-nematic conversion process. When the sample is illuminated for longer times, increasingly larger volume of the sample gets fully saturated with cis molecules as was the case in previous measurements (see Fig. 4.20). In

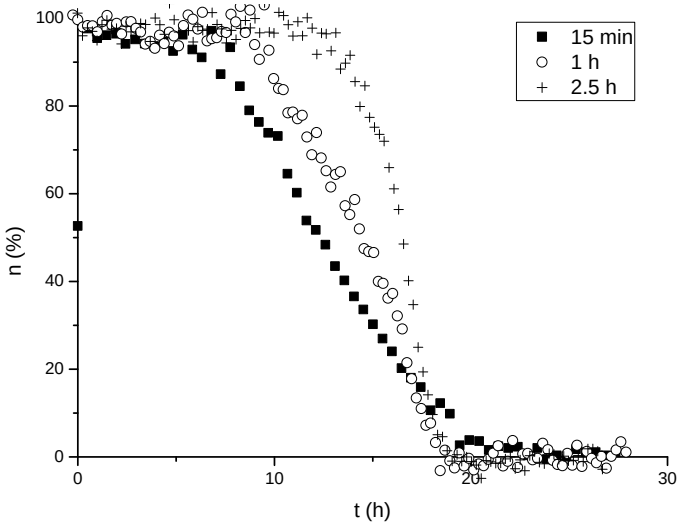

Figure 4.21 *The effect of the illumination time on the isotropic-to-nematic transition. The light was switched off at* $t = 0$.

such homogeneous sample, the transition is apparently faster as seen from Fig. 4.21.

So far, the output of a bare fiber was used for illuminating the sample. The non-uniformity of such output produced an inhomogeneous distribution of cis isomers. In order to assure homogeneous initial state of the system, a collimator was added to the in-situ illumination setup. With the uniform intensity of the light beam, the cis concentration in the sample is always homogeneous, therefore the isotropic-to-nematic transition is fast. This can be seen from the time decay of the isotropic phase shown in Fig. 4.22. The sample was illuminated for 1 h. Measurement was then repeated by illuminating for 10 h. Although the transition looks the same it occurs at different times after the UV light was switched off. We conclude that when the sample was illuminated for only 1 h the cis concentration was not saturated. Consequently, shorter time was needed to reach the cis concentration at which the transition occurs.

By using a uniform light beam it was possible to control the initial cis concentration by changing the intensity of light. This was achieved by varying the diameter of the iris opening.

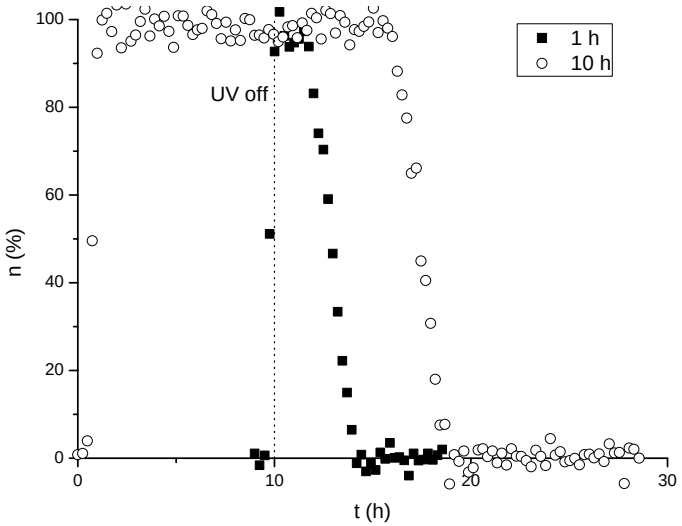

Figure 4.22 *The effect of the illumination time on the isotropic-to-nematic transition when a collimator is used to produce uniform light beam.*

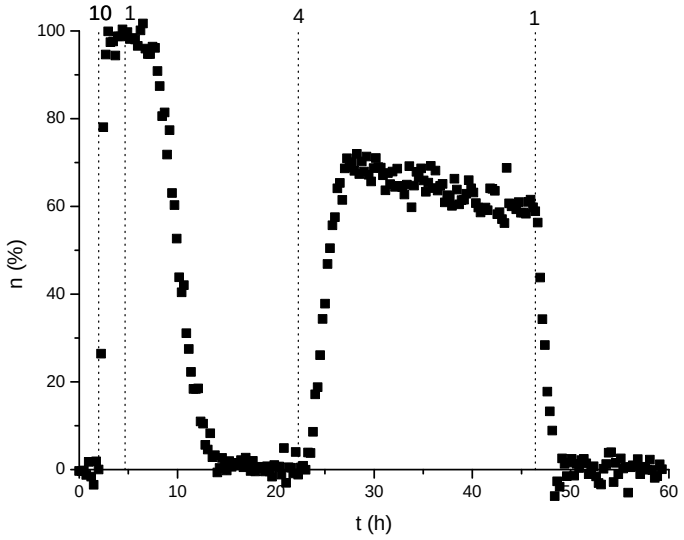

Figure 4.23 *The change in the volume fraction of the isotropic phase due to variation of the intensity of illumination beam. The numbers at the top mark the diameter of the iris opening (in mm).*

The results of such a measurement are presented in Fig. 4.23. With closed iris ($d = 1$ mm), only the nematic phase can be seen, whereas with an open iris ($d = 10$ mm), only the isotropic phase is present. To bring the system into the coexistence region, some fine-tuning was necessary with the appropriate iris diameter determined to be about 4 mm. We noted that the system is extremely sensitive to changes in light intensity. A weak drift of the isotropic volume fraction was observed while the iris opening was kept constant. This is attributed to the variations of irradiance of the lamp beyond our control.

The results of measurements presented above provided for crucial information for defining the optimal measuring conditions. It was determined that heating of the sample due to illumination is present and that the UV light fully penetrates only the first Anopore membrane. In addition, atmosphere effects were confirmed to be present in 7AB. Furthermore, the impact of non-uniform illumination was analyzed and the problems related to variations of irradiance explained. On the basis of these conclusions, we selected the optimal sample to consist of only one Anopore membrane, sealed in a container. The incident light beam had to be as uniform as possible (achieved by using a collimator), and the illumination time long enough to allow for complete saturation of cis molecules. Only the relaxation part of the measurements will be considered in the following, in order to completely exclude the heating effects. Using this approach, the sample has a well defined initial state, i.e. it is fully in the isotropic phase with homogeneous, saturated cis concentration. Let us emphasize that it was impossible to achieve such an initial state with a bulk system.

4.3.3 Light induced phase transition

The goal of illumination-induced phase transition measurements was to determine the temperature-concentration phase diagram of photoisomerized 7AB. More specifically, we wanted to obtain the width of the N+I coexistence interval, the orientational order parameters of cis and trans component in the N and I phases, as well as the concentration of cis-isomer in the two coexistent phases.

The experimental setup for the main set of measurements was prepared according to the discussion in the previous section. A single Anopore piece was used and the light was well

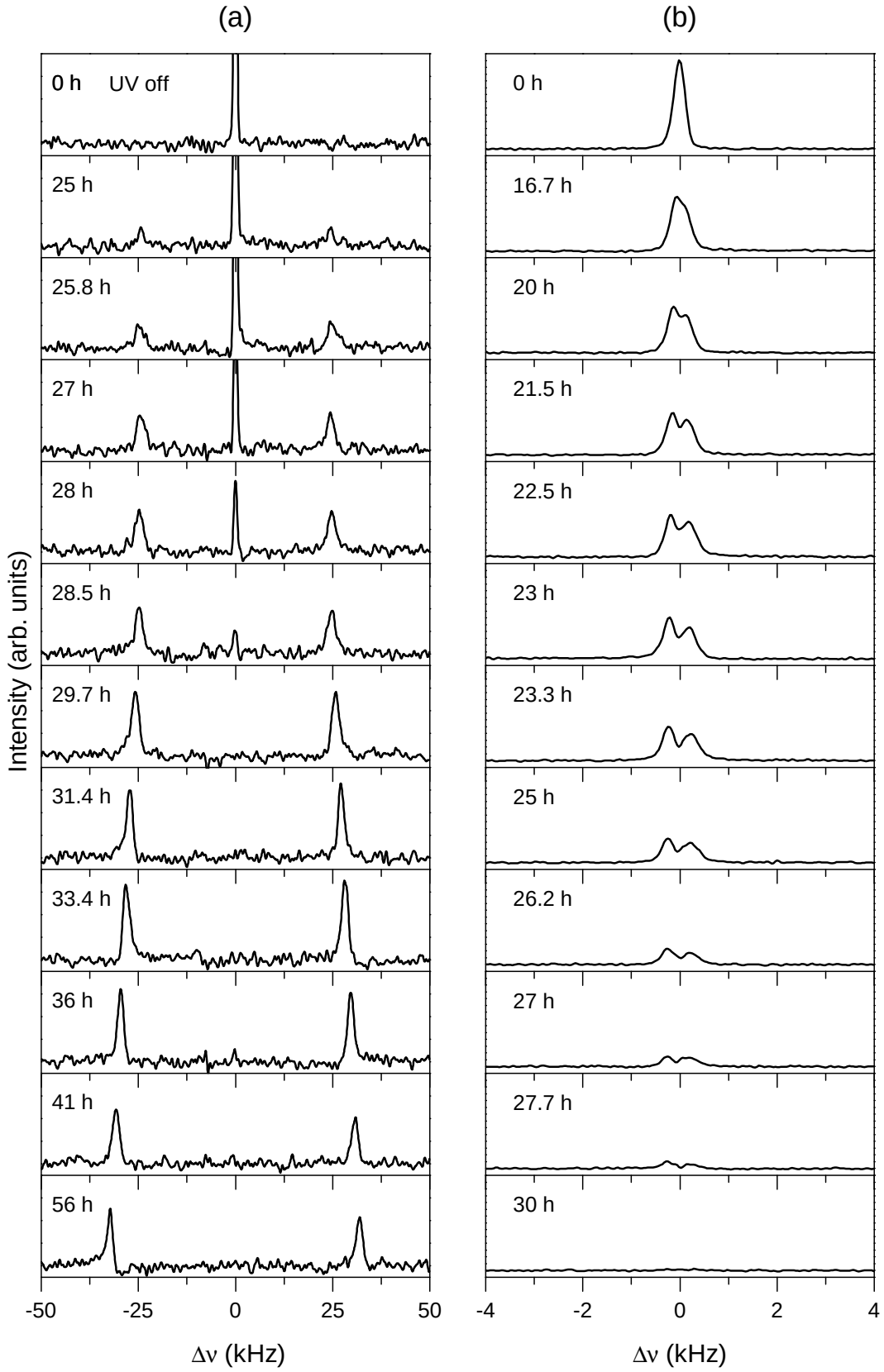

Figure 4.24 *Spectra recorded during the thermal backisomerization of 7AB at* 310 *K (a). The magnification of central line shows the surface-induced splitting (b).*

collimated. Time dependencies of photoisomerization and backisomerization processes were recorded at several temperatures with all other experimental parameters being identical. The illumination time was always 5.2 h which was long enough to reach cis concentrations close to 1. A typical sequence of spectra recorded at 310 K is shown in Fig. 4.24. In contrast to bulk photoisomerization measurements, a splitting of the isotropic line can be observed. The splitting is characteristic of confined liquid crystals, as already explained in section 4.3.1. During the illumination, however, the splitting completely disappears due to high concentration of cis molecules which destroy the surface-induced order. This state could not be established thermally since the splitting of the isotropic line persisted even at temperatures as high as 360 K.

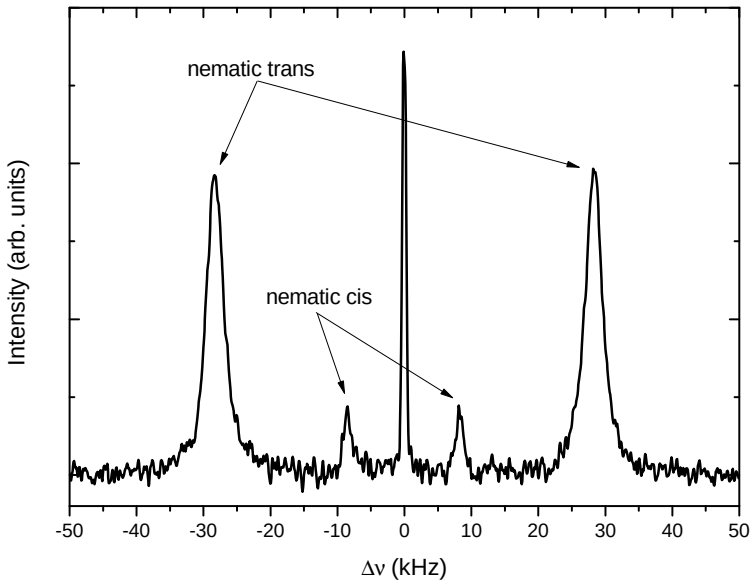

Figure 4.25 *Deuteron NMR spectrum of photoisomerized 7AB at $T = 302$ K, revealing three major components. In the isotropic phase, trans and cis components could not be resolved, whereas they are clearly distinguishable in the nematic phase.*

In the spectra of Fig. 4.24, the nematic cis doublet, present in bulk measurements, could not be resolved. The apparent absence of the doublet is however only due to the low signal-to-noise ratio of experiment with low amount of material. However, by averaging 15 successive spectra, the cis doublet becomes clearly visible (see Fig. 4.25). The spectra were taken at the time of maximal nematic cis concentration. In addition, the temperature was set to 302 K as the nematic cis concentration is higher at low temperatures.

In Fig. 4.26, the temperature dependence of the trans-doublet splittings is shown. The illumination was switched off at $t = 0$. The order parameters in both isotropic and nematic phases were determined by fitting with a double Lorentzian line. At $t = 0$ there are predominantly cis molecules in the sample and no splitting can be detected. When the cis concentration decreases, the splitting of the isotropic line increases so that it can be detected in the spectrum. The splitting then further increases and at temperatures above T_{NI} saturates at a value corresponding to zero-cis order. At temperatures below T_{NI}, the splitting does not saturate since the coexistence region is reached. In this region, a nematic doublet appears. It is important to note that both isotropic and nematic splittings are constant in the coexistence region. This is due to the constant cis concentrations in both phases as predicted by Eq. (2.39). When the concentration drops, the isotropic line disappears and the nematic splitting starts to increase. This process continues until saturated orientational order of trans molecules with zero concentration of cis molecules is established.

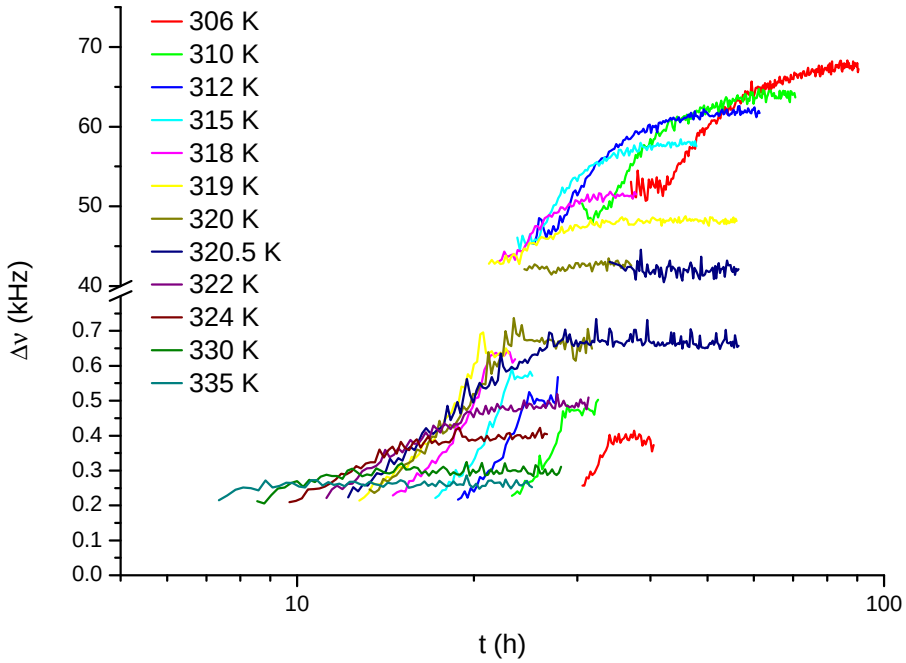

Figure 4.26 *Time dependence of the nematic and the surface-induced splitting during the backisomerization process. The temperature was varied from* 302 *to* 340 *K.*

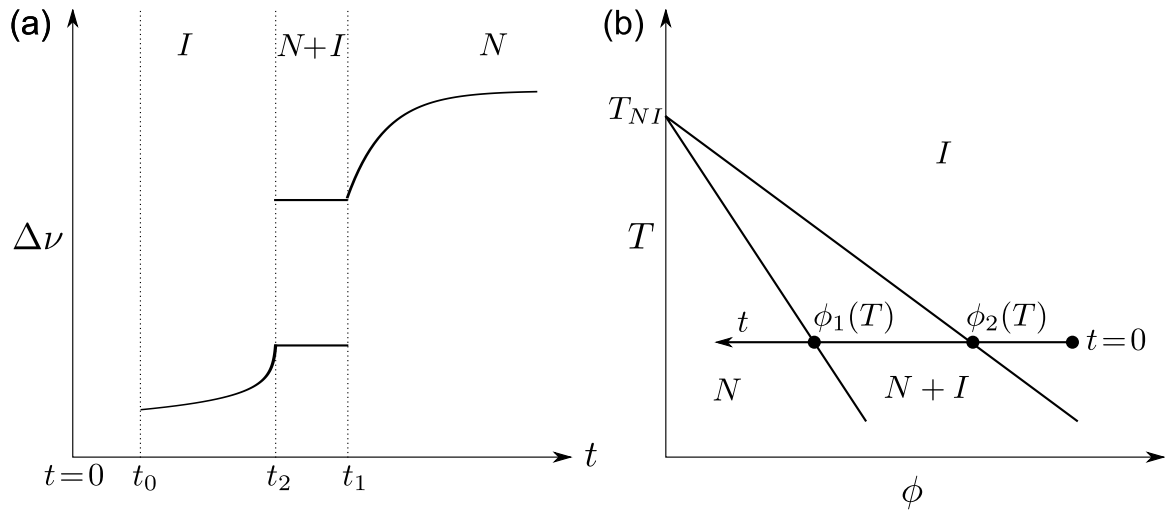

Figure 4.27 *Schematic representation of the splitting in a typical photoisomerization experiment at a temperature below T_{NI} (a). Time-line in a phase diagram, corresponding to such an experiment, crossing the three characteristic regions I, N+I and N (b).*

The observed behavior is schematically depicted in Fig. 4.27a. The experiment starts at $t = 0$. At t_0 the surface-induced splitting increases to the level that can be detected by our experimental equipment. The two characteristic times t_1 and t_2 correspond to critical concentrations ϕ_1 and ϕ_2 at which the transitions from N to N+I and N+I to I regions of the phase diagram take place, respectively. The same experiment is shown again in the T-ϕ phase diagram (Fig. 4.27b).

Except for the splitting of the isotropic line due to surface-induced order, there was no other evidence within our rather limited experimental resolution, that confined samples behave differently from the bulk. We anticipate that additional quantitative differences between the phase diagram of bulk and confined system could be resolved in a high-resolution NMR experiment. For instance, cis and trans isomers may become resolvable in the isotropic component of the spectrum through a difference in spin relaxation rates.

Due to the fact that we were unable to fully photoisomerize the a bulk sample (see section 4.2.3), it was impossible to prove that the phase diagrams of the two systems are the same. For this reason, we built a flat liquid crystal cell with approximately the same dimensions as those of the Anopore membranes used for confining the liquid crystal. The spacing inside the cell was determined to be 55 μm which is only 5 μm less than the specified thickness of Anopore membranes. Although the liquid crystalline material inside such a cell can still be considered as bulk, it can be fully photoisomerized because of small thickness of the cell. The results of studies of the material inside a thin cell could therefore be directly compared to the results of measurements of confined system (presented in Fig. 4.26). As expected, the isotropic line measured in a thin cell did not exhibit any splitting. As is evident from Fig. 4.28, the time evolution of nematic splittings for both samples measured at the same conditions is almost identical. The presented result supports the assumption that the same theoretical model (described in section 2.2) can be used to describe the phase separation behavior and nematic ordering in both confined and bulk samples.

Time dependencies of the volume fraction of the isotropic phase are given in Fig. 4.29. They were used to determine the T-ϕ phase diagram of 7AB, which encompasses nematic (N), isotropic (I) and coexistence (N+I) regions. In terms of deuteron NMR experiment, performed during the backisomerization of fully photoisomerized 7AB, the N+I coexistence region is entered whenever the intensity of the isotropic component in the spectrum starts to decrease in parallel with the appearance of nematic doublets (trans and cis). By analyzing the data of

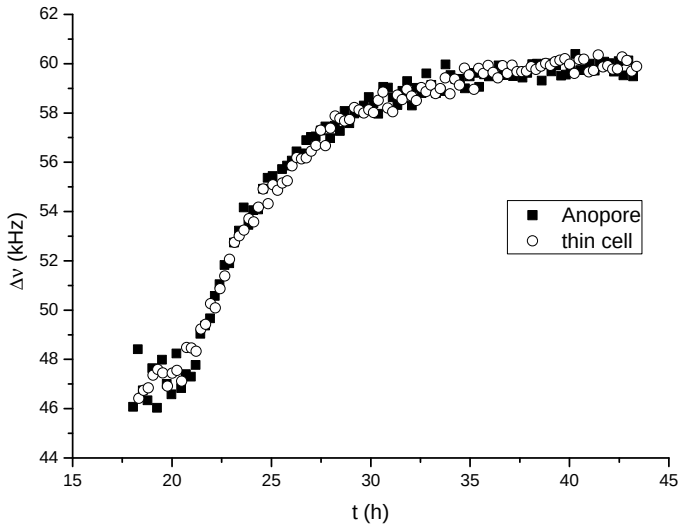

Figure 4.28 *The comparison of time dependencies of nematic splittings in confined Anopore geometry and in thin cell at* 315 *K.*

Fig. 4.29, it is straightforward to determine the temperature-time phase diagram. In order to discern the temperature-concentration phase diagram, one just needs to map the time into the concentration, i.e. the relation $\phi(t)$ should be known. Taking into account the quasi-stationary nature of our experiment, it is possible to assume that, due to slow backisomerization, our system is always in the quasi-equilibrium state. Moreover, since a typical signal accumulation time in the deuteron NMR experiment is much shorter than the characteristic decay time of cis population (minutes vs. hours), each individual accumulation of a NMR spectrum can be considered to probe a well-defined point in the T-ϕ plane.

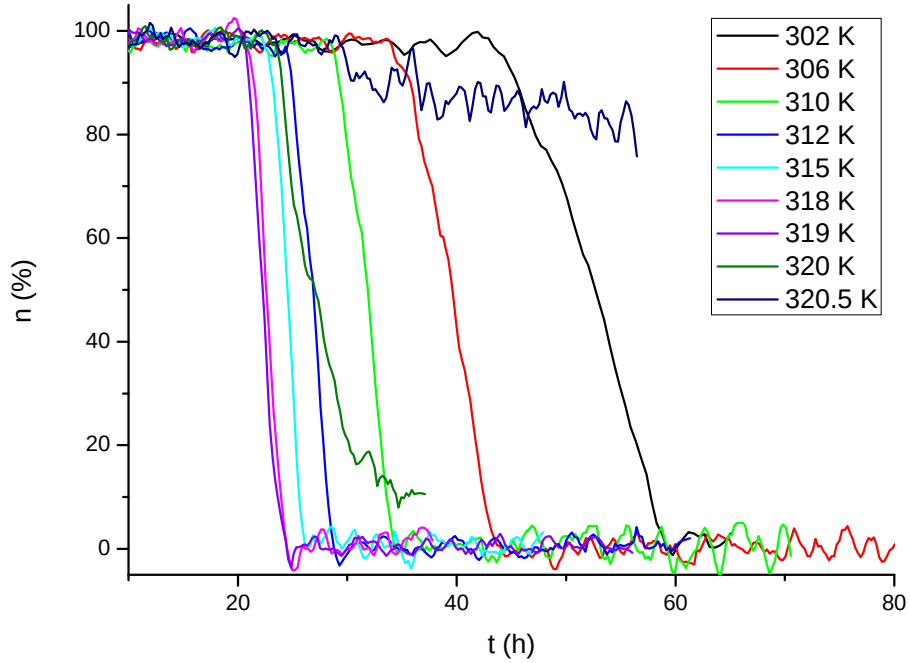

Figure 4.29 *Temperature and time dependencies of volume fraction of the isotropic phase used in the determination of the T-t phase diagram.*

4.4 Determination of the T-ϕ phase diagram

In order to address the problem of calculating the time dependence of cis concentration, measurements of bulk and confined system were compared. It was argued in section 2.2 that the surface-induced ordering does not have significant impact on the free energy of the system due to low value of the order parameter. This hypothesis was confirmed with experiments performed on a thin cell. The phase separation processes of bulk and confined samples is thus qualitatively and quantitatively similar, justifying the assumption that the results obtained with the bulk systems are also valid for confined systems.

As shown in section 4.2.3, exact cis concentration can be determined in bulk samples from the spectrum at the moment when the isotropic phase disappears. The experimental data was acquired in a temperature range from 300 to 318 K in 3 K steps. This measurement was used to determine the $\phi_1(T)$ line which separates coexistence and nematic regions. In confined samples, $t_1(T)$ curve corresponding to the $\phi_1(T)$ line can be extracted. The combined $t_1(T)$ and $\phi_1(T)$ data thus implicitly define the $\phi_1(t_1)$ relationship.

The relaxation process in the photoisomerizable material is due to thermal backisomerization for which an exponential decay is assumed, according to Eq. (1.35). Cis concentration at any

time is given by:

$$\phi = \phi_0 e^{-t/\tau} \tag{4.4}$$

It should be noted that the relaxation time τ depends on the temperature. The temperature dependence of the reaction rate $1/\tau$ is described by the Arrhenius law, which states:

$$\frac{1}{\tau} = Ae^{-\frac{E_a}{kT}} \tag{4.5}$$

The activation energy is denoted by E_a and A is the pre-exponential factor. In order to determine the reaction rate from Eq. (4.4), at least two points of the $\phi(t)$ dependence have to be known. The point (t_1, ϕ_1) was determined from direct measurements of cis population in the bulk, whereas the other point is given by the initial cis concentration at $t = 0$. Since it was shown that the cis concentration gets saturated at long illumination times, we can assume that the initial cis concentration is $\phi_0 = 1$.

By combining equations (4.4) and (4.5) we obtain the following dependence:

$$\ln\left(-\frac{\ln\phi}{t}\right) = \ln A - \frac{E_a}{k}\frac{1}{T} \tag{4.6}$$

When a logarithm of the reaction rate is plotted versus inverse temperature, a linear dependence is obtained. The measurements recalculated according to Eq. (4.6), are presented in Fig. 4.30. The data can easily be fitted with a straight line which confirms the Arrhenius type behavior of the backisomerization process. The activation energy is estimated to be 0.68 eV which is close to the value of 0.9 eV found in the literature for derivatives of azobenzene [80]. Once the activation energy E_a and pre-factor A are known, the cis concentration in confined system can be determined for any time during the relaxation.

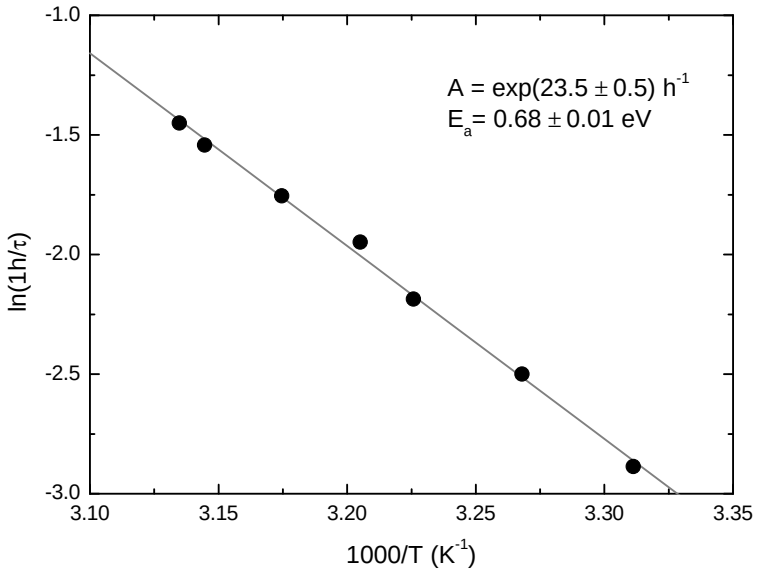

Figure 4.30 *Arrhenius law fit of the thermal backisomerization process.*

With a known $\phi(t)$ relationship, it is possible to test the theoretical predictions of the models presented in section 2.2. Five different data sets were modeled:

- temperature dependence of the nematic order parameter (Fig. 4.31)
- temperature dependence of the surface-induced order parameter (Fig. 4.33)

- concentration dependence of the nematic order parameter at different temperatures (Fig. 4.32)
- concentration dependence of the surface-induced order parameter at different temperatures (Fig. 4.34)
- temperature-concentration phase diagram (Fig. 4.35)

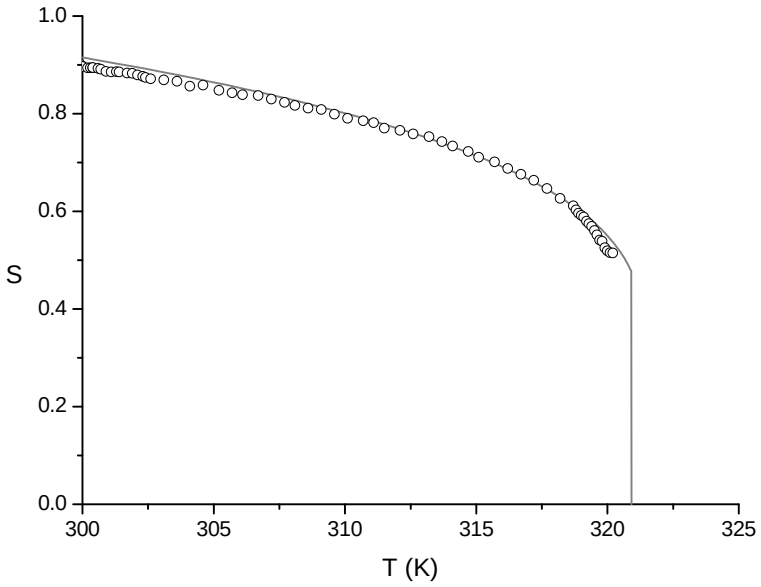

Figure 4.31 *Best fit of the temperature dependent nematic order parameter of trans molecules.*

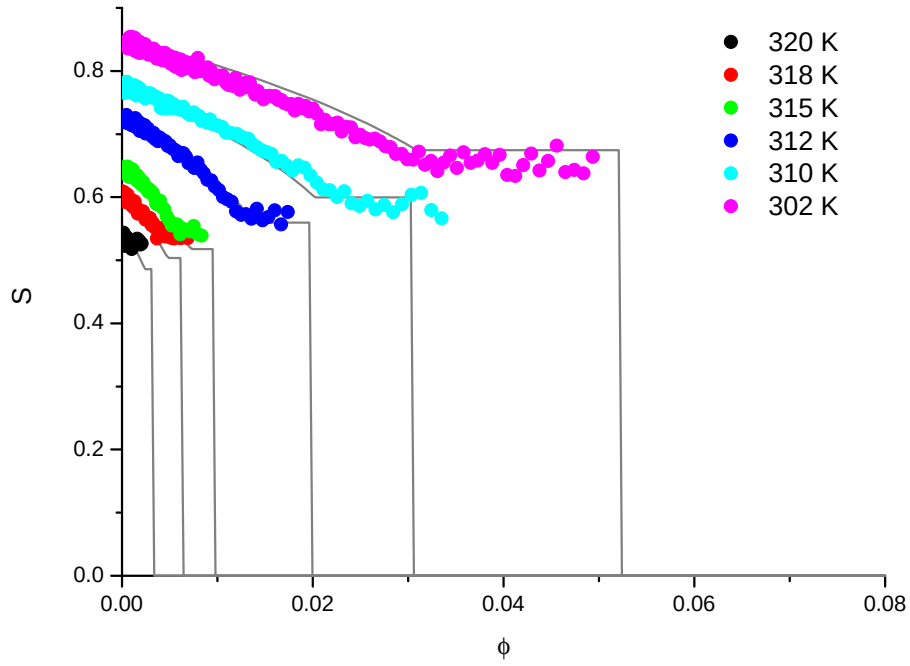

Figure 4.32 *The agreement between the experimental data and the theoretical prediction for nematic order parameter as a function of cis concentration.*

The models for different data are not independent. The temperature and concentration dependencies use the same model for the order parameter $S(T,\phi)$ by setting either $T = const$.

or $\phi = 0$, respectively. Furthermore, some of the parameters used in separate descriptions must be the same. The model for the nematic order is given by Eq. (2.29) whereas the average surface-induced order in the isotropic phase is described by (2.36). Finally, the phase diagram can be modeled by calculating the total free energy and using bitangent method to determine boundary concentrations.

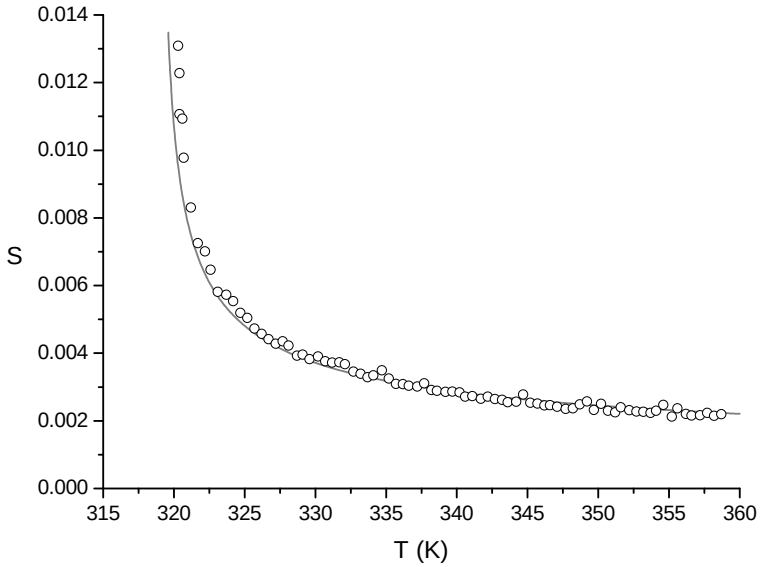

Figure 4.33 *Best fit of the temperature dependence of the surface-induced order parameter at* $\phi = 0$.

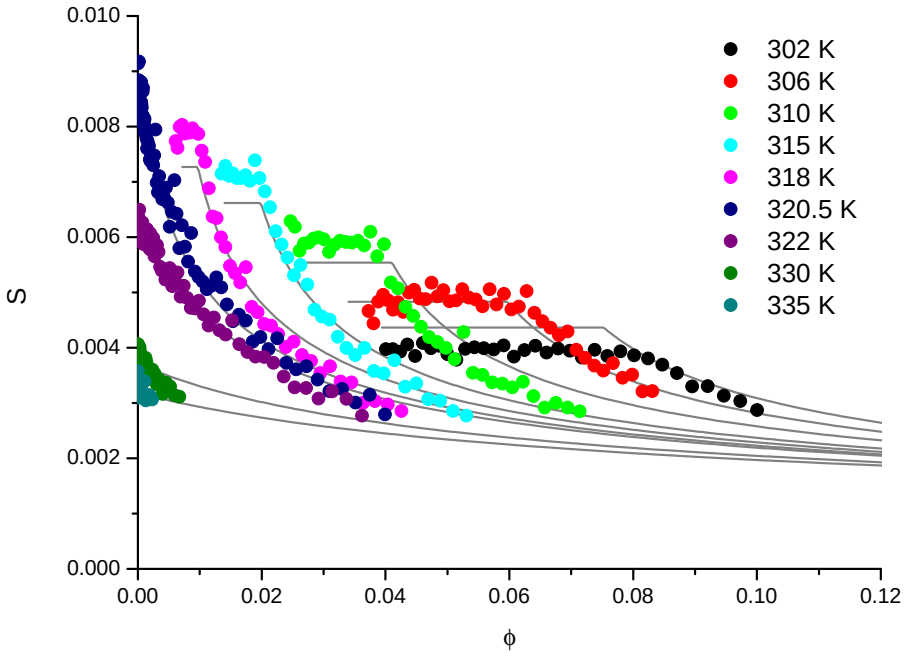

Figure 4.34 *Best fits of the surface-induced order parameters in the isotropic phase of a binary mixture.*

From the temperature dependence of the nematic order parameter in Fig. 4.31, the Landau-de Gennes parameters a, B, E and T^* were determined. The same parameters were then used when fitting the set of concentration dependence measurement at different temperatures (Fig. 4.32). The only free parameter that could be varied in this case was the interaction parameter between the trans molecules U. The values of the parameters are given in table 4.2. Fig. 4.32 is an

Table 4.2 *Best fit parameters used in the theoretical description of nematic and surface-induced ordering, as well as phase separation in a binary trans-cis 7AB liquid crystal.*

T^* (K)	a (K^{-1})	B	E	U	S_0	$\tilde{r}_0$	R_1 (K^{-1})	U_0 (10^{-3} eV)
319	0.02	0.18	0.8	6.9	0.072	0.004	181	9.4

equivalent of Fig. 4.26, with $\Delta\nu$ expressed in terms of the order parameter S and time t expressed in terms of concentration ϕ.

The same procedure as before was used to model the surface-induced order. First, the temperature dependence (Fig. 4.33) was fitted to determine parameters S_0, $\tilde{r}_0$ and R_1. The value of the temperature T^* was taken from table 4.2, so that the only free parameter was R_2. However, since parameters R_1 and R_2 must have the same ratio as parameters a and U, R_2 is predetermined via $R_1 U/a$. Best fits of the concentration-dependent surface-induced order parameter vs. concentration are shown in Fig. 4.34. Although they are not ideal, we can see that the expanded theoretical model of section 2.2 adequately describes the behavior of both nematic and surface-induced order on varying the temperature and concentration.

Fig. 4.35 shows experimentally determined phase diagram of diheptylazobenzene, together with the best fit to the theoretical model. Three distinct regions, N, I and N+I, are clearly visible in the diagram. We observe that the coexistence region forms at relatively low cis concentrations, below 10%. Furthermore, the phase boundary lines $\phi_1(T)$ and $\phi_2(T)$ are relatively steep. This explains the sensitivity of the material on minute changes of light intensity.

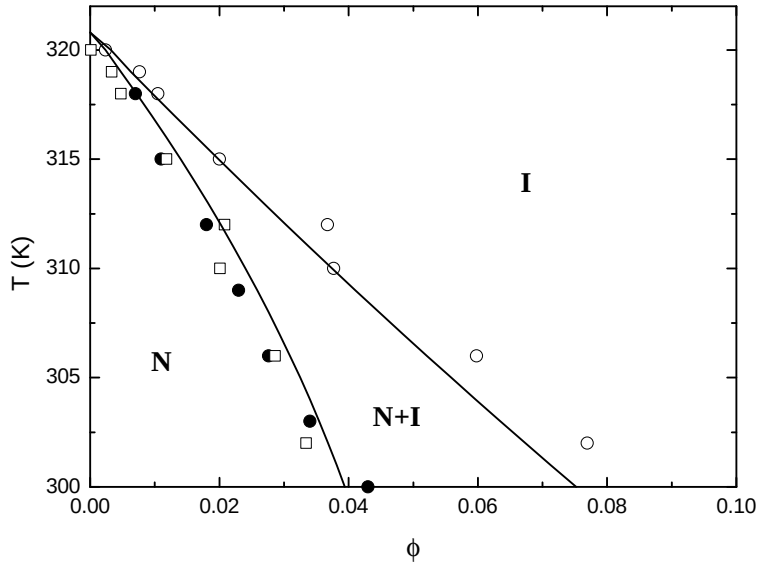

Figure 4.35 *The phase diagram of diheptylazobenzene. Black circles are direct measurements of the cis concentration from the bulk, open circles and open squares are determined from thermal relaxation measurements in Anopores and the lines show theoretical predictions.*

The phase diagram was fitted using the same parameters as above. The only parameter varied was the interaction term U_0 in the free energy of mixing. As evident from Eq. (2.6), the interaction term U_0 and the temperature T determine the value of the free energy of mixing. It is the competition between the free energy of mixing and the nematic free energy which determines when the phase separation will occur. The phase separation behavior, specifically the concentration dependence of the phase boundary lines $\phi_1(T)$ and $\phi_2(T)$, can therefore be modeled solely by varying U_0.

All the dimensionless parameters of table 4.2 must be multiplied by U_0 when calculating the free energy per molecule. To check if reasonable values are obtained for the parameters in table 4.2, we shall compare them to the values characteristic for a conventional nematogen, e.g. 5CB. Parameters were recalculated into a dimensionless form using $\rho_{5CB} = 1.38$ g/cm^3, $M_{5CB} = 249.4$ g/mol and $\tilde{x} = xM/(U_0 N_A \rho)$, where x is a parameter from table 1.1. The comparison of the data shown in table 4.3 confirms that plausible parameter values were obtained for 7AB.

Table 4.3 *Comparison of Landau-de Gennes parameters between 7AB and 5CB.*

	7AB	5CB
ΔT (K)	2.1	1.1
a (K^{-1})	0.02	0.26
B	0.18	0.32
R_1 (K^{-1})	181	988

By comparing the experimental data and theoretical predictions, we conclude that both nematic and surface-induced order of 7AB can be controlled by either temperature or concentration of cis molecules. A question then arises about the sensitivity of the order parameter on these externally controllable parameters, specifically how the change in the temperature can be mapped into the change in concentration or vice versa. In order to answer this question, let us analyze the temperature and concentration dependence of the nematic order parameter $S(T,\phi)$ given by Eq. (2.29) and of the average surface-induced orientational order parameter $< S > (T,\phi)$ given by Eq. (2.36). As far as orientational ordering is concerned, the system is considered to be in the same state whenever the order parameter remains constant while the external parameters T and ϕ are varied. It is straightforward to show that this is the case with $S(T,\phi)$ and $< S > (T,\phi)$ if the two respective effective temperatures

$$T_{ef}^{S}(T,\phi) = T + \frac{U}{a}\phi \tag{4.7}$$

and

$$T_{ef}^{<S>}(T,\phi) = \frac{T + (U/a - T^*)\phi}{1-\phi} \tag{4.8}$$

are kept at a constant value T_0. This requirement is satisfied whenever the following holds:

$$\begin{aligned} T^{S}(\phi) &= T_0 - \frac{U}{a}\phi \\ T^{<S>}(\phi) &= T_0 - (\frac{U}{a} + T_0 - T^*)\phi \end{aligned} \tag{4.9}$$

In both cases, the relationship between T and ϕ is linear. This prediction was tested experimentally and the result is presented in Fig. 4.36. We found a fairly good agreement between experiment and theory. The linear trend can clearly be seen. Let us stress that, outside the coexistence region, any two dimensional point (T,ϕ) can be mapped into a single parameter, i.e. its effective temperature $T_{ef}(T,\phi)$. The lyotropic behavior of the system, i.e. the dependence of the order parameter on the concentration of cis molecules ϕ can therefore be described by considering the thermotropic behavior with a single redefinition of temperature.

The presented results clearly show the main advantage of using confined samples. Using deuteron NMR, precise measurements of the order parameters are possible. Consequently, more detailed information is obtained than by solely studying the phase diagram. Since the order parameter at constant temperature depends only on the concentration of cis molecules,

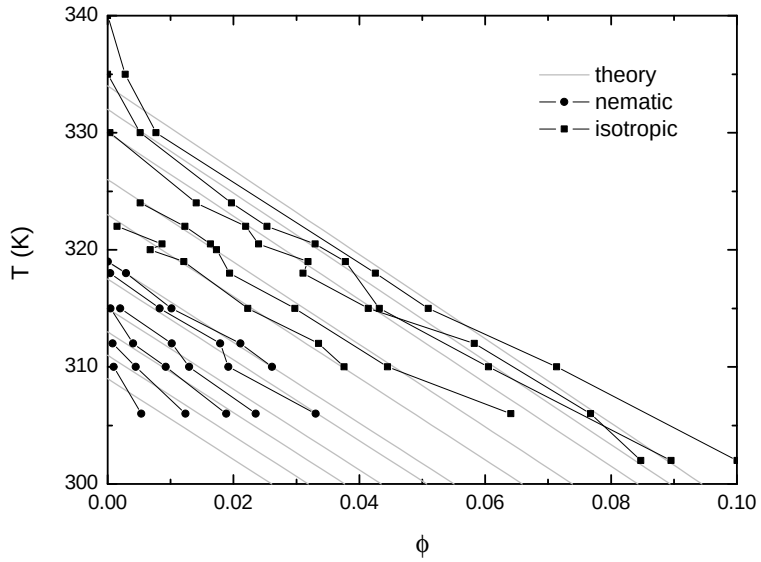

Figure 4.36 *The lines of constant orientational order parameters in nematic and isotropic phase. Black lines serve only as a guide to the eye.*

the concentration can be determined at any time simply by measuring at the splitting of the nematic doublet. Unfortunately, nematic phase exists only at relatively low cis concentrations. In confined samples, the surface-induced ordering exists high above the nematic-to-isotropic transition concentration. Much wider concentration ranges can thus be measured directly.

5 Conclusions

We have successfully applied deuteron NMR for the study of phase separation behavior of photoisomerized liquid crystals, specifically of the 7AB nematogenic azodye. The so far elusive temperature-concentration phase diagram of dynamically controlled binary trans-7AB and cis-7AB mixture has been determined by comparative analysis of the behavior in bulk, thin planar cell, and Anopore confining geometries.

First, in order to optimize photoisomerization parameters, UV-VIS spectroscopy of bulk 7AB material was performed. The absorption spectrum reveals absorption peaks corresponding to trans-to-cis and cis-to-trans photoisomerization positioned at 332 nm and 439 nm, respectively. No significant departure from the values obtained in solutions has been observed. The penetration depth, measured by wedge cell, exhibits a local minimum at the cis-to-trans absorption peak wavelength with the value about 2.5 μm, whereas the extrapolated penetration depth at the wavelength of the trans-to-cis absorption peak is estimated at few 100 nm. These measurements clearly demonstrate that, in bulk samples, photoisomerization only takes place at the surface, making it impossible for quantitative analysis and accurate control of the photoisomerization induced phase separation. However, due to spatial separation of isotropic and nematic phases, driven by the difference in their respective mass densities, it is possible to reach relatively high cis concentrations with thin enough samples. Some qualitative characterization of the photoisomerization-driven response is thus nevertheless possible in a bulk system.

Digital imaging proved to be particularly useful in the design of a photoisomerization experiment. This is so since the isotropic-to-nematic and the reverse conversion, induced by UV illumination stimulated trans-to-cis isomerization and thermally induced cis-to-trans backisomerization, respectively, are visible by the naked eye, the coexistence of transparent isotropic phase and opaque nematic phase being the most significant feature. Digital imaging experiments are reminiscent of a typical demixing behavior, with an ideally mixed isotropic phase at high temperatures and onset of nematic order characterized by a wide nematic-isotropic coexistence region on lowering the temperature below T_{NI}. The existence of the three regions in the phase diagram, specifically the nematic phase at low temperature, the isotropic phase at high temperatures, and the wide coexistence region supports the conjecture that photoisomerized 7AB can be theoretically modeled as a binary nematogen using combined theories of isotropic mixing and Landau de Gennes nematic ordering. In order to prove that in a quantitative way, deuterium NMR was employed.

The analysis of the temperature dependence of the deuterium quadrupole-perturbed NMR provides for a straightforward identification of the three characteristic regions of the phase diagram. The sharp central peak at the deuteron Larmor frequency is attributed to isotropic phase. Cis and trans isomers could not be resolved in this spectral line. On the contrary, the nematic state is visible in the spectrum as two coexisting doublets, attributed to the two isomers. The areas of the spectral doublets therefore mirror directly the relative populations the two respective 7AB species, i.e. the cis concentration ϕ. The presence of the cis doublet confirms the interplay between both isomers, taken into account in the theoretical modeling via the bi-linear $S_t S_c$ free energy term. The observed time-dependent changes of the relative intensities of spectral peaks can be directly associated with the photoisomerization-induced changes of the cis concentration

which were either stimulated by UV-illumination (trans-to-cis conversion) or allowed to take place spontaneously through thermal backisomerization (cis-to-trans conversion). Unfortunately, NMR measurements in bulk 7AB can not be used for a quantitative analysis of the phase diagram due to extremely small penetration depth of UV light, resulting in a spatially inhomogeneous cis concentration.

The above problem was resolved by confining 7AB to cylindrical channels of Anopore membranes. The flat geometry of membranes allows for easy implementation of uniform illumination. Moreover, the membranes are so thin that we were able to fully cis-isomerize the 7AB system. Consequently, since the initial value of ϕ (100%) was known, quantitative mapping of time into cis concentration was possible. In all experiments, we were able to model the $\phi(t)$ dependence as an exponential decay, with an Arrhenius-type characteristic time. The activation energy was determined to be $E_a = 0.68$ eV. The condition with homogeneous 100% cis concentration is not accessible in a bulk system with small penetration depth of UV light. Let us stress that the temperature-concentration phase diagram could only be successfully determined by performing the measurements in the absence of UV illumination, i.e. in the backisomerization regime, since during the illumination significant sample heating occurs due to non-resonant absorption of light. Moreover, since the timescale of the backisomerization process is several hours, deuteron NMR experiments can be performed in a quasi-equilibrium regime, i.e. even with experiments demanding extensive signal accumulation, sharp points in the temperature-concentration phase diagram can be sampled.

The temperature dependence of deuteron NMR spectra of confined samples displays a phase transition behavior similar to the one found in the bulk. In addition, the isotropic peak is split in a similar way as in conventional, single-component confined nematogens. The respective surface-induced order parameter $< S >$ exhibits strong dependence on cis concentration. The measurements of angular dependence of deuteron NMR spectra reveal a parallel axial configuration of the nematic director.

The experimental results for Anopore-confined 7AB can be consistently explained with Landau-de Gennes theory, extended by including the concentration-dependent terms and spatially variable order parameter in the isotropic phase. It is found that the influence of the cis ordering on the trans order is not significant, so that cis isomers can be treated as non-mesogenic solutes.

As anticipated for a binary nematic, the individual order parameters of the coexisting nematic and isotropic phases, i.e. S and $< S >$, respectively, remain constant when the concentration is varied isothermally, equivalently the isonematic lines in the coexistence region are horizontal. This is so since the individual cis concentrations of the two coexisting phases remain constant.

It was experimentally confirmed that, out of the coexistence region, a simple linear relationship exists between temperature and concentration for the order parameters to remain constant. Equivalently, changes in concentration can be linearly mapped into changes of temperature.

In conclusion, photoisomerized 7AB turned out to be a convenient system for investigation of combined thermotropic and lyotropic behavior of nematogenic mixtures. The ratio of trans and cis isomers can be accurately controlled by photoisomerization of Anopore-confined 7AB. We thus deal with a model system for the investigation of temperature-concentration phase diagram of binary nematogens, where the concentration can be controlled dynamically. In spite of sub-micron confining geometry, the phase separation behavior still resembles that of a bulk system. The ability of localized manipulation of nematic order by simultaneous control of temperature and concentration may be important for applications in micro- and nano-mechanical systems.

6 Acknowledgements

First, I would like to thank my advisor prof. dr. Boštjan Zalar for introducing me to the field of experimental NMR. The numerous discussions we had, as well as his suggestions kept me on the right path to complete this work.

Special thanks go to the other people that are, or at one time were, members of our experimental group: dr. Andrija Lebar helped me with the NMR measurements and theoretical modeling of liquid crystals, dr. Valentina Domenici was invaluable with explanations of the chemical aspects of our materials and dr. Martin Chambers assisted me with initial illumination setups and introduced me to the wonders of Blu-Tack.

Next, I would like to express my gratitude to the members of Department of Solid State Physics, many of which helped me in the course of my work by lending me some of their time or their experimental equipment.

I thank prof. dr. Daniele Finotello for inviting and hosting me at the Liquid Crystal Institute. It was during the four months abroad that my work with confined systems started. I thank dr. Sergio Diez Berart for helping me with initial measurements.

7 References

[1] de Gennes, P. G.; Prost, J., *The physics of liquid crystals* (Oxford University Press, New York, 1993).

[2] Stephen, M. J.; Straley, J. P., Physics of liquid crystals. *Reviews of Modern Physics* **46**, 617 (1974).

[3] Chigrinov, V. G., *Liquid crystal devices: physics and applications* (Artech House, Boston, 1999).

[4] Crawford, G. P.; Žumer, S., *Liquid crystals in complex geometries: formed by polymer and porous networks* (Taylor & Francis, London, 1996).

[5] Kityk, A. V.; Wolff, M.; Knorr, K.; Morineau, D.; Lefort, R.; Huber, P., Continuous Paranematic-to-Nematic Ordering Transitions of Liquid Crystals in Tubular Silica Nanochannels. *Physical Review Letters* **101**, 187801 (2008).

[6] Moses, T.; Shen, Y. R., Pretransitional surface ordering and disordering of a liquid crystal. *Physical review letters* **67**, 2033 (1991).

[7] Steuer, H.; Hess, S.; Schoen, M., Phase behavior of liquid crystals confined by smooth walls. *Physical Review E* **69**, 31708 (2004).

[8] Sheng, P., Boundary-layer phase transition in nematic liquid crystals. *Physical Review A* **26**, 1610 (1982).

[9] Crawford, G. P.; Ondris-Crawford, R. J.; Doane, J. W.; Žumer, S., Systematic study of orientational wetting and anchoring at a liquid-crystal-surfactant interface. *Physical Review E* **53**, 3647 (1996).

[10] Kossyrev, P. A.; Crawford, G. P., The birefringent texture of nematic liquid crystals confined to capillary tubes with square cross-section. *Molecular crystals and liquid crystals* **351**, 379 (2000).

[11] Bellini, T.; Radzihovsky, L.; Toner, J.; Clark, N. A., Universality and scaling in the disordering of a smectic liquid crystal. *Science* **294**, 1074 (2001).

[12] Iannacchione, G. S.; Crawford, G. P.; Žumer, S.; Doane, J. W.; Finotello, D., Randomly constrained orientational order in porous glass. *Physical review letters* **71**, 2595 (1993).

[13] Doane, J. W.; Vaz, N. A.; Wu, B. G.; Žumer, S., Field controlled light scattering from nematic microdroplets. *Applied Physics Letters* **48**, 269 (1986).

[14] Drzaic, P. S., Polymer dispersed nematic liquid crystal for large area displays and light valves. *Journal of Applied Physics* **60**, 2142 (1986).

[15] Shah, R. R.; Abbott, N. L., Principles for measurement of chemical exposure based on recognition-driven anchoring transitions in liquid crystals. *Science* **293**, 1296 (2001).

[16] McCamley, M. K.; Ravnik, M.; Artenstein, A. W.; Opal, S. M.; Žumer, S.; Crawford, G. P., Detection of alignment changes at the open surface of a confined nematic liquid crystal sensor. *Journal of Applied Physics* **105**, 123504 (2009).

[17] Lebar, A.; Kutnjak, Z.; Tanaka, H.; Zalar, B.; Žumer, S., Phase separation in nematic microemulsions probed by one-dimensional spectroscopic deuteron magnetic resonance microimaging. *Physical Review E* **78**, 31707 (2008).

[18] Loudet, J. C.; Barois, P.; Poulin, P., Colloidal ordering from phase separation in a liquid-crystalline continuous phase. *Nature* **407**, 611 (2000).

[19] Yamamoto, J.; Tanaka, H., Transparent nematic phase in a liquid-crystal-based microemulsion. *Nature* **409**, 321 (2001).

[20] Ikeda, T.; Tsutsumi, O., Optical switching and image storage by means of azobenzene liquid-crystal films. *Science* **268**, 1873 (1995).

[21] Yu, Y.; Nakano, M.; Ikeda, T., Directed bending of a polymer film by light. *Nature* **425**, 145 (2003).

[22] Domenici, V.; Ambrožič, G.; Čopič, M.; Lebar, A.; Drevenšek-Olenik, I.; Umek, P.; Zalar, B.; Zupančič, B.; Žigon, M., Interplay between nematic ordering and thermomechanical response in a side-chain liquid single crystal elastomer containing pendant azomesogen units. *Polymer* **50**, 4837 (2009).

[23] Devetak, M.; Zupančič, B.; Lebar, A.; Umek, P.; Zalar, B.; Domenici, V.; Ambrožič, G.; Žigon, M.; Čopič, M.; Drevenšek-Olenik, I., Micropatterning of light-sensitive liquid-crystal elastomers. *Physical Review E* **80**, 50701 (2009).

[24] Woltman, S. J.; Jay, G. D.; Crawford, G. P., Liquid-crystal materials find a new order in biomedical applications. *Nature Materials* **6**, 929 (2007).

[25] Choi, B. Y.; Kahng, S. J.; Kim, S.; Kim, H.; Kim, H. W.; Song, Y. J.; Ihm, J.; Kuk, Y., Conformational molecular switch of the azobenzene molecule: a scanning tunneling microscopy study. *Physical review letters* **96**, 156106 (2006).

[26] Muraoka, T.; Kinbara, K.; Aida, T., Mechanical twisting of a guest by a photoresponsive host. *Nature* **440**, 512 (2006).

[27] Beharry, A. A.; Sadovski, O.; Woolley, G. A., Photo-control of peptide conformation on a timescale of seconds with a conformationally constrained, blue-absorbing, photoswitchable linker. *Organic & Biomolecular Chemistry* **6**, 4323 (2008).

[28] Pons, T.; Moreaux, L.; Mertz, J., Photoinduced flip-flop of amphiphilic molecules in lipid bilayer membranes. *Physical review letters* **89**, 288104 (2002).

[29] van Oosten, C. L.; Bastiaansen, C. W. M.; Broer, D. J., Printed artificial cilia from liquid-crystal network actuators modularly driven by light. *Nature Materials* **8**, 677 (2009).

[30] Urban, S.; Gestblom, B.; Kuczyński, W.; Pawlus, S.; Würflinger, A., Nematic order parameter as determined from dielectric relaxation data and other methods. *Physical Chemistry Chemical Physics* **5**, 924 (2003).

[31] Hamley, I. W.; Garnett, S.; Luckhurst, G. R.; Roskilly, S. J.; Sedon, J. M.; Pedersen, J. S.; Richardson, R. M., Orientational ordering in the nematic phase of a thermotropic liquid crystal: A small angle neutron scattering study. *The Journal of Chemical Physics* **104**, 10046 (1996).

[32] Ondris-Crawford, R. J.; Crawford, G. P.; Doane, J. W.; Žumer, S.; Vilfan, M.; Vilfan, I., Surface molecular anchoring in microconfined liquid crystals near the nematic–smectic-A transition. *Physical Review E* **48**, 1998 (1993).

[33] Tazuke, S.; Kurihara, S.; Ikeda, T., Amplified image recording in liquid crystal media by means of photochemically triggered phase transition. *Chemistry Letters* **16**, 911 (1987).

[34] Zalar, B.; Lavrentovich, O. D.; Zeng, H.; Finotello, D., Deuteron NMR investigation of a photomechanical effect in a smectic-A liquid crystal. *Physical Review E* **62**, 2252 (2000).

[35] Attard, G. S.; Emsley, J. W.; Khoo, S. K.; Luckhurst, G. R., Pre-transitional behaviour in the isotropic phase of nematogenic mixtures: on NMR investigation. *Chemical physics letters* **105**, 244 (1984).

[36] de Gennes, P. G., Short range order effects in the isotropic phase of nematics and cholesterics. *Molecular Crystals and Liquid Crystals* **12**, 193 (1971).

[37] Kleman, M.; Lavrentovich, O. D., *Soft Matter Physics: An Introduction* (Springer-Verlag, New York, 2003).

[38] Coles, H. J., Laser and electric field induced birefringence studies on the cyanobiphenyl homologues. *Molecular Crystals and Liquid Crystals* **49**, 67 (1978).

[39] Stelzer, J.; Galatola, P.; Barbero, G.; Longa, L., Molecular dynamics simulations of surface-induced ordering in a nematic liquid crystal. *Physical Review E* **55**, 477 (1997).

[40] Miyano, K., Surface-induced ordering of a liquid crystal in the isotropic phase. *The Journal of Chemical Physics* **71**, 4108 (1979).

[41] Sheng, P., Phase transition in surface-aligned nematic films. *Physical Review Letters* **37**, 1059 (1976).

[42] Kutnjak, Z.; Kralj, S.; Lahajnar, G.; Žumer, S., Calorimetric study of octylcyanobiphenyl liquid crystal confined to a controlled-pore glass. *Physical Review E* **68**, 21705 (2003).

[43] Kralj, S.; Žumer, S., Saddle-splay elasticity of nematic structures confined to a cylindrical capillary. *Physical Review E* **51**, 366 (1995).

[44] Jin, T.; Zalar, B.; Lebar, A.; Vilfan, M.; Zumer, S.; Finotello, D., Anchoring and structural transitions as a function of molecular length in confined liquid crystals. *The European Physical Journal E: Soft Matter and Biological Physics* **16**, 159 (2005).

[45] Kralj, S.; Žumer, S., Smectic-A structures in submicrometer cylindrical cavities. *Physical Review E* **54**, 1610 (1996).

[46] Crawford, G. P.; Stannarius, R.; Doane, J. W., Surface-induced orientational order in the isotropic phase of a liquid-crystal material. *Physical Review A* **44**, 2558 (1991).

[47] Jin, T.; Crawford, G.; Crawford, R.; Zumer, S.; Finotello, D., Surface Ordering Transitions at a Liquid Crystal–Solid Interface above the Isotropic Smectic-A Transition. *Physical review letters* **90**, 15504 (2003).

[48] Poniewierski, A.; Sluckin, T. J., Statistical Mechanics of a Simple Model of the Nematic Liquid Crystal-Wall Interface. *Molecular Crystals and Liquid Crystals* **111**, 373 (1984).

[49] Ji, Q.; Lefort, R.; Busselez, R.; Morineau, D., Structure and dynamics of a Gay–Berne liquid crystal confined in cylindrical nanopores. *The Journal of Chemical Physics* **130**, 234501 (2009).

[50] Cheung, D. L.; Schmid, F., Monte Carlo simulations of liquid crystals near rough walls. *The Journal of chemical physics* **122**, 074902 (2005).

[51] Barbero, G.; Evangelista, L. R., Local self-consistent approach to the phase transition at the nematic liquid-crystal-wall interface. *Physical Review E* **65**, 31708 (2002).

[52] Ziherl, P.; Vilfan, M.; Vrbančič-Kopač, N.; Žumer, S.; Ondris-Crawford, R. J.; Crawford, G. P., Substrate-induced order in the isotropic phase of a smectogenic liquid crystal: A deuteron NMR study. *Physical Review E* **61**, 2792 (2000).

[53] Bahadur, B., *Liquid crystals: applications and uses* (World Scientific Publishing, Singapore, 1990).

[54] Luckhurst, G. R., Liquid crystals: a chemical physicist's view. *Liquid Crystals* **32**, 1335 (2005).

[55] Rosenblatt, C., Susceptibility measurements of liquid crystal–quasispherical solute mixtures in the isotropic phase near the nematic–isotropic transition. *The Journal of Chemical Physics* **82**, 2790 (1985).

[56] Rauch, A. C.; Garg, S.; Jacobs, D. T., Phase transitions in a nematic binary mixture. *The Journal of Chemical Physics* **116**, 2213 (2002).

[57] Kyu, T.; Chiu, H. W.; Kajiyama, T., Induced smectic phase in a nematic liquid crystal mixture. *Physical Review E* **55**, 7105 (1997).

[58] Cuetos, A.; Martínez-Haya, B.; Lago, S.; Rull, L. F., Use of Parsons-Lee and Onsager theories to predict nematic and demixing behavior in binary mixtures of hard rods and hard spheres. *Physical Review E* **75**, 61701 (2007).

[59] Fritsche, J. *Les Comptes Rendus de l'Academie des Sciences* **69**, 1035 (1867).

[60] Dürr, H.; Bouas-Laurent, H., *Photochromism: molecules and systems* (Elsevier, Amsterdam, 2003).

[61] de Boni, L.; Rodrigues, J. J.; dos Santos, D. S.; Silva, C.; Balogh, D. T.; Oliveira, O. N.; Zilio, S. C.; Misoguti, L.; Mendonca, C. R., Two-photon absorption in azoaromatic compounds. *Chemical Physics Letters* **361**, 209 (2002).

[62] Kawata, S.; Kawata, Y., Three-dimensional optical data storage using photochromic materials. *Chem. Rev* **100**, 1777 (2000).

[63] Atkins, P.; de Paula, J., *Elements of physical chemistry* (Oxford University Press, Oxford, 2005).

[64] Noomnarm, U.; Clegg, R. M., Fluorescence lifetimes: fundamentals and interpretations. *Photosynthesis Research* **101**, 1 (2009).

[65] Zhao, Y.; Ikeda, T., *Smart light-responsive materials: Azobenzene-containing polymers and liquid crystals* (John Wiley & Sons, New Jersey, 2009).

[66] Rabek, J. F., *Photochemistry and photophysics, Vol. II* (CRC Press, Boca Raton, 1990).

[67] Gore, P. H.; Wheeler, O. H., Absorption spectra of aromatic azo and related compounds: III. substituted azobenzenes. *The Journal of Organic Chemistry* **26**, 3295 (1961).

[68] Morgante, C. G.; Struve, W. S., $S_2 \rightarrow S_0$ fluorescence in trans-azobenzene. *Chemical Physics Letters* **68**, 267 (1979).

[69] Nepras, M.; Lunak, S.; Hrdina, R.; Fabian, J., Electronic excited states of azo compounds: Strong $\pi\pi^*$ fluorescence of bis-4,4'-diethylaminoazobenzene. *Chemical Physics Letters* **159**, 366 (1989).

[70] Toro, C.; Thibert, A.; de Boni, L.; Masunov, A. E.; Hernandez, F. E., Fluorescence emission of Disperse Red 1 in solution at room temperature. *Journal of Physical Chemistry B* **112**, 929 (2008).

[71] Monti, S.; Dellonte, S.; Bortolus, P., The lowest triplet state of substituted azobenzenes: An energy transfer investigation. *Journal of Photochemistry* **23**, 249 (1983).

[72] Mita, I.; Horie, K.; Hirao, K., Photochemistry in polymer solids. 9. Photoisomerization of azobenzene in a polycarbonate film. *Macromolecules* **22**, 558 (1989).

[73] Monti, S.; Orlandi, G.; Palmieri, P., Features of the photochemically active state surfaces of azobenzene. *Chemical Physics* **71**, 87 (1982).

[74] Wachtveitl, J.; Nägele, T.; Puell, B.; Zinth, W.; Krüger, M.; Rudolph-Böhner, S.; Oesterhelt, D.; Moroder, L., Ultrafast photoisomerization of azobenzene compounds. *Journal of Photochemistry and Photobiology A: Chemistry* **105**, 283 (1997).

[75] Brown, C. J., A refinement of the crystal structure of azobenzene. *Acta Crystallographica* **21**, 146 (1966).

[76] Hampson, G. C.; Robertson, J. M., Bond lengths and resonance in the cis-azobenzene molecule. *Journal of the Chemical Society* 409–413 (1941).

[77] Mostad, A.; Rømming, C., Refinement of crystal-structure of cis-azobenzene. *Acta Chemica Scandinavica* **25**, 3561 (1971).

[78] Holland, N. B.; Hugel, T.; Neuert, G.; Cattani-Scholz, A.; Renner, C.; Oesterhelt, D.; Moroder, L.; Seitz, M.; Gaub, H. E., Single molecule force spectroscopy of azobenzene polymers: Switching elasticity of single photochromic macromolecules. *Macromolecules* **36**, 2015 (2003).

[79] Hartley, G. S., The cis-form of azobenzene. *Nature* **140**, 281 (1937).

[80] Brown, E. V.; Granneman, G. R., Cis-trans isomerism in pyridyl analogs of azobenzene. Kinetic and molecular-orbital analysis. *Journal of the American Chemical Society* **97**, 621 (1975).

[81] Shirota, Y.; Moriwaki, K.; Yoshikawa, S.; Ujike, T.; Nakano, H., 4-[Di (biphenyl-4-yl) amino] azobenzene and 4, 4′-bis [bis (4′-tert-butylbiphenyl-4-yl) amino] azobenzene as a novel family of photochromic amorphous molecular materials. *Journal of Materials Chemistry* **8**, 2579 (1998).

[82] Barrett, C. J.; Mamiya, J.; Yager, K. G.; Ikeda, T., Photo-mechanical effects in azobenzene-containing soft materials. *Soft Matter* **3**, 1249 (2007).

[83] Gegiou, D.; Muszkat, K. A.; Fischer, E., Temperature dependence of photoisomerization. V. Effect of substituents on the photoisomerization of stilbenes and azobenzenes. *Journal of the American Chemical Society* **90**, 3907 (1968).

[84] Shen, Y. Q.; Rau, H., The environmentally controlled photoisomerization of probe molecules containing azobenzene moieties in solid poly(methyl methacrylate). *Die Makromolekulare Chemie* **192**, 945 (1991).

[85] Albini, A.; Fasani, E.; Pietra, S., The photochemistry of azo dyes. Photoisomerisation versus photoreduction from 4-diethylaminoazobenzene and 4-diethylamino-4′-methoxyazobenzene. *Journal of the Chemical Society, Perkin Transactions 2* **1983**, 1021 (1983).

[86] Fischer, E., Calculation of photostationary states in systems A $\rightleftharpoons$ B when only A is known. *The Journal of Physical Chemistry* **71**, 3704 (1967).

[87] Beltrame, P. L.; Paglia, E. D.; Castelli, A.; Tantardini, G. F.; Seves, A.; Marcandalli, B., Thermal cis-trans isomerization of azo dyes in poly(methyl methacrylate) matrix: A kinetic study. *Journal of Applied Polymer Science* **49** (1993).

[88] Rau, H.; Lüddecke, E., On the rotation-inversion controversy on photoisomerization of azobenzenes. Experimental proof of inversion. *Journal of the American Chemical Society* **104**, 1616 (1982).

[89] Fujino, T.; Tahara, T., Picosecond time-resolved raman study of trans-azobenzene. *Journal of Physical Chemistry A* **104**, 4203 (2000).

[90] Fujino, T.; Arzhantsev, S. Y.; Tahara, T., Femtosecond time-resolved fluorescence study of photoisomerization of trans-azobenzene. *Journal of Physical Chemistry A* **105**, 8123 (2001).

[91] Angeli, C.; Cimiraglia, R.; Hofmann, H. J., On the competition between the inversion and rotation mechanisms in the cis-trans thermal isomerization of diazene. *Chemical Physics Letters* **259**, 276 (1996).

[92] Naito, T.; Horie, K.; Mita, I., Photochemistry in polymer solids. 11. The effects of the size of reaction groups and the mode of photoisomerization on photochromic reactions in polycarbonate film. *Macromolecules* **24**, 2907 (1991).

[93] Lamarre, L.; Sung, C. S. P., Studies of physical aging and molecular motion by azochromophoric labels attached to the main chains of amorphous polymers. *Macromolecules* **16**, 1729 (1983).

[94] Gerstein, B. C.; Dybowski, C. R., *Transient techniques in NMR of solids: an introduction to theory and practice* (Academic Press, Orlando, 1985).

[95] Emsley, J. W., NMR methods of studying orientational order in the liquid crystalline and isotropic phases of mesogenic samples. *Liquid Crystals* **32**, 1515 (2005).

[96] Crawford, G. P.; Yang, D. K.; Žumer, S.; Finotello, D.; Doane, J. W., Ordering and self-diffusion in the first molecular layer at a liquid-crystal–polymer interface. *Physical review letters* **66**, 723 (1991).

[97] Cowan, B. P., *Nuclear magnetic resonance and relaxation* (Cambridge University Press, Cambridge, 1997).

[98] Slichter, C. P., *Principles of magnetic resonance* (Springer-Verlag, New York, 1990).

[99] Brochard, F.; Jouffroy, J.; Levinson, P., Phase diagrams of mesomorphic mixtures. *Journal de Physique* **45**, 1125 (1984).

[100] Chiu, H.; Kyu, T., Equilibrium phase behavior of nematic mixtures. *The Journal of Chemical Physics* **103**, 7471 (1995).

[101] Gramsbergen, E. F.; Longa, L.; de Jeu, W. H., Landau theory of the nematic-isotropic phase transition. *Physics Reports* **135**, 195 (1986).

[102] de Jeu, W. H.; Leenhouts, F., Physical properties of nematic p, p′-diheptylazobenzene. *Journal de Physique* **39**, 869 (1978).

[103] Zimmerman, G.; Chow, L. Y.; Paik, U. J., The Photochemical Isomerization of Azobenzene1. *Journal of the American Chemical Society* **80**, 3528 (1958).

[104] Crawford, G. P.; Steele, L. M.; Ondris-Crawford, R.; Iannacchione, G. S.; Yeager, C. J.; Doane, J. W.; Finotello, D., Characterization of the cylindrical cavities of Anopore and Nuclepore membranes. *The Journal of Chemical Physics* **96**, 7788 (1992).

[105] Ernst, R. R.; Bodenhausen, G.; Wokaun, A., *Principles of nuclear magnetic resonance in one and two dimensions* (Oxford University Press, Oxford, 2004).

[106] Sánchez Ferrer, A., *Photoactive Liquid-Crystalline Elastomers*, Ph.D. thesis, Universitat de Barcelona, Barcelona (2006).

[107] Vilfan, M.; Apih, T.; Gregorovič, A.; Zalar, B.; Lahajnar, G.; Žumer, S.; Hinze, G.; Böhmer, R.; Althoff, G., Surface-induced order and diffusion in 5CB liquid crystal confined to porous glass. *Magnetic resonance imaging* **19**, 433 (2001).

[108] Emsley, J. W.; Hashim, R.; Luckhurst, G. R.; Shilstone, G. N., Solute alignment in liquid crystal solvents: The Saupe ordering matrix for anthracene dissolved in uniaxial liquid crystals. *Liquid Crystals* **1**, 437 (1986).

List of publications

Publications in refereed journals

1. Blinc, R.; Laguta, V. V.; Zalar, B.; Zupančič, B.; Itoh, M., ^{17}O and ^{93}Nb NMR investigation of magnetoelectric effect in $Pb(Fe_{1/2}Nb_{1/2})O_3$. *Journal of Applied Physics* **104**, 084105 (2008).

2. Devetak, M.; Zupančič, B.; Lebar, A.; Umek, P.; Zalar, B.; Domenici, V.; Ambrožič, G.; Žigon, M.; Čopič, M.; Drevenšek-Olenik, I., Micropatterning of light-sensitive liquidcrystal elastomers. *Physical Review E* **80**, 50701 (2009).

3. Domenici, V.; Ambrožič, G.; Čopič, M.; Lebar, A.; Drevenšek-Olenik, I.; Umek, P.; Zalar, B.; Zupančič, B.; Žigon, M., Interplay between nematic ordering and thermomechanical response in a side-chain liquid single crystal elastomer containing pendant azomesogen units. *Polymer* **50**, 4837 (2009).

Conference proceedings

1. Domenici, V.; Zupančič, B.; Remškar, M.; Laguta, V. V.; Veracini, C. A.; Zalar, B., New composites based on liquid crystalline elastomers and electroactive nanomaterials. *Advances in Science and Technology* **61**, 34 (2008).

Index of Figures

Index of Tables